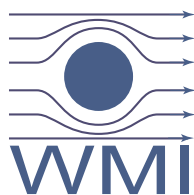


Annual Report
Jahresbericht

2005



WALTHER-MEISSNER-INSTITUT
für Tieftemperaturforschung
Bayerische Akademie der Wissenschaften



Contact:

Prof. Dr. Rudolf Gross
Walther–Meißner–Institute for Low Temperature Research
Bavarian Academy of Sciences
and
Chair for Technical Physics – E23
Technical University of Munich

Address:

Walther–Meißner–Str. 8	Phone:	+49 – (0)89 289 14201
D - 85748 Garching	Fax:	+49 – (0)89 289 14206
GERMANY	e-mail:	Rudolf.Gross@wmi.badw.de
	WWW-address:	http://www.wmi.badw.de

Secretary's Office:

Jutta Laaser	Phone:	+49 – (0)89 289 14202
	Fax:	+49 – (0)89 289 14206
	e-mail:	Jutta.Laaser@wmi.badw.de

Emel Dönertas	Phone:	+49 – (0)89 289 14205
	Fax:	+49 – (0)89 289 14206
	e-mail:	Emel.Doenertas@wmi.badw.de

Preface

The research activities of the Walther–Meißner–Institute for Low Temperature Research (WMI) are focused on low temperature solid state and condensed matter physics as well as the development of techniques and methods for low and ultra-low temperature experiments. The WMI is operated by the Commission for Low Temperature Research of the Bavarian Academy of Sciences. At the same time the WMI is the host institute of the chair for Technical Physics (E 23) of the Technical University of Munich (TUM) with the director of the WMI being ordinarium at the Faculty of Physics of the Technical University of Munich. Since 2004 the WMI also hosts a new scanning probe division with the head of this division being professor at the Ludwig-Maximilians-University of Munich (LMU). In this way a tight collaboration has been established between research groups of both Munich universities joining technological and human resources in the fields of experimental and theoretical solid state and condensed matter physics, low temperature techniques, materials science as well as thin film and nanotechnology. The WMI also supplies liquid helium to more than 20 research groups at both Munich universities and provides the technological basis for low temperature research.

The research program of the WMI is devoted to both **fundamental** and **applied research** and also addresses **materials science** aspects. With respect to **basic research** the main focus of the WMI is on

- superconductivity and superfluidity,
- magnetism and spin transport,
- quantum phenomena in mesoscopic systems and nanostructures,
- self-organization of molecules on surfaces,
- and the general properties of metallic systems at low and very low temperatures.

The WMI also conducts **applied research** in the fields of

- solid state based quantum information processing systems,
- superconducting and spintronic devices,
- oxide electronics,
- and the development of low and ultra low temperature systems and techniques.

With respect to **materials science** the research program is focused on

- the synthesis of superconducting and magnetic materials,
- the single crystal growth of oxide materials,
- the epitaxial growth of complex oxide heterostructures and multifunctional materials systems,
- and the growth of self-organized molecular ad-layers.

The year 2005 brought a few important improvements of the technological infrastructure of the WMI. Firstly, the installation of a new helium liquefier (Linde TCF 20) and the reconstruction of the helium recovery systems has been completed. Already much more than 100 000 liters of

liquid helium have been produced by the new machine and supplied to the research groups at both Munich universities. Due to the improved efficiency of the new system the price for liquid helium is expected to stay stable despite strongly increasing energy costs. Secondly, by the installation of a new UHV sputtering system and a Reactive Ion Etching (RIE) system in 2005, the WMI also could improve the thin film technology required for the fabrication of metallic nanostructures such as superconducting quantum bits. Finally, a new ultra low temperature system has been developed and fabricated at the WMI and set up in the basement. This systems is particularly designed for the study of solid state based quantum information systems.

The WMI is involved in several long-term research projects. The first to mention is the Cooperative Research Center SFB 631 on *Solid State Based Quantum Information Processing: Physical Concepts and Materials Aspects*, which has been installed by the German Science Foundation in July 2003 (see <http://www.wmi.badw-muenchen.de/SFB631>). The second is the Research Unit FOR 538 on *Doping Dependence of Phase Transitions and Ordering Phenomena in Cuprate Superconductors*, which has been installed by the German Science Foundation in April 2004 (see <http://www.wmi.badw-muenchen.de/FG538>). Both for the SFB 631 and the FOR 538 the spokesperson and coordinator of the coordinated research programs are members of the WMI. Thirdly, the WMI is participating in the Priority Programme 1157 of the German Science Foundation on *Integrated Electroceramic Functional Systems* with a project on *New Functional Thin Film Systems Based on Artificial Heterostructures of Transition Metal Oxides*. This project has been evaluated very positively in 2005 and is continued for further two years. There are further smaller national and international projects that are listed in the section on “Research Projects and Cooperations” in this report. All our research projects have been successfully continued in 2005. To intensify the collaboration with our partners, the WMI also was organizing several national and international workshops in 2005.

With respect to research the year 2005 has been very successful for the WMI. This is demonstrated by a large number of scientific papers in high quality journals, invited presentations at national and international conferences as well as seminar talks and colloquia. I particularly would like to mention that Dr. Kurt Uhlig of WMI received the “*Cryogenics 2004 Award*” for his article *Dry dilution refrigerator with pulse tube precooling*. Besides this scientific honoring an equally important aspect is the fact that the dry dilution refrigerator developed at WMI is starting to become a successful product.

The staff of the WMI was still growing in 2005 due to the increasing number of PhD and diploma/master students. Throughout 2005, an average of 13 scientific staff members, 18 members of the administrative and technical staff, 15 doctorate candidates, more than 20 diploma/master students as well as a large number of short and long-term guests belonged to the institute. The high level of scientific productivity of the WMI strongly profits from the collaborative atmosphere, the commitment and high motivation of our research and technical staff and the support of various funding agencies. In particular, we acknowledge the financial support from the Bavarian Academy of Sciences, the German Science Foundation, the Bavarian Ministry for Science and Arts, the BMBF and the EU. Unfortunately, in the same way as in the years 2002 to 2004 the WMI has to suffer a cut-back of its annual total budget by more than 15% in 2005. Although this reduction could be partly compensated by the very successful acquisition of additional research money from various funding agencies, on the long term similar cut-backs will significantly affect the technical equipment of the WMI and in turn its competitiveness in acquiring external research projects..

The Annual Report 2005 gives an overview on the scientific results of the WMI, which in many cases have been obtained within joint national and international research projects and in close

collaboration with international guests. The report is intended to provide an overview on our work to our friends and partners in research and industry and thereby to intensify our numerous collaborations. In order to be useful also for our numerous international partners the report is written in English.

I finally would like to thank all the colleagues, guests, students, post-docs and cooperating partners, who contributed to the success of our work within the last year, and last but not least all our friends and sponsors for their interest, trust and continuous support.



Rudolf Gross

Garching, December 2005



The majority of the WMI group members (October 2005)

Contents

Preface	1
The Walther–Meißner–Institute	7
Reports:	9
Basic Research	9
Ginzburg-Landau Analysis of the Doll-Näbauer Experiment	9
The Shear Viscosity of Superfluid ^3He in Aerogel	12
Charge Ordering Phenomena in High Temperature Superconductors	16
Weakly Incoherent versus Coherent Interlayer Magnetotransport in a Layered Metal	19
Field-induced Charge-Density-Wave Transitions	23
Low-frequency $1/f$ -Noise in LSMO:MgO Nanocomposite Films	26
Magnetic Polarization of Re in the Double Perovskite $\text{Sr}_2\text{CrReO}_6$	29
Structure and Dynamics of Molecular Self-Organization	32
Magnetization Studies on Nuclear Ordered Phases of Solid ^3He in Ag Sinters	35
Redox Reactions and Polypyrrole Formation in Vermiculites from Spain	38
Application Oriented Basic Research	40
Large Geometrically Enhanced TMR Effect in Magnetite Based Magnetic Tunnel Junctions	40
Generation of Microwave Single Photons and Homodyne Detection on a Chip	44
Microwave Spectroscopy on Single Josephson Junctions	49
Ferromagnetism in Cobalt Doped ZnO	52
Materials and Experimental Techniques	55
Fabrication of Superconducting Flux Qubits	55
Dry Fridge Continued	58
Single Crystal Growth of Cuprate Superconductors	61
Scanning Probe Division of the WMI	65
The New Helium-Liquefier at the WMI	67

Experimental Facilities	69
Publications	81
Theses, Appointments, Awards	85
Research Projects and Cooperations	89
Invited Conference Talks and Seminar Lectures	95
Seminars, Courses, Lectures and other Scientific Activities	101
Staff of the Walther-Meissner-Institute	109
Guest Researchers	111
Commission for Low Temperature Physics	113

The Walther–Meißner–Institute

The Walther–Meißner–Institute for Low Temperature Research (WMI) is operated by the Commission for Low Temperature Research of the Bavarian Academy of Sciences (BAW). The Commissions (Research Groups) of the Bavarian Academy are set up in order to carry out long-term projects, which are too ambitious for the lifetime or capacity of any single researcher, or which require the collaboration of specialists in various disciplines. At present, the Bavarian Academy of Sciences consists of 36 Commissions with more than 300 employees. The WMI also is the host institute of the chair for Technical Physics (E 23) of the Technical University of Munich. The director of the WMI at the same time is ordinarius at the Faculty of Physics of the Technical University of Munich.

The research at the Walther–Meißner–Institute is focused on low temperature physics (see reports below). The WMI also develops systems and techniques for low and ultra-low temperature experiments. As typical examples we mention a dry mK-system that can be operated without liquid helium by using a pulse-tube refrigerator for precooling, a nuclear demagnetization cryostat for temperature down to below 100 μK , or very flexible dilution refrigerator inserts for temperatures down to about 20 mK fitting into a 2 inch bore. These systems have been engineered and fabricated at the WMI. Within the last years, several dilution refrigerators have been provided to other research groups for various low temperature experiments. The WMI also operates a helium liquifier with a capacity of more than 150.000 liters per year and supplies both Munich universities with liquid helium. To optimize the transfer of liquid helium into transport containers the WMI has developed a pumping system for liquid helium that is commercialized in collaboration with a company.

The individual research groups of the WMI offer a wide range of attractive research opportunities for diploma (graduate) students, PhD students and postdoctoral fellows. The WMI is equipped with state of the art facilities for the preparation and characterization of superconducting and magnetic materials as well as for various low and ultra-low temperature experiments. The main experimental and technological resources of the WMI are listed in the following.

Materials Preparation and Fabrication of Nanostructures

- Laser Molecular Beam Epitaxy system for oxide heterostructures (equipped with in-situ RHEED, AFM/STM system, atomic oxygen source, laser heating system, metallization)
- UHV magnetron sputtering systems for metals (e.g. Nb, Al, NiPd, ...)
- magnetron sputtering system for oxide heteroepitaxy (equipped with four sputtering guns and an oxygen ion gun)
- ion beam sputtering system
- UHV metallization system (equipped with e-gun and thermal evaporators)
- reactive ion beam etching (RIE) system (Plasmalab 80 Plus with ICP source, Oxford Instruments Plasma Technology)
- ion beam etching system equipped with a LN₂ cooled sample holder
- polishing machine for substrate preparation
- ultrasonic bonding machine
- 50 m² class 1000 clean room facility
- optical lithography (Süss maskaligner MJB 3, projection lithography)

- electron beam lithography (based on Philips XL 30 SFEG scanning electron microscope and Raith Elphy Plus lithography system including a laser stage)
- four-mirror image furnace for crystal growth

Characterization

- 2-circle x-ray diffractometer (Bruker D8 Advance, sample temperature up to 1 600°C)
- high resolution 4-circle x-ray diffractometer (Bruker D8 Discover)
- scanning electron microscope with EDX analysis
- UHV room temperature AFM/STM system
- 2048 u high resolution mass spectrometer (Fa. Pfeiffer, cross beam ion source, SEM)
- Low Energy Electron Diffraction (SPECTA-LEED, Fa. Omicron)
- two Raman spectroscopy systems (1.5 to 300 K, in-situ sample preparation)
- SQUID magnetometer (Quantum Design, 1.5 to 700 K, up to 7 Tesla)
- several high field magnet systems (up to 17 Tesla) with variable temperature inserts
- experimental set-ups for the measurement of noise including low noise SQUID amplifiers and signal analyzers
- high frequency network analyzer (up to 40 GHz) for the determination of high frequency parameters

Low temperature systems and techniques

- 5 K-Scanning Tunnelling Microscope (low temperature STM, Fa. Omicron)
- several $^3\text{He}/^4\text{He}$ dilution refrigerator inserts for temperatures down to 10 mK
- “dry” mK-cooler based on a dilution refrigerator with pulse-tube precooling
- ultra-low temperature facility for temperatures down to below 100 μK based on a nuclear demagnetization cryostat
- experimental set-ups for the measurement of specific heat, magnetization, thermal expansion as well as electrical and thermal transport properties as a function of temperature, magnetic field and pressure

Ginzburg-Landau Analysis of the Doll-Näbauer Experiment

Robert Doll and Dietrich Einzel

We consider a hollow type-I superconducting cylinder of length L , radius R and wall thickness d exposed to an external field H_0 . Let H_i be the magnetic field trapped inside this cylinder after the external field has been removed. Both the London- and the Ginzburg-Landau (GL) theory predict the flux quantization in the form

$$H_i(H_0) \pi R^2 = n\phi_0 \quad ; \quad \phi_0 = \frac{hc}{2e} \quad (1)$$

with ϕ_0 the flux quantum. The experimental verification of the fluxoid quantization by Doll and Näbauer [1] and Deaver and Fairbank [2] has led to various attempts to describe theoretically the dependence of the trapped flux on the applied field H_0 and geometrical parameters [3 – 5]. In this short note we provide a self-consistent GL-analysis of the Doll-Näbauer experiment, which enables us to describe the dependence of $H_i(H_0)$ on H_0 analytically. To our knowledge, this has not been attempted before.

The description starts from the macroscopic pair wave function (pair field), which reads in cylindrical co-ordinates $\mathbf{r} = \{r, \theta, z\}$

$$\psi(r, \theta, H_0, T) = \psi_\infty(T) f_0(r, H_0, T) e^{i\varphi(\theta)} \quad (2)$$

The pair field ψ_∞ is related to the equilibrium superfluid density $n^s = 2\psi_\infty^2$ and leads to a temperature dependent form of the London penetration depth $\lambda_L^2 = mc^2/4\pi n^s e^2$. The normalized pair field f_0 will turn out to carry the information of the magnetic field dependence of f_0 . Assuming that the thickness d of the cylinder wall is small compared with the GL coherence length, spatial derivatives of f_0 can be neglected and the Gibbs free energy, appropriate for the case that H_0 represents the independent variable, is of the form [6]

$$G_S = G_N + \int d^3r \left\{ \frac{[H(r) - H_0]^2}{8\pi} + \frac{m}{2} n^s f_0^2 v^s{}^2 + \frac{H_c^2}{8\pi} (f_0^4 - 2f_0^2) \right\} \quad (3)$$

Here G_N is the Gibbs free energy of the normal state, the first term in the curly brackets describes the hole contribution and the rest represents the contribution to G_S from the cylinder wall. In (3)

$$v^s = -\frac{e}{mc} \left[A(r) - \frac{\phi_0}{2\pi r} \frac{\partial \varphi}{\partial \theta} \right] \quad (4)$$

is the superfluid velocity with $A(r)$ the component of the vector potential oriented in the azimuthal direction, which is related to the magnetic field via $H(r) = A' + A/r$. As usual, H_c denotes the thermodynamical critical field entering the condensation energy $H_c^2/8\pi$. The uniqueness of the pair wave function $\psi(r, \theta) \equiv \psi(r, \theta + 2\pi)$ implies $\partial\varphi/\partial\theta = n$ with $n = 0, 1, 2, \dots$. In the Doll-Näbauer experiment the trapped field inside the cylinder is constant and one may write $H(r) = H_i$ for $0 < r < R$ and $H(r) = H_0$ for $r > R + d$ with $H_i = 2A(r)/r$. Writing the supercurrent in the cylinder wall in the usual form $j_e^s(r) = en^s f_0^2 v^s$, the magnetic field $H(r)$ can be obtained from Amperes law $-\partial H/\partial r = (4\pi/c) j_e^s$ by integration over r . This generates a geometry factor $\gamma^2 = Rd/2\lambda_L^2 = \gamma^2(0)n^s/n$ ($\gamma^2(0) \approx 377 \gg 1$ in the geometry of the Doll-Näbauer experiment) and leads to the following relationship between H_i and H_0

$$H_i = \frac{H_0 + \gamma^2 f_0^2 H_n}{1 + \gamma^2 f_0^2} \quad ; \quad H_n = \frac{n\phi_0}{\pi R^2} \quad (5)$$

From (5) one immediately observes that the flux quantization is closely connected to pair condensation ($f_0 > 0$), since for $f_0 = 0$ one recovers the normal state result $H_i = H_0$. Note that equation (1) is recovered only in the limit $\gamma^2 \gg 1$ and that the flux quantum is reduced by geometry effects in the general case [3–5]. Variation of G_S w.r.t. f_0 leads to

$$f_0^2 = 1 - z^2 ; \quad z = \frac{R}{\sqrt{8}\lambda_L} \frac{H_i - H_n}{H_c} \quad (6)$$

Using (6), one may eliminate the trapped field H_i from (5) in favor of H_0 to get:

$$H_0 = H_n + \frac{\sqrt{8}\lambda_L}{R} H_c \gamma^2 [a - z^2] z ; \quad a = 1 + \frac{1}{\gamma^2} \quad (7)$$

From (7) one observes how the system adjusts to a given external field H_0 below the condensation point ($f_0 > 0$) by the choice of a proper quantum number n and an appropriate value of the normalized pair field $f_0(T)$, dictated by the temperature-dependent values of $\lambda_L(T)$, $H_c(T)$ and $\gamma^2(T)$. A numerical solution of (7) has been provided by R. Doll [7]. Alternatively, we may aim at an analytical solution of the problem, since both Eqs. (5) and (7) can easily be shown to be equivalent to a (self-consistency) relation, which assumes the form of a standard cubic equation:

$$z^3 - az + \xi = 0 ; \quad \xi = \frac{1}{\sqrt{2}} \frac{\lambda_L}{d} \left(\frac{H_0 - H_n}{H_c} \right) \quad (8)$$

Eq. (8) has three real solutions, provided that $\xi \leq 2\rho$ with $\rho = (a/3)^{3/2}$, the physically relevant of which has the form

$$z(\xi) = 2\sqrt{\frac{a}{2}} \sin \left(\frac{\pi}{6} - \frac{1}{3} \arccos \frac{\xi}{2\rho} \right) ; \quad \rho = \left(\frac{a}{3} \right)^{3/2} \quad (9)$$

For practical purposes it is convenient to use the Taylor expansion of $z(\xi)$ about $\xi = 0$

$$z(\xi) = \frac{\xi}{a} + \frac{\xi^3}{a^4} + 3\frac{\xi^5}{a^7} + 12\frac{\xi^7}{a^{10}} + 55\frac{\xi^9}{a^{13}} + \dots \quad (10)$$

Inserting (9) into (5) one obtains the explicit dependence of the trapped field H_i on H_0 :

$$H_i(H_0) = H_n + \frac{H_0 - H_n}{1 + \gamma^2} [1 + h(\xi)] ; \quad h(\xi) \equiv \frac{a \cdot z(\xi)}{\xi} - 1 \quad (11)$$

Using the Taylor representation (10) of $z(\xi)$, the function $h(\xi)$ can be written as

$$h(\xi) = \frac{\epsilon^2}{a} \zeta_n^2 + \frac{3\epsilon^4}{a^2} \zeta_n^4 + \frac{12\epsilon^6}{a^3} \zeta_n^6 + \dots \quad (12)$$

$$\epsilon^2 = \frac{1}{2} \left(\frac{\lambda_L}{ad} \right)^2 ; \quad \zeta_n = \frac{H_0 - H_n}{H_c}$$

Eq. (11) clearly describes the step-like H_0 -field dependence of the trapped field H_i as influenced by geometry effects described by γ^2 . It should be emphasized that in the Doll–Näbauer experiment the field H_0 had to be removed, which corresponds to a change of the superconducting state accompanied by a modification of H_i . In Fig. 1 we plot the geometrical parameters which characterize the *finite* slope $(1 + \gamma^2)^{-1}$ of the H_0 -dependence of the flux quantization steps as well as the importance ($\propto \epsilon^2$) of higher order terms in the expansion for the specific sizes of the Doll–Näbauer experiment. The latter was performed on Pb with

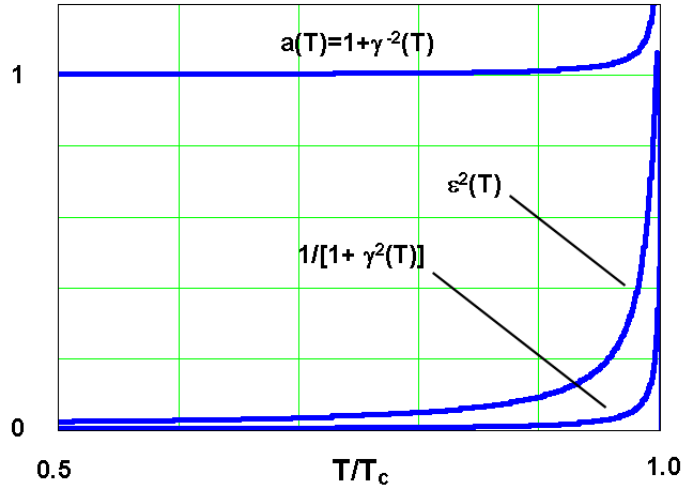


Figure 1: Geometry parameters appearing in the central Eqs. (11) and (13) as applied to the Doll–Näbauer experiment

$\lambda_L(0) = 3.9 \cdot 10^{-6} \text{cm}$, $d = 2 \cdot 10^{-5} \text{cm}$, $R = 5.739 \cdot 10^{-4} \text{cm}$. The slope is seen to be vanishingly small for temperatures not too close to the transition and the result for ϵ^2 justifies a truncation of the infinite series after a few terms. As a next step we compute the dominating hole contribution to the Gibbs free energy ($V_{\text{hc}} = \pi R^2 L$):

$$\begin{aligned} G_{\text{hole}} &= G_N + V_{\text{hc}} \frac{H_c^2}{4\pi} \left(\frac{d}{\lambda_L} \right)^2 \left[1 - z^2(\xi) \right]^2 z^2(\xi) \\ &= G_N + V_{\text{hc}} \frac{H_c^2}{8\pi} \frac{\gamma^2}{1 + \gamma^2} \zeta_n^2(H_0) \left\{ 1 - \frac{2\epsilon^2 \zeta_n^2}{1 + \gamma^2} - \frac{(6\gamma^2 - 1)\epsilon^4 \zeta_n^4}{(1 + \gamma^2)^2} - \dots \right\} \end{aligned} \quad (13)$$

Clearly, the correction terms in curly brackets are seen to be small and the main source of the magnetic field dependence of the Gibbs free energy G_S is the term $\propto \zeta_n^2$. A detailed analysis of the thermodynamics and field dependence of the Doll–Näbauer experiment, which is still a bit more complicated than the physics behind Eqs. (11) and (13), will be subject to a forthcoming publication.

References

- [1] R. Doll and M. Näbauer, Phys. Rev. Lett **7**, 51 (1961); Zeitschrift für Physik **169**, 526 (1962)
- [2] B. S. Deaver, Jr. and W. M. Fairbank, Phys. Rev. Lett. **7**, 43 (1961)
- [3] J. Bardeen, Phys. Rev. Lett. **7**, 162 (1961)
- [4] J. B. Keller and B. Zumino, Phys. Rev. Lett. **7**, 164 (1961)
- [5] D. H. Douglass, Jr., Phys. Rev. **132**, 513 (1963)
- [6] R. Doll and P. Graf, Zeitschrift für Physik, **197**, 172 (1966)
- [7] R. Doll, unpublished work

The Shear Viscosity of Superfluid ^3He in Aerogel

Dietrich Einzel

Introduction. We consider quite generally the shear viscosity in ^3He -B to which both impurity scattering (treated within the t -matrix approximation) and inelastic scattering contributes. A new interpolation scheme for the temperature dependence of the shear viscosity is presented which preserves all analytical results available for $T \rightarrow 0$ and $T \rightarrow T_c$ and allows for a transparent physical representation particularly of the impurity-limited shear viscosity. The two scattering processes are combined using Matthiessen's rule coupling. In superfluid ^3He -B silica aerogel acts as an impurity system. The latter is treated as a homogeneous isotropic scattering medium (HISM) [1]. Such an assumption is valid when the average spacing between the aerogel strands is smaller than the superfluid coherence length, and is applicable at low pressure and not too low aerogel concentrations. It is well established that the ^3He -B/aerogel system can be described by a spin triplet p-wave order parameter of the form (BW-state) $\Delta_{\mathbf{p}}^2 = \mathbf{d}_{\mathbf{p}} \cdot \mathbf{d}_{\mathbf{p}}^* = \Delta^2$. The transport properties of dirty superfluids originate from the (at low T dilute) gas of thermal excitations, the Bogoliubov quasiparticles (bogolons), which have the energy spectrum $E_{\mathbf{p}} = [\xi_{\mathbf{p}}^2 + \Delta^2]^{1/2}$ and the thermal distribution $\nu_{\mathbf{p}} = [\exp(E_{\mathbf{p}}/k_B T) + 1]^{-1}$. The shear viscosity η can be defined through the constitutive relation that connects the shear component of the momentum current Π_{xz} with the gradient of the bogolon velocity field $v_x^n(z)$

$$\Pi_{xz} = -\eta_{e,i} \frac{\partial v_x^n}{\partial z} ; \quad \eta_{e,i} = N_F \left\langle 2 \int_0^\infty dE_{\mathbf{p}} \varphi_{\mathbf{p}} p_x^2 v_{\mathbf{p}z}^2 \tau_{e,i}(\tilde{E}_{\mathbf{p}}) \right\rangle_{\text{FS}} ; \quad \varphi_{\mathbf{p}} = -\frac{\partial \nu(E_{\mathbf{p}})}{\partial E_{\mathbf{p}}} \quad (1)$$

In (1) $\eta_{e,i}$ and $\tau_{e,i}$ denote the shear viscosities and the transport times for elastic (e) and inelastic (i) scattering, N_F is the density of states for both spin projections, and $\langle \dots \rangle_{\text{FS}}$ abbreviates the Fermi surface average.

Elastic scattering. The impurity-limited transport time $\tau_e(\tilde{E}_{\mathbf{p}})$ is defined by [2]

$$\tau_e(\tilde{E}_{\mathbf{p}}) = \frac{\hbar}{\text{Im} \sqrt{\tilde{E}_{\mathbf{p}}^2 - \Delta^2}} \frac{1}{2} \left(1 + \frac{|\tilde{E}_{\mathbf{p}}^2| - \Delta^2}{|\tilde{E}_{\mathbf{p}}^2 - \Delta^2|} \right) \quad (2)$$

Here $\tilde{E}_{\mathbf{p}}$ is the bogolon energy renormalized by the impurity self-energy (computed within the t -matrix approximation):

$$\tilde{E}_{\mathbf{p}} = E_{\mathbf{p}} + \Sigma_e(\tilde{E}_{\mathbf{p}}) ; \quad \Sigma_e(\tilde{E}_{\mathbf{p}}) = i\hbar \Gamma_N^e \frac{D(\tilde{E}_{\mathbf{p}})(1+c^2)}{c^2 + D^2(\tilde{E}_{\mathbf{p}})} ; \quad D(\tilde{E}_{\mathbf{p}}) = \frac{\tilde{E}_{\mathbf{p}}}{\sqrt{\tilde{E}_{\mathbf{p}}^2 - \Delta^2}} \quad (3)$$

In Eq. (3)

$$\Gamma_N^e = \frac{1}{\tau_N^e} = \frac{2n_i}{\pi \hbar N_F} \frac{1}{(1+c^2)} \approx \frac{v_F}{\lambda_g}$$

represents the normal state scattering rate, with n_i the impurity concentration and λ_g the geometric mean free path. The parameter $c = \cot \delta_0$ is related to the scattering phase shift δ_0 , which is limited to the s-wave scattering approximation. Note that the superconducting density of states is related to $D(\tilde{E}_{\mathbf{p}})$ by $N_s(\tilde{E}_{\mathbf{p}})/N_0 = \text{Re} D(\tilde{E}_{\mathbf{p}})$. The impurity self energy has the following low energy behavior:

$$\Sigma_e(\tilde{E}_{\mathbf{p}}) = \Sigma_e'(\tilde{E}_{\mathbf{p}}) + i \Sigma_e''(\tilde{E}_{\mathbf{p}}) ; \quad \Sigma_e'(\tilde{E}_{\mathbf{p}}) \stackrel{E_{\mathbf{p}} \rightarrow 0}{=} 0 ; \quad \Sigma_e''(\tilde{E}_{\mathbf{p}}) \stackrel{E_{\mathbf{p}} \rightarrow 0}{=} \Sigma_e''(0) \quad (4)$$

$\tau_e(\tilde{E}_p)$ can be evaluated analytically in the limits $E_p \ll \Delta$ and $E_p \gg \Delta$:

$$\tau_e(\tilde{E}_p) = \begin{cases} \frac{\hbar \Sigma_e''(0)}{[\Delta^2 + \Sigma_e''(0)]^{\frac{3}{2}}} & ; \tilde{E}_p \ll \Delta \\ \tau_N^e \frac{E_p}{\sqrt{E_p^2 - \Delta^2}} \frac{1+c^2[D(E_p)]^{-2}}{(1+c^2)D(E_p)} \Theta(E_p - \Delta) & ; \tilde{E}_p \gg \Delta, \hbar \Gamma_N^e \ll \Delta \end{cases} \quad (5)$$

In (5) Θ denotes the Heaviside step function. The zero energy limit of the impurity self-energy can be evaluated analytically for arbitrary impurity scattering phase shifts

$$\Sigma_0''(0) = \left[\left[\frac{(\hbar \Gamma_N^e)^2 \Delta^2}{1+c^2} + \frac{(\hbar \Gamma_N^e)^4}{4} \right]^{\frac{1}{2}} + \frac{(\hbar \Gamma_N^e)^2}{2} - \frac{\Delta^2 c^2}{1+c^2} \right]^{\frac{1}{2}} \quad (6)$$

$\Sigma_0''(0)$ is seen to decrease with increasing $c = \cot \delta_0$ and to vanish for $c = [\hbar \Gamma_N^e / (\Delta - \hbar \Gamma_N^e)]^{\frac{1}{2}} = [2n_i / \pi N_F \Delta]^{\frac{1}{2}}$. Eq. (5) can be used to calculate both the zero temperature limit and the temperature dependence of η . In the zero temperature limit we may define a dimensionless quantity C_η through

$$C_\eta = \frac{\hbar \Gamma_N \Sigma_0''(0)}{[\Sigma_0''(0) + \Delta^2]^{\frac{3}{2}}} \quad (7)$$

The quantity C_η describes a normal-like low T contribution to the quasiparticle transport induced by resonant pair-breaking as a consequence of strong impurity scattering in the unitary limit. Like $\Sigma_e''(0)$, the pair breaking parameter C_η drops rapidly with decreasing δ_0 and vanishes for a critical value δ_{0c} . The temperature dependence of η_e can be estimated by observing that the self-consistent solution of Eq. (3) is relevant only for low energies. At high energies one may use the asymptotic form of $\tau_e(\tilde{E}_p)$ for $E_p \gg \Delta$. This gives rise to the definition of T -dependent generalized Yosida functions

$$Y_n = \int_{-\infty}^{\infty} d\xi_p \varphi_p \left| \frac{\xi_p}{E_p} \right|^n \quad (8)$$

From (5), using (7) and (8), one may construct the following interpolation procedure for the shear viscosity η :

$$\eta_e = \eta_N^e \left\{ C_\eta + (1 - C_\eta) \frac{Y_1 + c^2 Y_3}{1 + c^2} \right\} \quad (9)$$

Here $\eta_N^e = np_F v_F \tau_N^e / 5$ is the impurity-limited shear viscosity of the normal state. It should be emphasized that Eq. (9) is valid for arbitrary scattering phase shifts, but the pair-breaking parameter C_η is finite only in the proximity to the unitary scattering limit $\delta_0 \rightarrow \pi/2, c \rightarrow 0$, where it gives rise to a finite low- T limit of the viscosity η_e .

Inelastic scattering. The relaxation rate for *inelastic* scattering can be written in the form [3]

$$\frac{1}{\tau_i(E_p)} = \begin{cases} \frac{1}{\tau_N^i(T)} \left[1 + \left(\frac{\xi_p}{\pi k_B T} \right)^2 \right] & ; T > T_c \\ \frac{E_p}{\sqrt{E_p^2 - \Delta^2}} \frac{1}{\tau_B(E_p)} & ; T < T_c \end{cases} \quad (10)$$

Here $\tau_N^i(T) = \tau_N^i(T_c)(T_c/T)^2$ is the inelastic relaxation time of the normal Fermi liquid. The relaxation time $\tau_B(E_p)$ has been discussed in ref. [3]. At low temperatures it has the asymptotic form

$$\lim_{T \rightarrow 0} \frac{1}{\tau_B(E_p)} = \frac{1}{\tau_B^0} = \frac{3w_0 e^{-\frac{\Delta}{k_B T}}}{\sqrt{2\pi} \tau_N^i} \left(\frac{\Delta}{k_B T} \right)^{\frac{3}{2}} \quad (11)$$

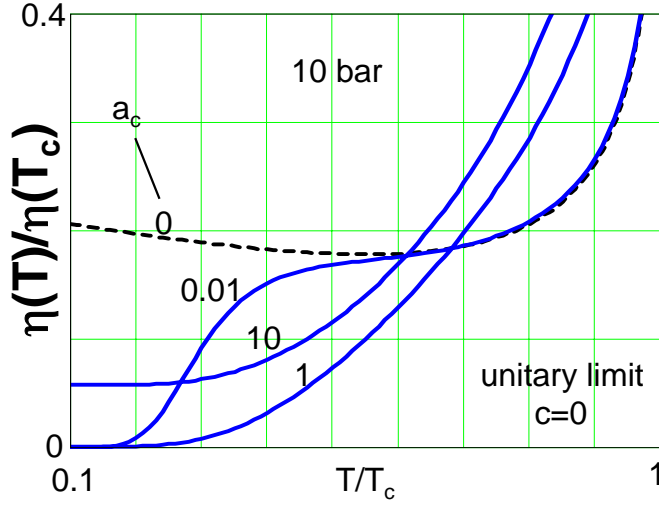


Figure 1: Total reduced shear viscosity at a pressure of 10 bar in the unitary limit vs. reduced temperature for various values of the parameter $a_c = \bar{\tau}_N^i(T_c)/\tau_N^e$. Note that $a_c = 0$ corresponds to the clean limit.

with $w_0 \approx 1$. For our purposes it is sufficient to work with the thermal average

$$\frac{1}{\bar{\tau}_B(T)} = \frac{\sum_{\mathbf{p}\sigma} \varphi_{\mathbf{p}}/\tau_B(E_{\mathbf{p}})}{\sum_{\mathbf{p}\sigma} \varphi_{\mathbf{p}}} = \begin{cases} \frac{1}{\bar{\tau}_N^i(T)} \equiv \frac{4}{3} \frac{1}{\tau_N^i(T)} & ; T > T_c \\ \frac{1}{\bar{\tau}_B^0(T)} & ; T < T_c \end{cases} \quad (12)$$

One may now interpolate the full temperature–dependent thermally averaged bogolon relaxation rate along the lines of the procedure proposed in [4] to get

$$\frac{1}{\bar{\tau}_B(T)} = \frac{Y_0(T)}{\bar{\tau}_N^i(T)} \left\{ \frac{9w_0\Delta(0)}{8\pi k_B T} [1 - t^\alpha] + t^{\alpha-1} \right\} \quad (13)$$

with $t = T/T_c$. The exponent α has to be chosen such that the slope of the interpolated bogolon relaxation rate coincides with that of an exact numerical evaluation [3].

Finally the inelastic contribution to the shear viscosity η_i can be written in the form

$$\eta_i = \eta_N^i Y_2 \frac{\bar{\tau}_B}{\bar{\tau}_N^i} \frac{1 - \lambda_\eta}{1 - \lambda_\eta Y_2/Y_0} \quad (14)$$

where Y_n is defined through Eq. (8) and λ_η is pressure–dependent scattering parameter that accounts for the vertex corrections in the collision integral [3]. As a last step, the elastic and inelastic contributions to η can be approximately combined using Matthiessen’s rule approximation

$$\frac{1}{\eta} = \frac{1}{\eta_e} + \frac{1}{\eta_i} \quad (15)$$

Discussion. In Figs. 1 and 2 we show numerical evaluations of the total reduced viscosity according to (14) for unitary and Born scattering, respectively, at a pressure of 10 bar. In the unitary case, for not too large values of the parameter $a_c = \tau_N^i(T_c)/\tau_N^e$, the viscosity is seen to almost vanish in the zero temperature limit. If, on the other hand, $a_c = 10$ (corresponding to an approximately 99.3% open aerogel) the viscosity has a finite low T limit. For Born scattering (Fig. 2) the viscosity falls off much more rapidly ($\propto Y_3$) at low T . It is interesting to note that crossing points like those observable in Fig. 2 (Born limit) for the shear viscosity vs. reduced

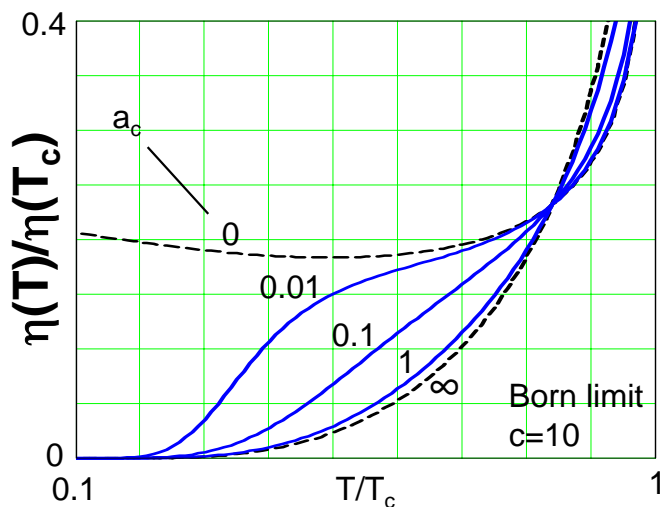


Figure 2: Total reduced shear viscosity in the Born limit vs. reduced temperature for various values of the parameter $a_c = \bar{\tau}_N^i(T_c)/\tau_N^e$.

temperature, which generally occur in context with a superposition law [5], arise here as a consequence of the Matthiessen rule approximation. In this contribution, we have, for the first time, calculated the *impurity-limited* shear viscosity η_e [6] and combined the effects of elastic and inelastic scattering to yield a comprehensive picture of the *total* shear viscosity η of the ^3He -B/aerogel system. η can be predicted to be impurity-limited for a wide range of experimentally accessible aerogel concentrations. A comparison of this theory with future experiments may discriminate whether the impurity-limited transport is characterized by scattering in the Born or the unitary limit and may allow to determine the nature of change in δ_0 with the addition of ^4He [6]. The dominance of the unitary limit is supported, for example, by refs. [6,7].

References

- [1] E.V. Thuneberg, S.K. Yip, M. Fogelström, J.A. Sauls, Phys. Rev. Lett. **80**, 2861 (1998)
- [2] P.J. Hirschfeld, P. Wölfle, J.A. Sauls, D. Einzel, W.O. Putikka, Phys. Rev. **B 40**, 6695 (1989)
- [3] D. Einzel, J.M. Parpia, J. Low Temp. Phys. **109**, 1 (1997)
- [4] D. Einzel, J. Low Temp. Phys. **131**, 1 (2003)
- [5] D. Vollhardt, private communication (2005)
- [6] A.I. Golov, D. Einzel, G. Lawes, K. Matsumoto, J.M. Parpia, Phys. Rev. Lett. **92**, 195301-1 (2004)
- [7] S.N. Fisher, A.M. Guenault, A.J. Hale, G.R. Pickett, J. Low Temp. Phys. **126**, 673 (2001)

Charge Ordering Phenomena in High Temperature Superconductors

*L. Tassini, W. Prestel, R. Hackl, A. Erb, M. Lambacher, T. Fujita, N. Kikugawa*¹

The high temperature superconductors (HTSC) have a complex phase diagram with many white spots. A substantial part of the debate focuses on the normal state at low and optimal doping p . Motivated mainly by the linear resistivity above the superconducting dome in the doping range where the transition temperature T_c is maximal ($p \simeq 0.16$) the metallic state was interpreted in terms of fluctuations leading to marginal behaviour of the electronic properties [1].

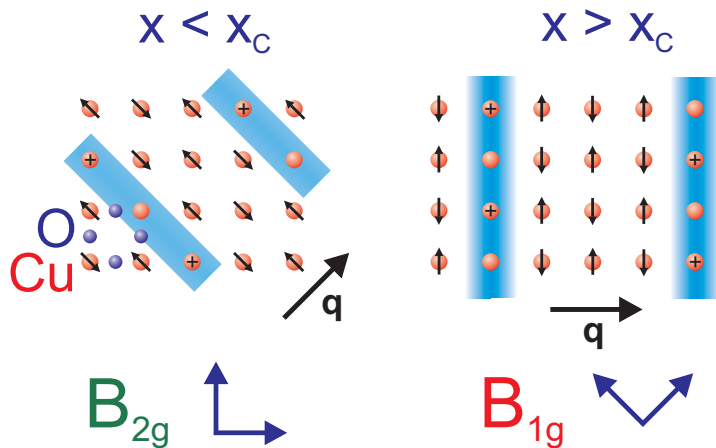


Figure 1: Sketch of spin-charge-ordered states in the copper-oxygen plane (adopted from ref. [9]). There are antiferromagnetic insulating areas and charged spin-free “stripes”. The modulation is characterized by the vector \mathbf{q} . If the pattern fluctuates the correlation length ξ_s is finite and can be as small as a few lattice constants. The response of 1D objects perpendicular to the modulation direction \mathbf{q} can only be observed by Raman scattering if the polarization vectors of both the incoming and the outgoing photons have a finite projection on either \mathbf{q} or the stripe direction for transverse or longitudinal excitations, respectively. This implies that stripes parallel to the principal axes can be observed only in B_{1g} and diagonal ones only in B_{2g} symmetry.

In the underdoped range ($p < 0.16$) metallic behaviour with linear resistivity $\rho(T)$ still prevails at high temperatures while there are deviations below a doping dependent cross over line characterized by $T^*(p)$ [2]. For $T < T^*$, not only $\rho(T)$ exhibits qualitatively new features [3], but also the spin-lattice relaxation time T_1 [4], the thermopower, the optical conductivity, and the Raman spectra [5] deviate from what one expects for conventional metals [2, 6]. T^* is not very well defined and depends on the experimental method, in particular on the characteristic timescale of a probe. This observation can be explained naturally if fluctuations are assumed to dominate the physics in the entire phase diagram. Then the different values for T^* reflect the low-frequency

cutoff of each experimental technique [7]. The critical fluctuations above a putative quantum-critical point (QCP) can lead to strong interactions between the electrons and provide an effective mechanism for the formation of Cooper pairs [8]. This implies that the tendency of the charge to order into one-dimensional (1D) structures (stripes) could be a precursor of superconductivity. Therefore, the study of the dynamical properties of charge in the relevant range of doping and temperature can be important for the understanding of the cuprates.

Here we present a study of the underdoped region of different HTSC using electronic Raman scattering which shows the dynamical behaviour particularly well. In Fig. 2 the Raman response function of $\text{La}_{2-x}\text{Sr}_x\text{CuO}_4$ (LSCO) at doping levels of $x = 0.02$ and $x = 0.10$ are plotted. In B_{1g} symmetry at $x = 0.10$ and in B_{2g} symmetry at $x = 0.02$ (panels (a) and (d) of Fig. 2), the spectra exhibit the expected behaviour based on the experience of other materials studied at similar doping levels: the B_{1g} spectra depend only weakly on temperature, and the evolution of the initial slope of the B_{2g} spectra follows the resistivity as obtained by transport

¹This work is supported by the German Science Foundation (projects Ha2071/[2-4]) via Research Unit 538.

measurements. Vice versa, in the other spectra (panels (b) and (c) of Fig. 2) we observe a strong deviation from the expected behaviour. Very clearly, an additional response manifesting itself as a peak at low energy, is superimposed on the response of the two dimensional (2D) CuO_2 planes.

The nature of this additional response is still a matter of the theoretical discussion. From an experimental point of view, the most direct way to get an idea of how to interpret the new structures is via a relationship between the Raman selection rules and structural properties. It was shown by neutron scattering in $\text{La}_{2-x-y}\text{Nd}_y\text{Sr}_x\text{CuO}_4$ that an antiferromagnetic (AF) superstructure and static charged stripes separating the magnetic domains form at low temperature [9]. In $\text{La}_{2-x}\text{Sr}_x\text{CuO}_4$ the AF domains are oriented along the principal axes for $x > 0.055$ and oriented along the diagonals of the CuO_2 planes at $x < 0.055$ [10].

In the present experiment the charge response is measured. In particular, it is possible to distinguish between 1D stripes oriented along the principle axes and along the diagonals of the CuO_2 planes. In the first case, an additional feature appears in the B_{2g} symmetry, in the second one in B_{1g} symmetry (see caption of Fig. 1). Therefore, the observation of the low-energy Raman peaks in LSCO at B_{1g} and B_{2g} symmetry for $x = 0.10$ and $x = 0.02$, respectively, is evidence of the formation of 1D structures at low temperature which flip by 45° as function of doping.

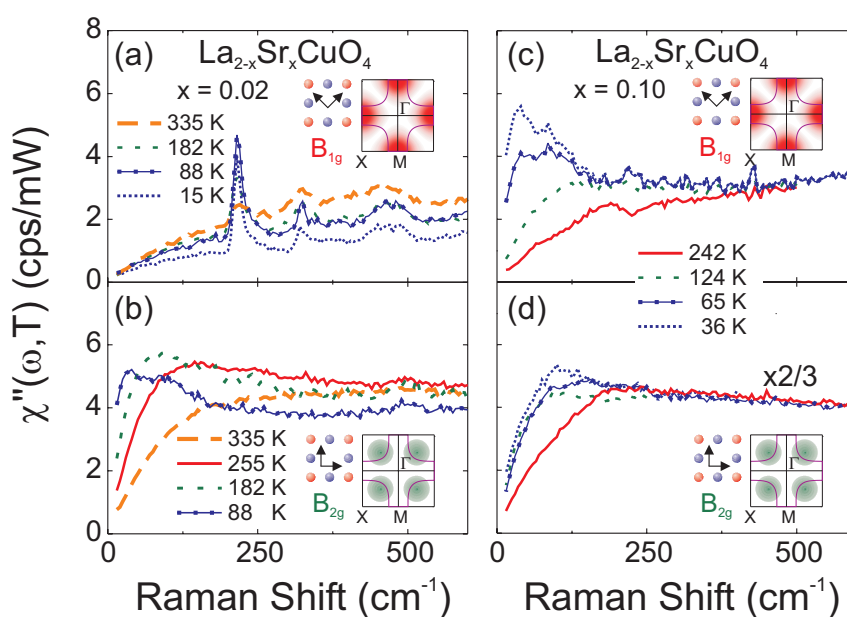


Figure 2: Raman response $\chi''_{\mu}(\omega, T)$ of $\text{La}_{1.98}\text{Sr}_{0.02}\text{CuO}_4$ (a,b) and $\text{La}_{1.90}\text{Sr}_{0.10}\text{CuO}_4$ (c,d). As indicated in the insets, areas around the M points and the center of the quadrant are projected out in B_{1g} and B_{2g} symmetry, respectively, on a quadratic 2D lattice. The selection rules for 1D structures are explained in Fig. 1.

The present interpretation of the additional features in terms of charge fluctuations is strongly supported by theory. An explicit calculation of the fluctuation diagrams predicts the observed spectral response and temperature dependence [12, 13].

It remains as an open point why the response from fluctuating stripes was not observed in other HTSC. In order to clarify whether fluctuating charge ordering is specific of LSCO or a general feature of all cuprates we performed experiments on single crystals of underdoped $\text{Y}_{1-x}\text{Ca}_x\text{Ba}_2\text{Cu}_3\text{O}_6$ (Y-123), with a virtually perfect tetragonal structure. In Fig. 3 Raman response functions of Y-123 at a doping level of $p \approx 0.02$ ($x = 0.03$) are shown. Similarly as in LSCO at a comparable doping level [Fig. 2 (a)], the B_{1g} spectra exhibit the behaviour expected for a correlated metal close to a Mott transition. In B_{2g} symmetry, however, we observe an exceptionally strong additional peak at low energy superimposed on the ordinary 2D response. For the spectral shape and the temperature dependence we conclude that the additional peak in Y-123 originates from fluctuating stripes similarly as in LSCO.

We hypothesize that the formation of fluctuating stripes is a general feature of cuprates. However, the correlation length ξ_s of the ordering phenomenon must exceed a minimal value to make the response visible. For example, in the case of phonons, translational symmetry must be established over several lattice constants to guarantee the selection rules to hold. Here, this seems to be a lower bound, and, more likely, the electronic mean free path ℓ is the relevant scale. On the other hand, ξ_s corresponds to a fluctuation frequency of order $\Omega_c \propto (\xi_s)^{-z}$ ($z = 2$ for damped modes). If ξ_s is substantially smaller than in LSCO Ω_c is expected to be larger. As a consequence, the intensity becomes weaker and is distributed over a larger energy range. Then, the response of the stripes cannot be separated from the usual one of the planes. We conclude that the charge-ordering instability is an intrinsic feature of the copper-oxygen plane. The maximal doping level up to which the stripes can be observed in a given compound directly depends on whether or not the lattice helps to stabilize the order.

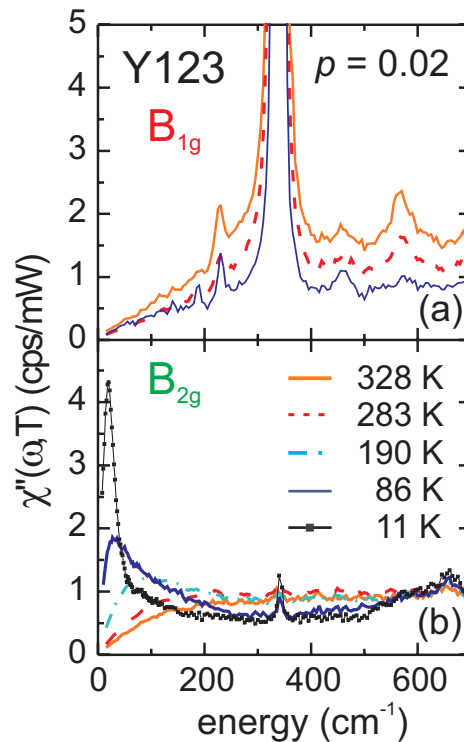


Figure 3: Raman response $\chi''_{\mu}(\omega, T)$ of $Y_{1.97}Ca_{0.03}Ba_2Cu_3O_6$ at B_{1g} and B_{2g} symmetries. Temperature and approximate carrier doping are indicated. From Ref. [11]

References

- [1] C.M. Varma, P.B. Littlewood, S. Schmitt-Rink, E. Abrahams, A.E. Ruckenstein, *Phys. Rev. Lett.* **63**, 1996 (1989).
- [2] T. Timusk, B.W. Statt, *Rep. Prog. Phys.* **62**, 61 (1999).
- [3] Y. Ando, S. Komiya, K. Segawa, S. Ono, and Y. Kurita, *Phys. Rev. Lett.* **93**, 267001 (2004).
- [4] S.J.L. Billinge, M. Gutmann and E.S. Božin, *Int. J. Mod. Phys. B* **17**, 3640 (2003) and M. Gutmann *et al.*, *cond-mat/0009141* (2000).
- [5] M. Opel *et al.*, *Phys. Rev. B* **61**, 9752 (2000).
- [6] J.L. Tallon and J.W. Loram, *Physica C* **349**, 53 (2001).
- [7] S. Andergassen, S. Caprara, C. Di Castro, M. Grilli, *Phys. Rev. Lett.* **87**, 056401 (2001).
- [8] C. Castellani, C. Di Castro, and M. Grilli, *Phys. Rev. Lett.* **75**, 4650 (1995).
- [9] J.M. Tranquada *et al.*, *Nature (London)* **375**, 561 (1995).
- [10] S. Wakimoto *et al.*, *Phys. Rev. B* **60**, R769 (1999); M. Fujita *et al.*, *Phys. Rev. B* **65**, 064505 (2002).
- [11] R. Hackl, L. Tassini, F. Venturini, Ch. Hartinger, A. Erb, N. Kikugawa, and T. Fujita, *Adv. Solid State Phys.* **45**, 227 (Edited by B. Kramer, Springer-Verlag Berlin 2005).
- [12] C. Di Castro, M. Grilli, S. Caprara, and D. Suppa, accepted for publication in *J. Phys. Chem. Solids*, *cond-mat/0408058* (2004).
- [13] S. Caprara, C. Di Castro, M. Grilli, and D. Suppa, *Phys. Rev. Lett.* **95**, 117004 (2005).

Weakly Incoherent versus Coherent Interlayer Magnetotransport in a Layered Metal

M. V. Kartsovnik, D. Andres, and W. Biberacher¹

The extremely high electronic anisotropy is a common feature of many exotic conductors extensively investigated in the recent years, such as, for example, organic conductors, superconducting copper oxides, and some magnetic oxides with colossal magnetoresistance. The mechanism of the interlayer charge transfer is one of the central questions in understanding the nature of various ground states and electronic properties of these materials. In particular, the problem of discriminating between coherent and incoherent interlayer transport has received much attention (see, e.g., [1, 2, 3, 4]).

If the interlayer hopping rate, $\sim t_{\perp}/\hbar$, where t_{\perp} is the interlayer transfer integral, is considerably higher than the transport scattering rate τ^{-1} , the electron transport is fully coherent and can be adequately described within the anisotropic three-dimensional (3D) Fermi liquid model. In the other limit, $t_{\perp}/\hbar \ll \tau^{-1}$, the successive interlayer hopping events are uncorrelated; thus the electron momentum and the Fermi surface can only be defined in the plane of the layers. Here one should distinguish between two different transport regimes. In the *strongly* incoherent regime there is no interference between the electron wave functions on adjacent layers and the interlayer hopping is entirely caused by scattering processes. Consequently, the temperature dependent resistivity across the layers, $\rho_{\perp}(T)$, is nonmetallic. On the other hand, one can consider the case of a weak overlap of the wave functions on adjacent layers, so that the interlayer transport is mostly determined by one particle tunneling. In this *weakly* incoherent transport the theory predicts the transverse resistivity ρ_{\perp} to be almost identical to that in the coherent case, sharing with the latter the metallic temperature dependence and most of high-field magnetotransport features [1, 2]. Thus the question arises: is there a substantial physical difference between the coherent and weakly incoherent interlayer transport regimes?

Moses and McKenzie [1] proposed to use the angle-dependent interlayer magnetoresistance to distinguish between the two cases: When the field is turned in a plane normal to the layers, a narrow peak is often observed at the orientations nearly parallel to the layers [5]. This *coherence peak* is caused by a topological change of electron orbits on a three-dimensional (3D) Fermi surface slightly warped in the direction perpendicular to the layers and can only exist in the coherent regime. Its absence in the weakly incoherent transport model [1, 2] is a natural consequence of the assumed strictly 2D Fermi surface.

Here, we report on a direct experimental comparison of the angle-dependent interlayer magnetoresistance in the coherent and weakly incoherent regimes. For the experiments several crystals of α -(BEDT-TTF)₂KHg(SCN)₄ being characterized by different sample quality have been used. This compound is known as one of the most anisotropic organic conductors. The conducting system of α -(BEDT-TTF)₂KHg(SCN)₄ comprises two bands, quasi-1D and quasi-2D. The former is subject to the nesting instability resulting in a charge-density-wave (CDW) transition at ≈ 8 K [6]. The other, quasi-2D band remains metallic. The extremely weak interlayer coupling gives the hope to realize either the coherent or incoherent interlayer transport regimes by selecting a sample with an appropriate electron scattering rate.

Fig. 1 shows the dependence of the interlayer resistance of two different samples on the magnetic field orientation. The latter is defined by the polar angle θ between the field direction and the normal to the plane of the layers, and by the azimuthal angle φ , as shown in the inset in

¹In collaboration with S. Simonov, ISSP, Chernogolovka, Russia, and I. Sheikin, GHMFL, Grenoble, France,

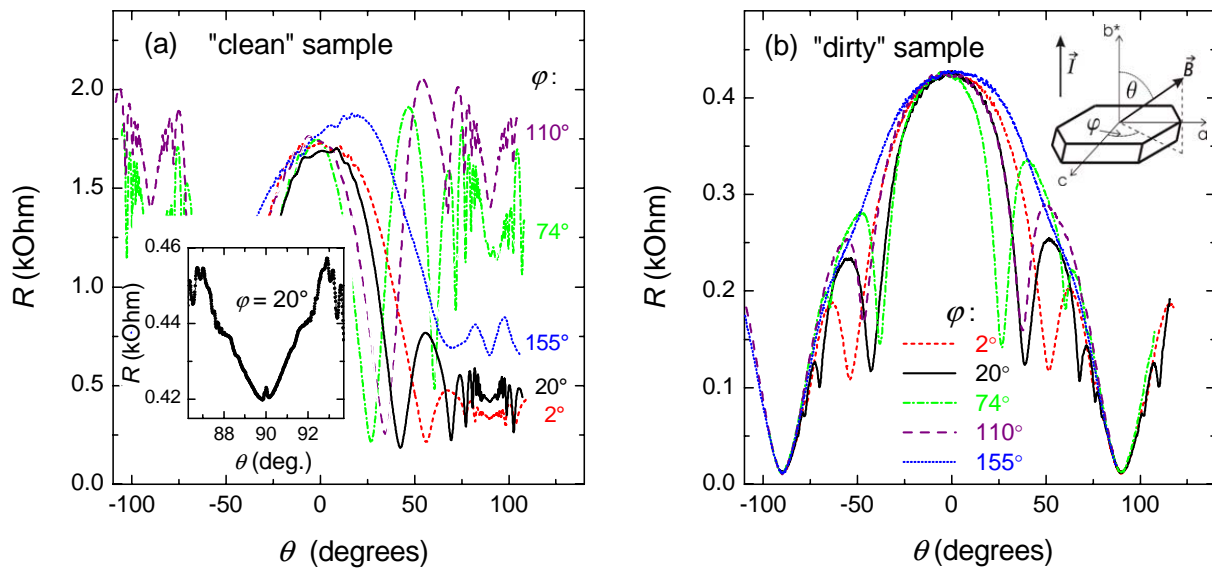


Figure 1: Interlayer resistance of two crystals of α -(BEDT-TTF) $_2$ KHg(SCN) $_4$ as a function of the polar angle θ recorded at different azimuthal angles φ , at $B = 10$ T. Insets: (left panel) details of a θ -sweep for the "clean" sample, showing the small coherence peak; (right panel) geometry of the experiment.

Fig. 1b. The most obvious feature is a series of sharp dips in the magnetoresistance. These well known angular magnetoresistance oscillations (AMRO) originate from the motion of the quasi-2D carriers in k -space along open orbits on the Fermi surface reconstructed by the CDW potential [7]. However, our present interest is the behavior of the non-oscillating background magnetoresistance which turns out to be drastically different in the two samples.

The behavior of the "clean" sample (Fig. 1a) is typical of a highly anisotropic 3D Fermi liquid. In particular, the rather strong φ -dependence (angles defined in the inset of Fig. 1b) of the resistance with the field parallel to the layers ($\theta = 90^\circ$) is directly related to the in-plane curvature of the Fermi surface. Further, a detailed inspection of the θ -dependence around $\theta = 90^\circ$ reveals a very narrow peak as shown in the inset in Fig. 1a. The width of this *coherence* peak, $\Delta\theta \approx 0.3^\circ$ yields an extremely low interlayer transfer integral: $t_\perp \simeq 0.03$ meV. For the "dirty" sample, represented in Fig. 1b, no coherence peak has been found at any φ that indicates the breakdown of the interlayer coherence. On the other hand, the presence of the AMRO and the metallic temperature dependence $R(T)$ is characteristic of the *weakly* rather than *strongly* incoherent interlayer transport regime.

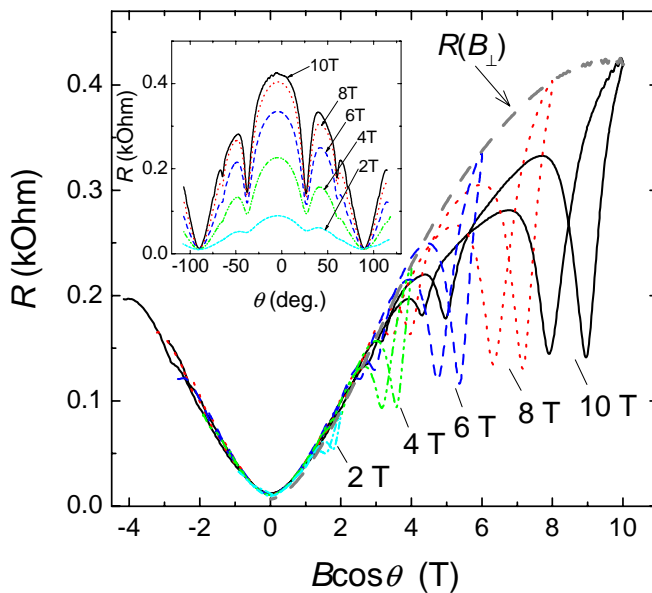


Figure 2: Magnetoresistance of the "dirty" sample as a function of the out-of-plane field component. Inset: the raw θ -sweeps recorded at different field strengths.

The most obvious distinction of the "dirty" sample is the behavior of the nonoscillating resistance background: the latter continuously decreases, as the field approaches a direction parallel

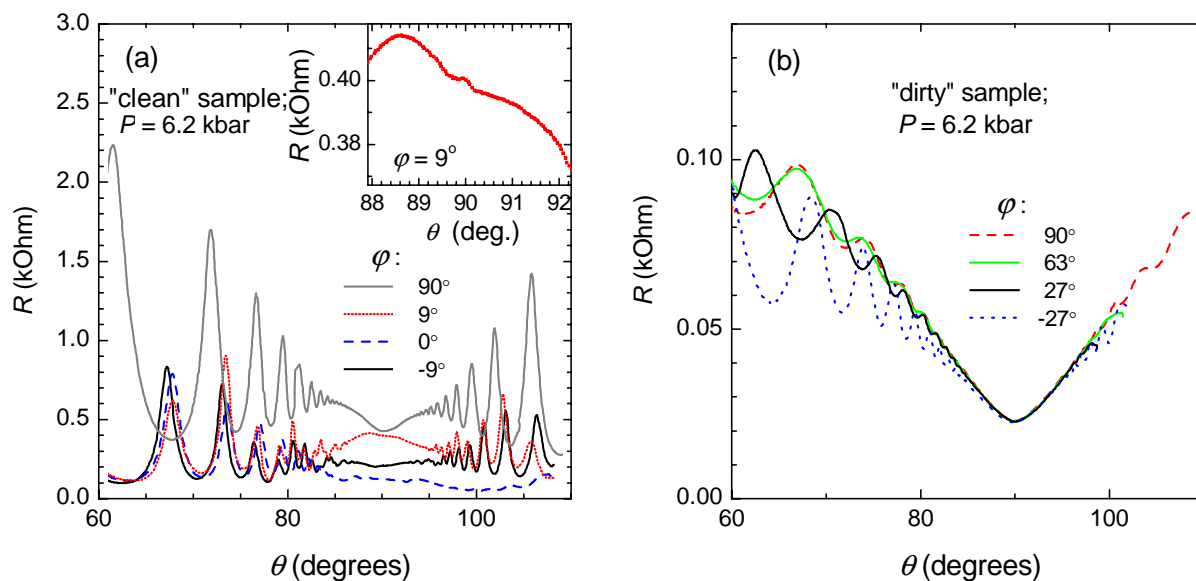


Figure 3: Angle-dependent magnetoresistance of the pressurized (a) "clean" and (b) "dirty" sample; $P = 6.2$ kbar, $B = 20$ T. Inset: fragment of the $\varphi = 9^\circ$ curve for the "clean" sample with the coherence peak.

to the layers, and is basically independent of the azimuthal orientation. Moreover, its angular dependence can be nicely scaled by a function of only the out-of-plane component of the magnetic field. This is illustrated by Fig. 2 where several θ -sweeps recorded at different field values are replotted as a function of $B_\perp = B \cos \theta$.

The results above were obtained at zero pressure, in the partially metallic CDW state. To verify that the drastic difference in the behavior of the "clean" and "dirty" samples is related to the metallic magnetotransport and not to some specific features of the CDW state, we have performed measurements under high pressure at which the whole material is entirely normal metallic.

Examples of the θ -sweeps recorded for "clean" and "dirty" samples at the pressure of 6.2 kbar are shown in Fig. 3. The Fermi surface and, therefore, the electron orbit topology are different from those at zero pressure. This is, in particular, reflected in the AMRO behavior [8]: now the oscillations are mostly determined by closed orbits on the cylindrical Fermi surface. Despite the radical modification of the magnetoresistance behavior upon applying pressure, the major differences between the "clean" and "dirty" samples remain the same as in the zero-pressure state. The "clean" sample exhibits a small narrow peak around $\theta = 90^\circ$ (see the inset in Fig. 2a) and a strong dependence on the azimuthal orientation φ . By contrast, the "dirty" sample shows a broad dip, centered at $\theta = 90^\circ$ and insensitive to φ , and no coherence peak.

Thus, we conclude that the non-oscillating magnetoresistance component of the "dirty" sample is essentially a function of only the field component perpendicular to the layers. Remarkably, this behavior is found in both the zero- and high-pressure states, characterized by different Fermi surface geometries.

This is a surprising and somehow counterintuitive result. Normally, an in-plane magnetic field acts to confine charge carriers to the layers, thus increasing the interlayer resistivity. The theory predicts a strong linear or superlinear magnetoresistance in strong fields parallel to the layers, both in the coherent [9] and in the weakly incoherent [1] regimes. The exact field dependence is determined by the Fermi surface geometry. Since the latter is generally anisotropic in the plane of the layers, the magnetoresistance strongly depends on the azimuthal orientation of

the field [9]. While the “clean” sample is in good agreement with the predictions for the coherent transport, this is not the case for the weakly incoherent regime, as follows from the data on the “dirty” sample. The fact that its resistance is insensitive to the in-plane field is clearly in conflict with the model predictions, thus urging a considerable revision of the weakly incoherent interlayer transport theory.

References

- [1] R. H. McKenzie and P. Moses, *Phys. Rev. Lett.* **81**, 4492 (1998); P. Moses and R. H. McKenzie, *Phys. Rev. B* **60**, 7998 (1999).
- [2] T. Osada, *Physica E* **12**, 272 (2002); T. Osada and M. Kuraguchi, *Synth. Met.* **133-134**, 75 (2003).
- [3] J. Wosnitzer, J. Hagel, J. S. Qualls, J. S. Brooks, E. Balthes, D. Schweitzer, J. A. Schlueter, U. Geiser, J. Mohtasham, R. W. Winter, and G. L. Gard, *Phys. Rev. B* **65**, 180506(R) (2002).
- [4] N. E. Hussey, M. Abdel-Jawad, A. Carrington, A. P. Mackenzie, and L. Balicas, *Nature* **425**, 814 (2003).
- [5] M. V. Kartsovnik, *Chem. Rev.* **104**, 5737 (2004).
- [6] D. Andres, M. V. Kartsovnik, W. Biberacher, H. Weiss, E. Balthes, H. Müller, and N.D. Kushch, *Phys. Rev. B* **64**, 161104(R) (2001).
- [7] M. V. Kartsovnik, A. E. Kovalev, and N. D. Kushch, *J. Phys. I* **3**, 1187 (1993).
- [8] N. Hanasaki, S. Kagoshima, N. Miura, and G. Saito, *Phys. Rev. B* **65**, 1010 (1996).
- [9] A. G. Lebed and N. N. Bagmet, *Phys. Rev. B* **55**, R8654 (1997); V. G. Peschansky, *Low Temp. Phys.* **23**, 35 (1997).

Field-induced Charge-Density-Wave Transitions

D. Andres, M. V. Kartsovnik, W. Biberacher, K. Neumaier

In the layered organic metal α -(BEDT-TTF)₂KHg(SCN)₄ there exists a charge-density-wave (CDW) state below 8 K at ambient pressure [1]. A quasi-one-dimensional (Q1D) electron band becomes completely gapped at the Fermi level, due to the so-called nesting of the Fermi surface, while the other, quasi-two-dimensional (Q2D) band still leads to metallic behavior of the system. However, the cylinders on the Fermi surface of the Q2D band turn into strongly warped open sheets due to the additional periodic potential of the density wave [2]. Further, it is known that hydrostatic pressure can easily tune the nesting conditions of the present compound [1]. This means that hydrostatic pressure deteriorates the nesting conditions and even leads to a complete suppression of the density wave at $P_0 \approx 2.5$ kbar [1, 3]. Remarkably, in this system there exists a stimulating orbital effect of the magnetic field which becomes stronger on deteriorating the nesting conditions. Under hydrostatic pressure, it therefore becomes possible that the CDW transition temperature increases with magnetic field [1], before the suppression by the additional, Pauli paramagnetic effect sets in. In this work, we show that this orbital effect stabilizes the CDW, even when the latter is already completely suppressed at zero field.

We have performed standard four point measurements of the interlayer resistance under pressure down to 20 mK. The pressure cell was mounted on a dilution refrigerator, the sample being at a fixed position with respect to the magnetic field during the measurements. The magnetic field was oriented perpendicular to the conducting planes. The pressure value at low temperatures was determined from the resistance of a calibrated Manganin coil to an accuracy of better than ± 100 bar.

The critical pressure P_0 , at which the density-wave transition temperature at zero field becomes 0 K has been determined as 2.5 ± 0.1 kbar [1, 3]. Above P_0 we expect the CDW state only to become stabilized via the orbital effect of magnetic field. Fig. 1 shows magnetic field sweeps, with the field oriented perpendicular to the conducting plane, up to 15 T at 100 mK for different pressures covering the whole pressure range investigated within this work. The data presented in Fig. 1 are obtained on the same sample and have been qualitatively reproduced on another one measured at the same time. Since the pressures were applied successively, i.e., without opening the clamp cell, the magnetic field orientation is exactly the same for each pressure.

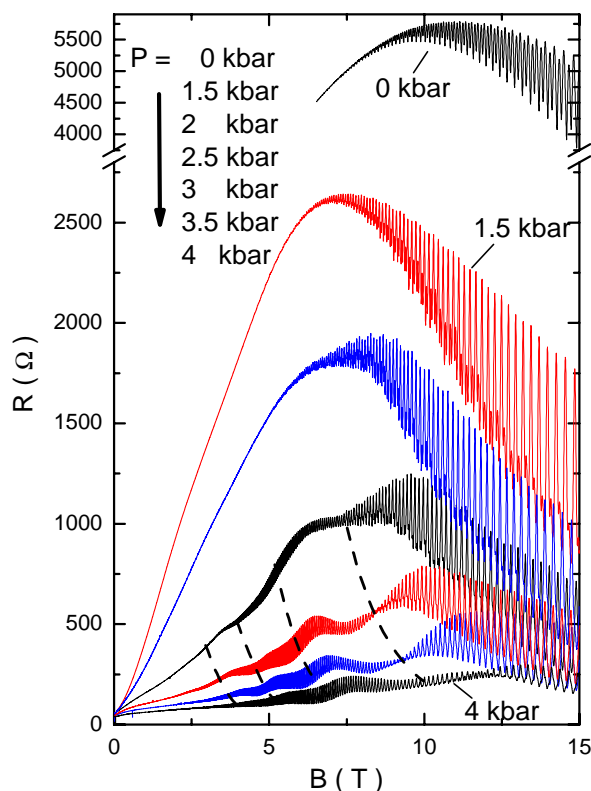


Figure 1: Magnetoresistance at various pressures at 100 mK. Above $P_0 \approx 2.5$ kbar slow oscillations appear in the background magnetoresistance. With pressure these oscillations gradually move to higher fields as visualized by dashed lines.

One of the basic characteristics of the ambient-pressure CDW state of this compound is the strong magnetoresistance, most likely caused by geometrical effects of the Fermi surface [2, 4]. At approximately 11 T the magnetoresistance has a maximum followed by a negative slope that is interpreted to arise from magnetic breakdown [4] between the strongly warped open sheets of the Fermi surface. The breakdown leads to fast Shubnikov-de Haas (SdH) oscillations at the frequency $F_\alpha = 670$ T. Additional SdH frequencies at $F_\lambda = 170$ T and $F_\nu = F_\alpha + F_\lambda$ present only in the CDW state were observed earlier [2] and remain a subject of speculations.

As shown in Fig. 1, the strong semiclassical magnetoresistance decreases with pressure indicating the gradual suppression of the CDW energy gap. Besides this, the curves show other pressure-induced changes, in particular on crossing the critical pressure P_0 . Most significantly, at pressures $P \gtrsim P_0$ slow oscillations with the frequency $F_{\text{slow}} \sim 20$ T emerge. With increasing pressure these oscillations gradually move up in field as visualized by the dashed lines in Fig. 1.

Another distinct change on crossing the critical pressure is the field at which the fast oscillations start to become visible. While at $P < P_0$ the oscillations appear at rather high fields, shortly before the magnetoresistance background reaches the maximum, i.e. 5-8 T, they already start below 2 T at $P > P_0$. This is directly seen in Fig. 2, where the field sweeps around 2 T are shown in an enlarged field scale at pressures above and below 2.5 kbar. This observation directly shows the absence of the density wave in low fields above the critical pressure: since in the normal metallic state there are cylinders on the Fermi surface it becomes understandable why the α -oscillations start at such low fields (see Fig. 2).

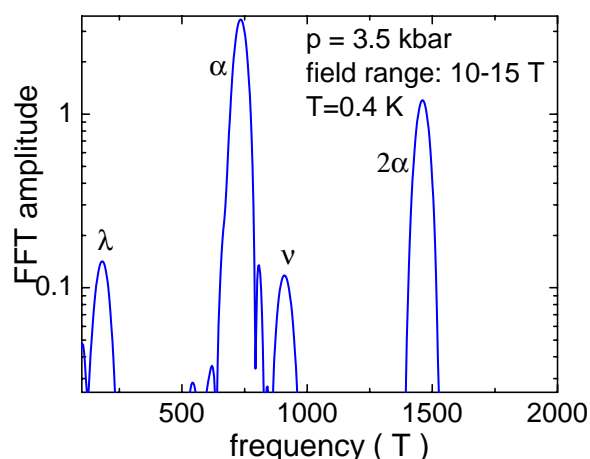


Figure 3: FFT spectrum of the field sweep at 100 mK and $P = 3.5$ kbar in the field interval 10-15 T. The additional frequencies λ and ν within the field-induced CDW state are clearly resolved.

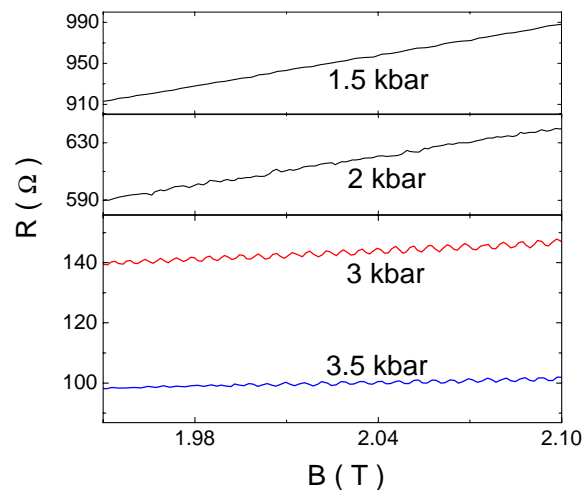


Figure 2: Enlarged low field parts of Fig. 1. Above 2.5 kbar the fast oscillations start to appear already below 2 T, at 100 mK.

The presence of the CDW state at higher fields and at $P > P_0$ is directly reflected in its distinct properties: First, in the field range of 10-15 T the additional SdH frequencies at F_λ and F_ν , characteristic of the CDW state, remain. An example of the Fast-Fourier-Transformation (FFT) spectrum of the magnetoresistance at 3.5 kbar is given in Fig. 3. Second, there is a broad hysteresis observed on sweeping the magnetic field up and down. An example at 3 kbar is given in Fig. 4. To determine the hysteresis, the fast oscillations were filtered out from these curves. Such a hysteresis is definitely at odds with normal metallic behavior and is known to be present in the CDW state of this compound [5]. Third, angle-dependent magnetoresistance oscillations were found to show clear signs of the CDW state at $P > P_0$ [6]. Alto-

gether, the re-entrance to the CDW state in magnetic field is thus clearly seen in the magnetoresistance data.

The slow oscillations appear only in the pressure region in which the density wave does not exist anymore at zero field. Moreover, a structure in the hysteresis ΔR is observed that correlates with the slow oscillations. As can be seen in Fig. 4 there are clear peaks in ΔR at approximately the same fields where the background resistance has maximal curvature.

From the above results, we conclude that these slow oscillations are indicative of successive field-induced CDW (FICDW) transitions. Qualitatively, these transitions emerge if the nesting conditions of the Fermi surface become so bad that free carriers start reappearing on the 1D sheets of the Fermi surface [7]. Under these conditions, the quantization of the electron motion in a magnetic field is predicted to cause a series of first order transitions between CDW states with quantized wave vectors [8, 9]. The pressure and temperature range, at which the slow oscillations are observed in our compound, as well as the hysteresis structure very well match the theoretical predictions for the FICDW phenomenon.

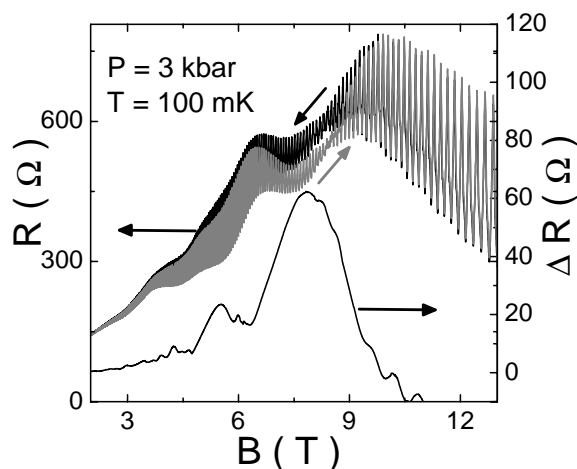


Figure 4: Up (grey) and down (black) field sweeps of the magnetoresistance at $P = 3$ kbar and $T = 100$ mK. The hysteresis, shown below, is observed by subtracting one curve from the other. A clear structure in the hysteresis correlating with the slow oscillation can be seen.

References

- [1] D. Andres, M. V. Kartsovnik, W. Biberacher, H. Weiss, E. Balthes, H. Müller, and N. Kushch, *Phys. Rev. B* **64**, 161104(R) (2001).
- [2] M. V. Kartsovnik, A. E. Kovalev, and N. D. Kushch, *J. Phys. I France* **3**, 1187 (1993).
- [3] D. Andres, M. Kartsovnik, W. Biberacher, K. Neumaier, E. Schuberth, and H. Müller, *Phys. Rev. B* **72**, 174513 (2005).
- [4] R. H. McKenzie, G. J. Athas, J. S. Brooks, R. G. Clark, A. S. Dzurak, R. Newbury, R. P. Starrett, A. Skougarevsky, M. Tokumoto, N. Kinoshita, T. Kinoshita, and Y. Tanaka, *Phys. Rev. B* **54**, 8289(R) (1996).
- [5] T. Osada, R. Yagi, A. Kawasumi, S. Kagoshima, N. Miura, M. Oshima, and G. Saito, *Phys. Rev. B* **41**, 5428 (1990).
- [6] see D. Andres, M. V. Kartsovnik, and W. Biberacher, WMI Annual report, 2004.
- [7] T. Ishiguro, K. Yamaji, and G. Saito, *Organic Superconductors*, 2nd edition, Springer-Verlag, Berlin, Heidelberg (1998).
- [8] D. Zanchi, A. Bjelis, and G. Montambaux, *Phys. Rev. B* **53**, 1240 (1996).
- [9] A. G. Lebed, *JETP Lett.* **78**, 138 (2003).

Low-frequency $1/f$ -Noise in LSMO:MgO Nanocomposite Films

A. Marx, R. Gross

M. Esseling, V. Moshnyaga, K. Samwer¹

Nanocomposite manganite films have attained considerable interest recently because they show very interesting physical properties and can be much more easily fabricated compared to layered thin film hetero-structures. However, grain boundaries between individual grains and the quality of interfaces separating different phases have significant influence on the electrical transport properties of these materials [1]. For epitaxial manganite thin films with individual well-defined grain boundaries it has been shown that the grain boundaries strongly modify the electrical transport and noise properties. In the $(\text{La}_{0.7}\text{Sr}_{0.3}\text{MnO}_3)_{0.95}:(\text{MgO})_{0.05}$ -system (LSMO:MgO) a large low-field magnetoresistance effect has been found, which is most likely due to a chemical phase separation of the ferromagnetic metallic manganite and the insulating MgO, which embeds individual LSMO grains [2]. In this system the electronic transport is dominated by spin polarized tunneling of electrons across the MgO-barrier, which in turn is extremely sensitive to the quality and microstructure of the involved interfaces/tunneling barrier. Since low-frequency $1/f$ -noise is known to be very sensitive to interface properties, the investigation of $1/f$ noise is a powerful tool to characterize the interfaces and tunneling barriers in these nanocomposite films. Furthermore, with respect to sensor applications it is important to determine the amount and origin of low-frequency noise is important

We have performed extensive $1/f$ noise measurements on LSMO:MgO nanocomposite films prepared by means of metal-organic aerosol deposition (MAD) technique [3] on (0001)-oriented sapphire. TEM measurements give evidence that the grain-boundaries between individual LSMO grains are filled with MgO. Therefore, the MgO interlayers are expected to act as insulating tunnel barriers. The noise measurements were taken in a magnetically shielded cryostat with an optical heating system [4] to minimize the background noise level.

Figure 1 shows typical noise spectra measured at $T = 25\text{ K}$ and $H = 0\text{ Oe}$ for different values of current bias.

The spectra reveal a $1/f^\alpha$ frequency dependence over more than three decades of frequency within the whole temperature and magnetic field range. S_V was found to scale with the sample resistance which can be modified by an external magnetic field at constant bias current. The frequency independent parameter

$$a_V = \frac{\gamma}{n} = S_V \frac{\Omega \cdot f^\alpha}{V^2} \quad (1)$$

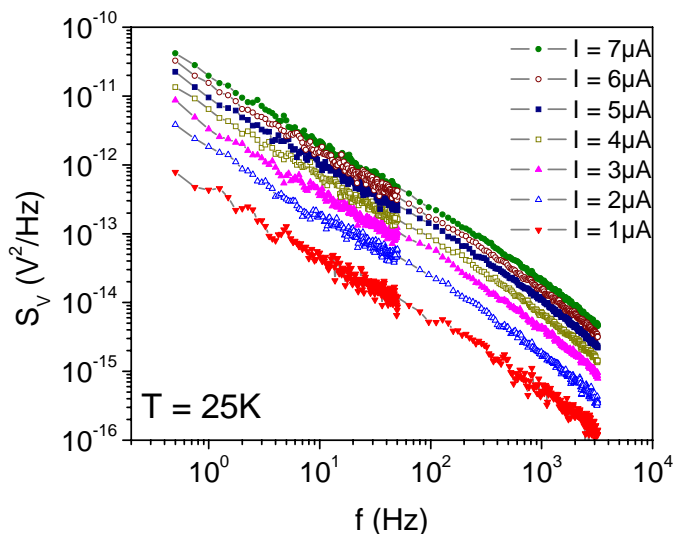


Figure 1: Typical voltage noise spectral densities corrected for the zero-bias current background at $T = 25\text{ K}$ and $H = 0\text{ Oe}$ measured at different bias currents.

¹I. Physikalisches Institut, Georg-August-Universität Göttingen, Friedrich-Hund-Platz 1, D-37077 Göttingen, Germany

is used to characterize the temperature and magnetic field dependence of the voltage noise data. Here, γ is the Hooge parameter [5], n the charge carrier density, Ω the sample volume and α the exponent derived by fitting the spectral power density $1/f^\alpha$ dependence.

Figure 2a shows the frequency averaged value $\langle a_V \rangle$ determined in the frequency range $10 \text{ Hz} \leq f \leq 20 \text{ Hz}$ at $T = 100 \text{ K}$ and $I_b = 5 \mu\text{A}$ as a function of the external magnetic field. Within the experimental error no significant magnetic field dependence is observable. This behavior is representative for all measurements within the temperature and bias current range investigated. Therefore, the normalized noise $\langle a_V \rangle$ in this system can be considered to be independent of the bias current and the external magnetic field, although the resistance is strongly depending on the magnetic field (TMR-effect).

Assuming that the $1/f$ noise is predominantly caused in the MgO tunnel barriers the magnetic field independence of the normalized noise indicates that there are no magnetic impurities in the barriers which are involved in the charge transport process [6]. Magnetic domain wall motion can also be excluded as source of the voltage noise, since the sample is fully magnetized for $H = \pm 1026 \text{ Oe}$.

The temperature dependence of $\langle a_V \rangle$ measured at the applied field $H = 1026 \text{ Oe}$ and $I_b = 5 \mu\text{A}$ is shown in Fig. 2b. The noise level shows a clear maximum between $T = 10 \text{ K}$ and $T = 25 \text{ K}$ and decreases at higher temperatures. No obvious connection to the temperature dependence of the resistance can be deduced. In this temperature range the onset of the electronic phase separation of the manganite takes place, which probably influences the temperature dependence of the normalized noise. Nevertheless, the temperature dependence of the noise is rather weak.

The magnitude of the normalized noise $\langle a_V \rangle \approx 10^{-27} \text{ m}^3$ is comparable to the values found for high quality epitaxial $\text{La}_{2/3}\text{Ca}_{1/3}\text{MnO}_3$ films grown on SrTiO_3 - or NdGaO_3 -substrates [7]. The manganite films grown on SrTiO_3 are highly strained and show a higher noise level as the unstrained films grown on NdGaO_3 . This result illustrates the tremendous influence of the effect of local strain in the epitaxial films on the $1/f$ noise properties. The fact that the noise level of the nanocomposite film lies between the values for the strained and unstrained films, respectively, indicates the good quality of the LSMO:MgO nanocomposite film and of the LSMO/MgO interfaces. Furthermore, our detailed noise analysis provides no evidence for a structurally distorted region at the LSMO/MgO interface.

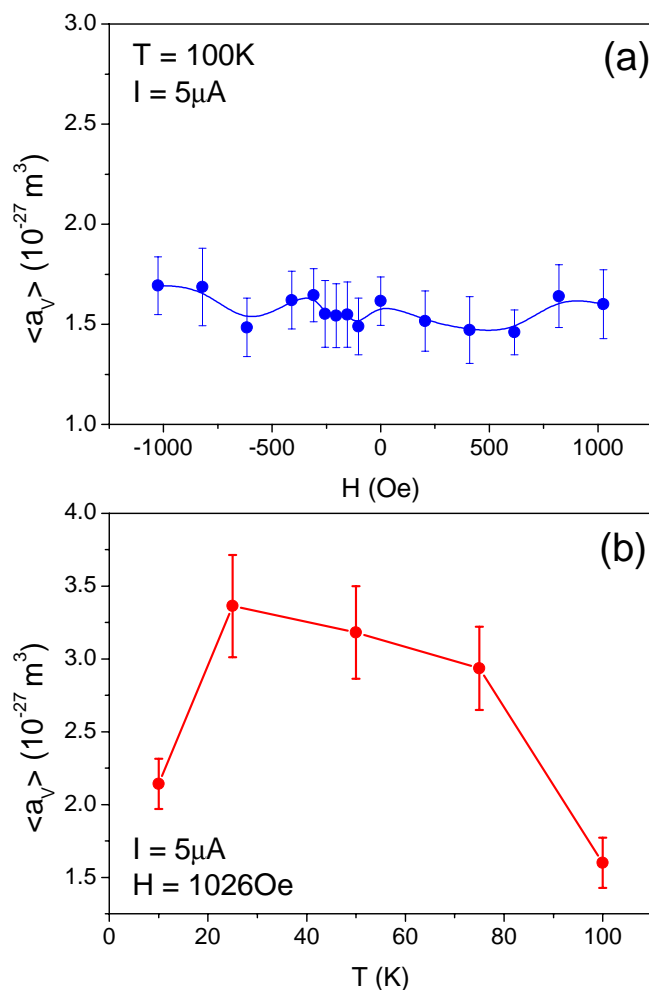


Figure 2: (a) Magnetic field dependence at 100 K and (b) temperature dependence in a field of 1026 Oe of $\langle a_V \rangle$ measured at $I_b = 5 \mu\text{A}$ in the range $10 \text{ Hz} \leq f \leq 20 \text{ Hz}$.

References

- [1] R. Gross, L. Alff, B. Büchner, B. H. Freitag, C. Höfener, J. Klein, Yafeng Lu, W. Mader, J. B. Philipp, M. S. R. Rao, P. Reutler, S. Ritter, S. Thienhaus, S. Uhlenbruck, *J. Magn. and Magn. Mat.* **211**, 150 (2000).
- [2] S. A. Köster, V. Moshnyaga, K. Samwer, O. I. Lebedev, G. van Tendeloo, O. Shapoval and A. Belenchuk, *Appl. Phys. Lett.* **81**, 1648 (2002).
- [3] V. Moshnyaga, I. Khoroshun, A. Sidorenko, P. Petrenko, A. Weidinger, M. Zeitler, B. Rauschenbach, R. Tidecks and K. Samwer, *Appl. Phys. Lett.* **74**, 2842 (1999).
- [4] A. Marx, U. Fath, W. Ludwig, R. Gross, and T. Amrein, *Phys. Rev. B* **51**, 6735 (1995).
- [5] S. Kogan, *Electronic Noise and Fluctuations in Solids*, (University Press, Cambridge, 1996).
- [6] J. B. Philipp, L. Alff, A. Marx and R. Gross, *Phys. Rev. B* **66**, 224417 (2002).
- [7] P. Reutler, A. Bensaid, F. Herbstritt, C. Höfener, A. Marx, and R. Gross, *Phys. Rev. B* **62**, 11619 (2000).

Magnetic Polarization of Re in the Double Perovskite $\text{Sr}_2\text{CrReO}_6$

P. Majewski, S. Geprägs, O. Sanganas, M. Opel, L. Alff,¹ F. Wilhelm², A. Rogalev,² and R. Gross³

The ferrimagnetic double perovskites have high Curie temperature well above room temperature and are predicted to have full spin polarization of the charge carriers at the Fermi level. Therefore, they are currently considered as promising materials for spintronics applications. Within the materials class of the ferrimagnetic double perovskites, the compound $\text{Sr}_2\text{CrReO}_6$ with the Curie temperature $T_C \simeq 635$ K has the highest transition temperature observed so far [1, 2, 3]. The magnetic exchange resulting in this high ordering temperature is believed to be kinetic energy driven in the spin down channel. According to a generalized double exchange model a considerable magnetic moment is induced on the non-magnetic site (Re in this case), which is oriented anti-parallel to the local moments on the magnetic sites (Cr in this case). For the compound $\text{Sr}_2\text{CrReO}_6$ a high spin magnetic moment of $-0.69\mu_B$ was predicted by recent bandstructure calculations based on the full-potential linear muffin-tin orbital method (FP-LMTO) using local spin density approximation (LSDA) [4]. A considerable orbital magnetic moment on Re was also predicted indicating the relevance of spin-orbit coupling, which leads, in turn, to a breakdown of the complete half-metallicity of $\text{Sr}_2\text{CrReO}_6$. Therefore, this material has to be considered as a *pseudo*-half-metal. In order to check these predictions the magnitude and the direction of the local moment on the Re site has to be measured. This can be done in an ideal way by a combination of X-ray Magnetic Circular Dichroism (XMCD) and SQUID magnetometry.

As a continuation of our XMCD study on the ferrimagnetic double perovskites (see [5]), where we probed the induced magnetic moment at the W-site in the double perovskites Sr_2CrWO_6 and Ca_2CrWO_6 [6], we investigated the induced moment at the Re-site in the compound $\text{Sr}_2\text{CrReO}_6$. Here, we are reporting on our XMCD study of the Re 5d moment in polycrystalline bulk samples supplemented by SQUID (superconducting quantum interference device) magnetization measurements of the same sample [7]. These measurements together with our previous study on other double perovskites give conclusive evidence that the Curie temperature T_C in the ferrimagnetic double perovskites of the form $A_2BB'O_6$ with A an alkaline earth, B a magnetic ion, and B' a non-magnetic 3d or 5d ion strongly depends on the induced magnetic moment at the originally non-magnetic B' site.

The measurements were done at the European Synchrotron Radiation Facility (ESRF) in Grenoble at the beam line ID12 [8]. XANES (x-ray absorption near-edge spectroscopy) spectra were recorded using the highly efficient total fluorescence yield detection method. As for a magnetic element the absorption due to the selection rules is dependent on the helicity of the circular polarized x-ray beam, the magnetic moment can be determined with XMCD spectra. The magnetic moment is determined from the difference between consecutive XANES scans recorded with opposite helicities of the incoming x-ray beam. To ensure that the XMCD spectra are free from experimental artefacts the data were collected for both directions of the applied magnetic field of 6 T (parallel and antiparallel to the x-ray beam).

The preparation of the polycrystalline bulk samples is described in detail in [7]. The XANES and XMCD measurements were performed at the $L_{2,3}$ edges of Re at about 10 K. Since the

¹TU Darmstadt, Petersenstr. 23, 64287 Darmstadt, Germany.

²ESRF, 6 Rue Jules Horowitz, Boîte Postale 220, 38043 Grenoble Cedex 9, France.

³This work is supported by the BMBF (project No.: 13N8279), the German Science Foundation (project No.: GR 1132/13) and the ESRF (HE-1882).

sample measured in backscattering geometry was very thick, the spectra were corrected for self-absorption effects. The edge jump ratio L_3/L_2 was normalized to 2.20/1 [9]. This takes into account the difference in the radial matrix elements of the $2p_{1/2}$ to $5d(L_2)$ and $2p_{3/2}$ to $5d(L_3)$ transitions.

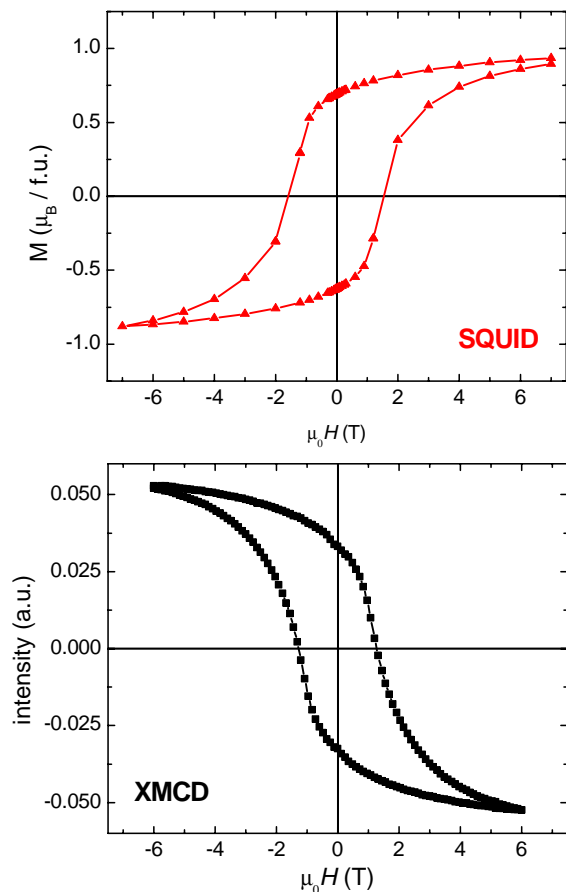


Figure 1: SQUID and XMCD data of $\text{Sr}_2\text{CrReO}_6$. Upper panel: Magnetization versus applied magnetic field measured by SQUID at $T = 5\text{K}$. Lower panel: XMCD signal versus applied magnetic field for the same sample at the Re L_2 edge at $T \approx 10\text{K}$.

Fig. 1 shows a direct comparison of the SQUID and XMCD measurements. The total magnetization of the sample was measured by SQUID magnetometry (upper panel), whereas the XMCD measurement (lower panel) was performed at the Re L_2 edge and shows the local magnetic moment at the Re site. It is obvious from the comparison, that the magnetic moments of Cr^{3+} (B ion) and Re^{5+} (B' ion) are coupled antiferromagnetically. This result is consistent with that obtained for Cr^{3+} and W^{5+} in Sr_2CrWO_6 and Ca_2CrWO_6 [6].

We calculated the spin and orbital moment at the Re 5d shell from the XMCD measurements at the Re $L_{2,3}$ edges, using the magneto-optical sum rules [10, 11]. According to bandstructure calculations we use $n_h = 5.3$ as the number of 5d holes [12]. The spin magnetic moment of $m_s(\text{exp}) = -0.68\mu_B$ matches nicely with the theoretically predicted value of $m_s(\text{th}) = -0.69\mu_B$ [4]. This result as well as other currently published data is summarized in Table 1.

In Fig. 2 the spin magnetic moment m_s on the B' site of various double perovskites presented in Table 1 is plotted versus the Curie temperature of these materials. The data suggests, that T_C scales with m_s at the B' site. Of course, we cannot draw final conclusions from this comparison, as other factors such as structure, hybridization and site occupation can significantly influence T_C [3, 14]. However, there is a clear trend that a large T_C is accompanied by a large induced spin magnetic moment m_s at the B' site. This finding is in qualitative agreement with

Table 1: Summary of the spin and orbital magnetic moments, m_s and m_L , at the 'non-magnetic' ion Re in $\text{Sr}_2\text{CrReO}_6$ ($T_C = 635\text{K}$) measured by XMCD using $n_h = 5.3$, as well as calculated values with FP-LMTO-LSDA are shown. For comparison, published experimental data for other double perovskite materials are also shown.

		m_s (μ_B/atom)	m_L (μ_B/atom)	$ m_L/m_s $
$\text{Sr}_2\text{CrReO}_6$	experiment	-0.68	0.25	0.37
$\text{Sr}_2\text{CrReO}_6$	theory [4]	-0.69	0.17	0.25
Ca_2CrWO_6	[6]	-0.22	0.10	0.44
Sr_2CrWO_6	[6]	-0.33	0.12	0.35
$\text{Sr}_2\text{FeMoO}_6$	[13]	-0.32	-0.05	0.15

the generalized double exchange model for double perovskites [15], where the ferrimagnetism is assumed to be mediated by itinerant minority spin carriers. We emphasize that T_C seems not to depend on the total spin moment given by the sum of the local moment on the magnetic B site (Cr, Fe) and the induced magnetic moment on the non-magnetic B' site (Mo, W, Re). If this would be the case, different T_C values would be expected for the Cr and Fe based double perovskites in contrast to the experimental data.

In summary, we have unambiguously demonstrated a large spin magnetic moment at the Re $5d$ site in the ferrimagnetic double perovskite $\text{Sr}_2\text{CrReO}_6$ together with a considerable orbital magnetic moment. This result together with data from literature suggest that the critical temperature for such double perovskites scales with the magnetic moment at the 'non-magnetic' site of the compound. The data is in fair agreement with the model prediction and is important for understanding the mechanism of the high Curie temperatures in the ferrimagnetic double perovskites.

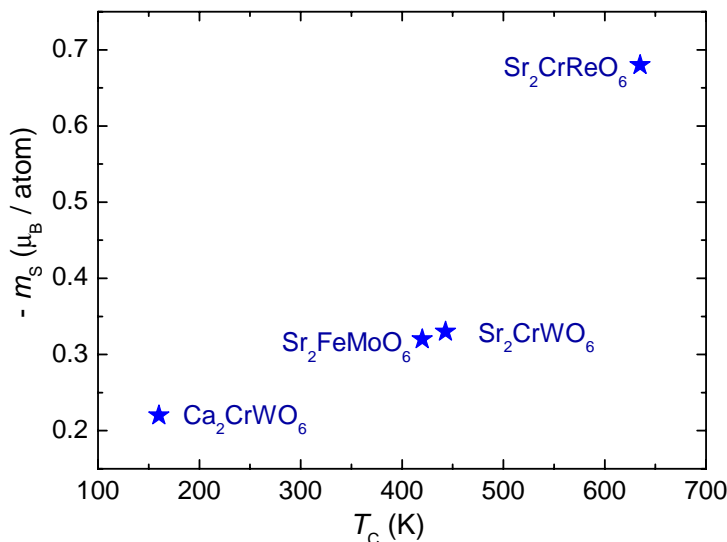


Figure 2: B' spin magnetic moments for different double perovskites $A_2BB'O_6$ determined by XMCD on Mo [13] together with our data on W [6] and Re. The number of $5d$ holes has been obtained from recent band-structure calculations [4, 6, 12].

References

- [1] H. Kato, T. Okuda, Y. Okimoto, Y. Tomioka, Y. Takenoya, A. Ohkubo, M. Kawasaki, and Y. Tokura, *Appl. Phys. Lett.* **81**, 328 (2002).
- [2] H. Asano, N. Kozuka, A. Tsuzuki, and M. Matsui, *Appl. Phys. Lett.* **85**, 263 (2004).
- [3] H. Kato, T. Okuda, Y. Okimoto, Y. Tomioka, K. Oikawa, T. Kamiyama, and Y. Tokura, *Phys. Rev. B* **69**, 184412 (2004).
- [4] G. Vaitheeswaran, V. Kanchana, and A. Delin, *Appl. Phys. Lett.* **86**, 032513 (2005).
- [5] P. Majewski, S. Geprägs, A. Boger, A. Erb, M. Opel, L. Alff, and R. Gross, F. Wilhelm, and A. Rogalev, *Annual Report WML*, (2004)
- [6] P. Majewski, S. Geprägs, A. Boger, A. Erb, M. Opel, and R. Gross, G. Vaitheeswaran and V. Kanchana, A. Delin, F. Wilhelm, and A. Rogalev, L. Alff, *Phys. Rev. B* **72**, 132402 (2005)
- [7] P. Majewski, S. Geprägs, O. Sanganas, M. Opel, and R. Gross, F. Wilhelm, and A. Rogalev, L. Alff, *Appl. Phys. Lett.* **87**, 202503 (2005)
- [8] A. Rogalev, J. Goulon, Ch. Goulon-Ginet, and C. Malgrange, in *Magnetism and Synchrotron Radiation*, E. Beaurepaire *et al.* (Eds.), LNP vol. **565** (Springer, 2001).
- [9] B. L. Henke, E. M. Gullikson, and J. C. Davis, *At. Data Nucl. Data Tables* **54**, 181-342 (1993). Online available: <http://www-cxro.lbl.gov>. Using the Chantler tables (online available: <http://physics.nist.gov/ffast>) the results change by not more than $\pm 4\%$.
- [10] B.T. Thole, P. Carra, F. Sette, and G. van der Laan, *Phys. Rev. Lett.* **68**, 1943 (1992).
- [11] P. Carra, B.T. Thole, M. Altarelli, and X. Wang, *Phys. Rev. Lett.* **70**, 694 (1993).
- [12] A. Delin, G. Vaitheeswaran, V. Kanchana, private communication.
- [13] M. Besse, V. Cros, A. Garthélemy, H. Jaffrès, J. Vogel, F. Petroff, A. Mirone, A. Tagliaferri, P. Bencok, P. Decorse, P. Berthet, Z. Szotek, W. M. Temmerman, S. S. Dhesi, N. B. Brookes, A. Rogalev, and A. Fert, *Europhys. Lett.*, **(60)**, 608 (2002).
- [14] J. M. De Teresa, D. Serrate, J. Blasco, M. R. Ibarra, and L. Morellon, *Phys. Rev. B* **69**, 144401 (2004).
- [15] D. D. Sarma, E. V. Sampathkumaran, S. Ray, R. Nagarajan, S. Majumdar, A. Kumar, G. Nalini, T. N. G. Row, *Sol. State Comm.* **114**, 465 (2000)

Structure and Dynamics of Molecular Self-Organization

B. A. Hermann¹

Nature's engineering is based on self-organization and thus, so to speak, happens by itself. To some extent, even mistakes are tolerated. Employing self-organization for technical applications in molecular electronics, catalysis, sensor surfaces and surface coating, is mostly desired, because thickness, structure as well as defects in monolayers could be controlled, if the self-organization would work excellently. In the past, research on self-organization focused on studying small, flat and stiff molecules on controlled surfaces. Larger and flexible molecules where thought to be too difficult to be controlled, however, our recent scanning tunneling microscopy (STM) studies on larger and flexible molecules show even better self-organization properties, provided the molecules are designed well.

Conformational Segregation in Domains

In order to engineer molecules in a way that they show excellent self-organization properties, a fundamental understanding of self-organization has to be gained by basic research. We analyzed conformational (conformation = constellation of the molecule) segregation in domains of a flexible aromatic molecule. Solution casting of second-generation (second generation = the outer aromatic unit is repeated once resulting in a branched structure) Fréchet dendrons with bipyridine-central core (see Fig. 1a (1)) resulted in good quality monolayers in which multiple domains could be observed [1]. Fig. 1b depicts the STM image of two domains showing a slightly different arrangement of the rows and different internal structure of the molecules. For these images, an averaging analysis of the lower and upper domain in Fig. 1b was performed over 62 and 44 positions, respectively, allowing the identification of single molecules almost without

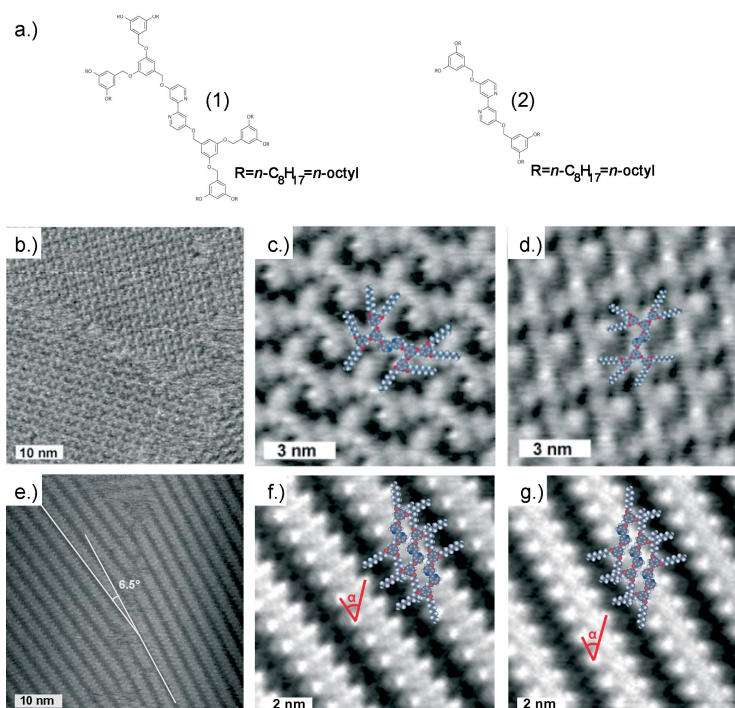


Figure 1: (a) Structural formulae of a (1) second and (2) first-generation 2,2'-bipyridine-based dendron (OR with R = n-octyl = n-C₈H₁₇). (b) STM images of two domains of monolayers of (1) on HOPG (50 nm x 50 nm) (c) and (d) expanded images (10 nm x 10 nm) of the lower and upper domains, respectively, of b ($U_{bias} = -1111$ mV, $|I_t| = 15$ pA). (e) STM images of two domains in a monolayer of (2) on HOPG (50 nm x 50 nm). The angle difference between the two domains is 6.5°. (f) and (g) Expanded images (10 nm x 10 nm) of e (left and right domain, respectively). ($U_{bias} = -1111$ mV, $|I_t| = 15$ pA). Further details in the text and in [1].

¹This research is conducted with L. Merz, my former Ph.D. student, in collaboration with Edwin Constable, Catherine Housecroft and Lukas Scherer of the Institute of Inorganic Chemistry, University of Basel. H. J. Güntherodt is gratefully acknowledged for hosting part of this research. The students and postdocs involved in this research in Basel are supported through the Swiss National Science Program NRP 47 project of B.A.H.

further interpretation. Interestingly we observed two different conformations of this molecule on the surface, segregated in domains, each of the domains being homo-conformational.

The first-generation 2,2'-bipyridine dendron (see Fig. 1a(2)) forms lamellar rows as shown in Figs. 1e,f,g. Again, Figs. 1f,g show an enlargement of the left and right part of Fig. 1e that has been averaged over 121 and 104 positions, respectively. The unit cell of the molecular layer can be deduced from a Fourier spectrum of an averaged image. Molecular models of all relevant conformations were analyzed using computer graphics. The models were overlaid on the STM images in order to find the best fits, and these are depicted in Fig. 1f,g. Also in this case, two different conformations (only differing in the rotation around one bond) of the first-generation 2,2'-bipyridine dendron could be determined.

Dynamic Reorganization Studied with Scanning Tunneling Microscopy

Here, the self-organization of a Fréchet-type dendron in an aldehyde (Fig. 2a (1)) or alcohol (Fig. 2a (2)) form is studied. The combination of relatively strong interactions between interdigitated octyl chains of adjacent molecules, interactions between octyl chains and the graphite surface, as well as $\pi - \pi$ stacking interactions of the phenyl rings with the graphite results in strong (but not covalent) binding. The aromatic portions (one phenyl group is subdivided in three protrusions, marked with a white ring in Fig. 2b) of these monolayers can be directly observed using STM techniques and molecular and sub-molecular resolution images are obtained at room temperature in air.

Initially, these molecules form a pattern on graphite based on trimeric units, assembled into hexagonal host structures with a pseudo-unit cell of seven molecules, one of which remains highly mobile. Within hours (or days in the case of the alcohol

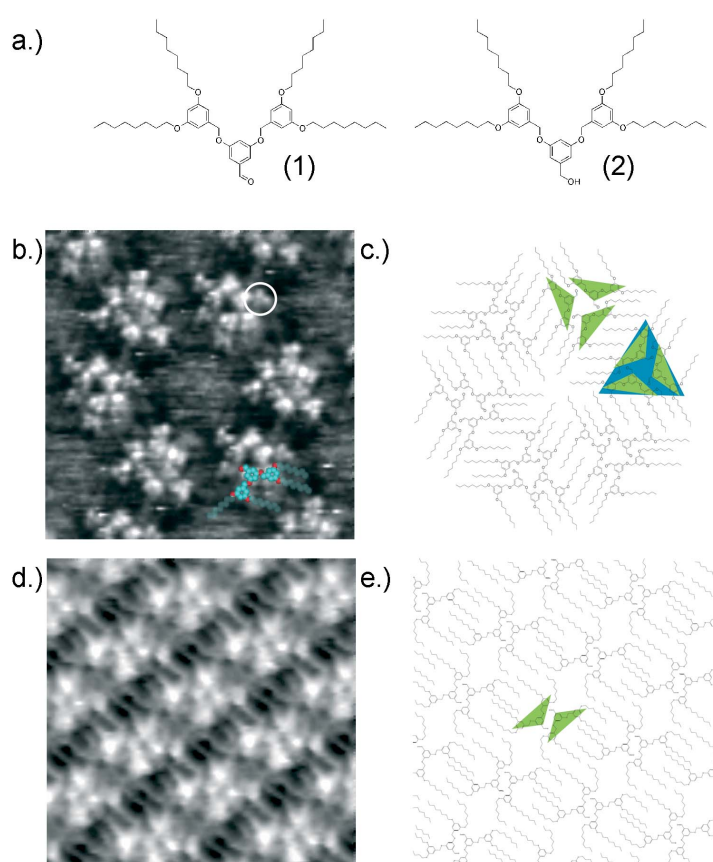


Figure 2: Structural formulae of (1) the aldehyde and (2) the alcohol Fréchet-dendritic wedges. (b) A 10 nm x 10 nm image of a monolayer of the aldehyde Fréchet-type dendron (wedge) prepared from a hexane solution, averaged over 10 positions. Marked with a circle are three protrusions of one phenyl-ring of a molecule. The conformation of the molecules is indicated with the overlaid molecular structure. ($U_{bias} = -700$ mV, $|I_t| = 8$ pA). (c) The proposed molecular arrangement. Note that in b, it appears that poorly resolved n-octyl chains can be seen. (d) A 10 nm x 10 nm enlargement of the dimeric structure of the aldehyde Fréchet-type dendron (wedge) averaged over 14 positions. The sample was prepared from a hexane solution. ($U_{bias} = -700$ mV, $|I_t| = 8.5$ pA) (e) A molecular model of the proposed arrangement of molecules of the aldehyde Fréchet-type dendron. Further details in the text and in [2]

Fréchet-type dendron), the supramolecular ordering changes from a trimeric to a dimeric pattern (Figs. 2d,e). This conversion can be followed by STM measurements. The newly formed pattern of dimers was stable over days, and no further conversion could be observed. Both chiralities (offset to the right or to the left of the molecules in a dimer) were found to be separated in homochiral domains.

Preparation and Further Analysis

Next we will study this structural transition while decreasing the surrounding temperature. Also new molecules were prepared to gain further insight into self-organization of molecules on surfaces [3].

References

- [1] Conformational Analysis of Self-Organized Monolayers with Scanning Tunneling Microscopy at Near-Atomic Resolution, Scherer, L., Merz, L., Constable, E.C., Housecroft, C.E., Neuburger, M., Hermann, B.A., *J. Am. Chem. Soc.* **127**, 4033-4041, (2005).
- [2] Octyl-Decorated Fréchet-Type Dendrons: A General Motif for Visualization of Static and Dynamic Behaviour Using Scanning Tunneling Microscopy? Merz, L., Güntherodt, H.-J., Scherer, L., Constable E.C., Housecroft C.E., Neuburger, M., Hermann B.A., *Chemistry* **11**, 2307-2318 (2005).
- [3] 2,2':6',2"-Terpyridine-4'(1'H)-thione: a missing link in metallosupra-molecular chemistry, Constable, E.C., Hermann B.A., Housecroft, C.E., Neuburger, M., Schaffner, S., and Scherer L., *New J. of Chem.* **29**, 1475 - 1481, (2005).

Magnetization Studies on Nuclear Ordered Phases of Solid ^3He in Ag Sinters

*E. Schuberth, M. Kath, and S. Bago*¹

Solid ^3He is unique among the magnetic systems as its magnetism is dominated solely by the exchange interaction of weak, localized nuclear spins in a cubic lattice. The system was initially regarded as the simplest version of a Heisenberg nearest neighbor interaction before it was realized that this picture is not enough to describe the magnetic phase diagram which was established only after two decades of laborious work [1] [2]. Solid ^3He magnetism is rather dominated by frustration between competing antiferromagnetic and ferromagnetic interactions. This leads to two nuclear magnetically ordered phases below a few mK, commonly denoted as low field phase (lfp) and high field phase (hfp) above 0.4 T. While the low field phase in bulk material most probably has the U2D2 structure proposed by Osheroff et al. [3], with two planes in the bcc lattice pointing "up" and two pointing "down" (orthogonal to the applied magnetic field) the spin structure of the "weak ferromagnetic" high field phase is indirectly inferred from its magnetization as a canted antiferromagnetic alignment.

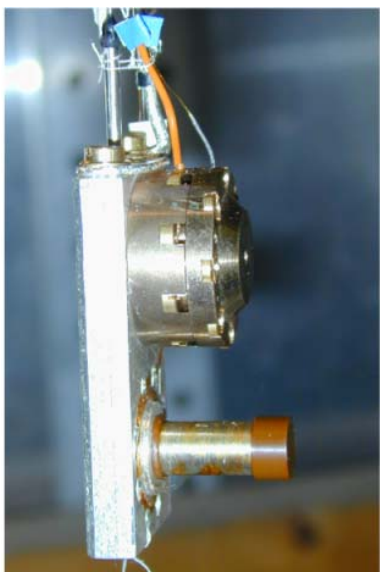


Figure 1: ^3He pressure cell (Ag) with Straty-Adams transducer and separate NMR coil former made from Vespel.

The theoretical description of the magnetic interaction is based on the fact that the quantum mechanical exchange description can be mapped on permutation operators in real space i.e. by physical exchange of atoms between lattice sites. Multiple ring exchange processes of odd or even parity lead to competing quantum mechanical exchange interactions and thus to frustration. Three and four spin exchange is favored in the dense lattice (bcc structure below 10 MPa and hcp structure above) since the two particle exchange requires too much deformation of the lattice.

This model has been worked out in a very elaborate way by Roger et al. [4] but quantitative details and even some qualitative features of the experimental phase diagram [2] are still not reproduced. To clarify experimentally the spin structures of the two phases in the sinters needed for cooling and adsorbing the heat released from the neutron absorption in ^3He , we started neutron scattering experiments

in collaboration with the Hahn-Meitner Institute in Berlin and other European and US groups [5], ultimately to reach even the high pressure hcp ordered phase below 20 μK [6]. For more information see the feasibility study by Siemensmeyer et al. [7].

A crucial requirement for neutron scattering from solid ^3He is that a single crystal can be formed in the sinter and that the sample remains in the ordered state long enough to observe magnetic neutron diffraction peaks. Also it has to be considered that possibly in the small pores of a sinter solid ^3He orders differently than in the bulk. In 200 \AA solid ^3He clusters, for instance, Matsunaga et al. found a transition very different from U2D2 [8]. In this work we measured the DC magnetization and the NMR resonance of solid ^3He in different Ag sinters

¹This work is supported by the DFG (project SCHU 450/4-1) and by the EU (contract HPRN-CT-2000-00166).

well into the nuclear ordered phases. The first was done with a home-made SQUID detection system [9] with the solid in an extension of the pressure cell sticking into the pickup coil of the flux transformer and being cooled through the sinter.

The NMR setup was described previously [10] and only a short description is given here. The H_1 (and pickup) coil was wound around a cylindrical Ag sinter which was formed around a central cooling rod, made of Ag. This arrangement was immersed in a pressure cell body, also filled with Ag sinter. Pulsed NMR measurements were performed at frequencies between 200 kHz and 3 MHz where we searched for a line splitting expected in the U2D2 structure [3].

We formed several sinters with different properties by varying the packing fractions and the heat treatments to find an optimal way to obtain single crystalline samples. A first attempt with a 100 Å Pt black powder failed (no solid was formed) and all of our following sinters were made of 700 Å "Japanese powder" which was "presintered" at 120 to 130 °C before pressing. From the measured surface areas we estimated, that in the presinter process we cluster the 700 Å particles to 2700 Å ones. At first, two sinters were formed by just pressing this powder, a third one was additionally annealed and the particle size had increased to 4200 Å. This third sinter with 50 % packing fraction proved most suitable for obtaining cold and well ordered solid.

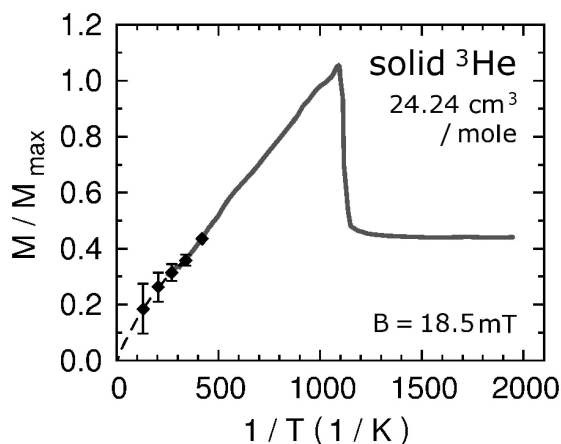


Figure 3: Normalized magnetization through the nuclear ordering transition of solid ^3He vs inverse temperature. The pressure was just above the melting pressure. Here and in Fig. 4 some special points on the continuous curves were selected as examples to show the error bars in the respective T-region.

A line splitting about 10 kHz on the high frequency side of the Larmor line (956 kHz) in the low field phase was observed only after a relatively slow growth, holding the sample at the melting curve for 6 h, and continuing cooling over 12 h. But the intensity of the signal was very low, only 2 % of the maximum amplitude just above T_{Neel} . In the spectra we could not find other split lines in the range between 200 kHz and 3 MHz. The small split-off lines near the Larmor frequency could be due to two crystallites with favorable orientation, the remaining Larmor line itself may come from a few surface

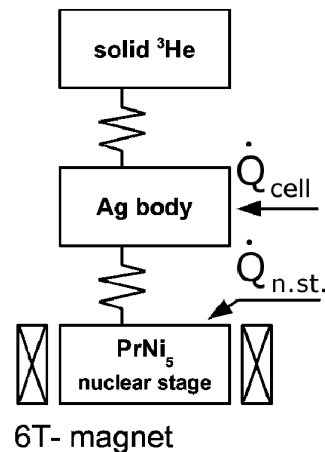


Figure 2: Model for analyzing the solid ^3He -sinter-nuclear stage heat transfer, used to determine the temperature of the solid numerically. \dot{Q}_{cell} and $\dot{Q}_{n.st.}$ denote the heat leaks to the Ag cell body and to the nuclear stage respectively.

The temperature of the solid inside the sinter can be determined only above T_{Neel} by applying a modified Curie-Weiss law [12] to the measured magnetization. Below T_{Neel} it can only be calculated. We employed a three stage thermal model to obtain T_{solid} from the temperature of the nuclear stage and the sinter using independent determinations of $R_{Kapitza}$ at various temperatures and heat capacity data of Greywall and Busch [13]. T_{3He} is calculated iteratively from $T_{n.st.}$ using measured \dot{Q}_{cell} , $\dot{Q}_{n.st.}$, and relaxation times $\tau(T) = R_{Kapitza}(T) * C_{3He}(T)$. For all sinters $R_{Kapitza}$ followed a $T^{-2.5}$ law with very small variations of the exponent. We believe that the given temperatures are correct within an error of less than 10 %.

layers of paramagnetic solid which we found to remain down to $500 \mu\text{K}$ in the DC SQUID data, see below. In the high field phase an increase of the NMR intensity by about 30 % in the ordered state is found, as expected in this "weakly ferromagnetic" phase in agreement with multiple spin exchange theories [4] which predict a "canted antiferromagnetic" state with just this magnetization.

For the SQUID magnetization signals the background of the 700 \AA Ag powder proved to be a major problem since its magnetization by far dominated the total signal. Therefore, the background had to be determined very accurately in each run for subtraction. Also a surface layer contribution $\propto T^{-1}$ was subtracted. Above 4 mK our SQUID data follow a Curie Weiss law with a negative Weiss constant of about $-2.0(5) \text{ mK}$, consistent with the observed ordering temperature of 0.94 mK . In Fig. 3 the inverse magnetization between 1 mK and 3 mK deviates from the Curie-Weiss law towards a pure Curie behavior. Our data are in full agreement with earlier ones by Hata et al. [12] including the decrease of the solid magnetization in the low field phase down to 40 % of its maximum value which is fully consistent with the U2D2 spin structure. As for the growth and cooling of ^3He crystals for neutron scattering experiments, our present result with the annealed third sinter is encouraging. With even slower growth rates, a single crystal with a small number of magnetic domains may be obtained and the pore size above 4000 \AA seems to be favorable for that. Indeed, the Berlin group found sharp structural reflections with similarly grown samples.

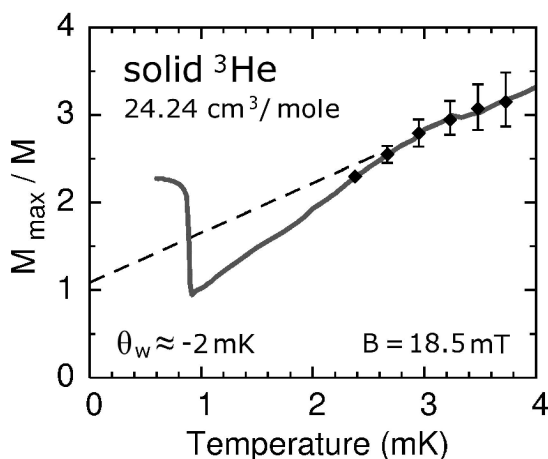


Figure 4: Data of Fig. 3 plotted as inverse magnetization of solid ^3He vs temperature.

References

- [1] D. D. Osheroff, *J. Low Temp. Phys.* **87**, 297 (1992).
- [2] J. S. Xia, W. Ni and E. D. Adams, *Phys. Rev. Lett.* **70**, 1481 (1993).
- [3] D. D. Osheroff, M. C. Cross, and D. S. Fisher, *Phys. Rev. Lett.* **44**, 792 (1980).
- [4] M. Roger, J. H. Hetherington, and J. M. Delrieu, *Rev. Mod. Phys.* **55**, 1 (1983).
- [5] The EU Research and Training Network includes groups from Hahn-Meitner-Institut, Berlin, Royal Holloway University, London, University of Liverpool, both UK, CNRS Grenoble, CEA/DSM, Paris, Saclay, both France, and the University of Florida, USA.
- [6] T. Lang, P. L. Moyland, D. A. Sergatskov, E. D. Adams, and Y. Takano, *Phys. Rev. Lett.* **77**, 322 (1996).
- [7] K. Siemensmeyer, E. A. Schuberth, E. D. Adams, Y. Takano, and K. Guckelsberger, *Physica B* **284-286**, 363 (2000).
- [8] N. Matsunaga, V. A. Shvarts, E. D. Adams, J. S. Xia, and E. A. Schuberth, *Phys. Rev. Lett.* **86**, 2365 (2001).
- [9] Erwin A. Schuberth, *Intern. Journ. Modern Physics B* **10**, 357 (1996).
- [10] E. A. Schuberth, C. Millan-Chacartegui, and S. Schöttl, *J. Low Temp. Phys.* **134**, 637 (2004).
- [11] H. Fukuyama, T. Okamoto, T. Fukuda, H. Akimoto, H. Ishimoto, and S. Ogawa, *Phys. Rev. Lett.* **67**, 1274 (1991).
- [12] T. Hata, S. Yamasaki, T. Kodama, and T. Shigi, *J. Low Temp. Phys.* **71**, 193 (1988).
- [13] D. S. Greywall and P. A. Busch, *Phys. Rev. B* **36**, 6853 (1987).

Redox Reactions and Polypyrrole Formation in Vermiculites from Spain

A. Lerf, F.E. Wagner¹, J. Poyato², V. Ramirez de Valle², J.L. Perez-Rodríguez²

Natural clay minerals of the 2:1 type very often contain Fe ions in the octahedral and/or tetrahedral layers. It has been known for fifty years that at least the octahedral iron ions are easily accessible to redox reactions; a striking example for this are the colour reactions of some amines intercalated into smectites. Oxidation of the octahedral structural iron ions has also been considered as an important step in the weathering of micas to vermiculite. To evaluate the extent of redox reactions one needs to know the $\text{Fe}^{2+}/\text{Fe}^{3+}$ ratio before and after the reaction. However, it is notoriously difficult to determine this ratio in natural and modified clay minerals by wet chemical methods. The most suitable method to derive reliable $\text{Fe}^{2+}/\text{Fe}^{3+}$ ratios is Mössbauer spectroscopy.

We report here the Mössbauer parameters measured mainly at room temperature for the vermiculites of Ojén and Santa Olalla, Spain, after various chemical modifications. The emphasis is mainly placed on the determination of the $\text{Fe}^{2+}/\text{Fe}^{3+}$ ratio. Whereas the accessible extent of reduction carried out in aqueous solutions is rather moderate (for the vermiculite of Santa Olalla ranging from 9% to about 20% of Fe^{2+} , for the Ojén from 26% to less than 40%) the Fe^{2+} content increases dramatically when the hydrazinium intercalation compounds were heated up to 400 °C and the ammonium compounds to 700 °C. An even higher degree of reduction has been obtained by treating the sodium vermiculite (Santa Olalla) in a stream of H_2/N_2 (5:95). The highest amount of Fe^{2+} thus obtained is in the order of 60%. Such a high degree of reduction could also be obtained in case of the Ojén vermiculite by treating it with ultrasound in water.

The Santa Olalla vermiculite can transfer the electrons again to an electron acceptor. Whereas the uptake of the redox active methylviologen (MV^{2+}) in the starting vermiculite does not lead to a change of the $\text{Fe}^{2+}/\text{Fe}^{3+}$ ratio, an aqueous MV^{2+} solution becomes strongly blue immediately after contact with hydrogen treated Na-vermiculite. This is indicative of the formation of the monoradical MV^+ obtained by reduction. After this treatment the Fe^{2+} content of the vermiculite drops remarkably again. The hydrogen reduced or sonicated Ojén vermiculite do not show a colour change with MV^{2+} . From these rather peculiar reaction behaviours of the two vermiculites investigated we expect insight into the electron transfer processes in these clay minerals.

Intercalated MV^{2+} can also donate electrons to structural Fe^{3+} when it is reduced by external reducing agents. Thus MV^{2+} can act as an electron shuttle to insert or to remove electrons to/from the insulating clay minerals, respectively. In treating a MV^{2+} intercalated Santa Olalla vermiculite with sodium dithionite we obtained the highest Fe^{2+} content in our reduction experiments in an aqueous medium. Now we can investigate the potential of this enhanced redox activity of the clays for electro- or photocatalytic reactions.

Structural Fe^{3+} can also act as an oxidizing agent (accompanied by the reduction to Fe^{2+}) towards organic substances like pyrrole. The oxidation of this molecule is accompanied by the formation of a conducting polymer. Though we could end up with a nanocomposite of insulating clay layers and layers of the conducting polymer. Treating both vermiculites with pyrrole vapour or liquid pyrrole leads to an immediate change in colour from pale green to

¹Physics Department, Technical University of Munich

²CSIC, Instituto de Ciencia de Materiales de Sevilla, Spain

black indicative of the deposition of the conducting polymer. The progress of this reaction can be monitored by the determination of the Fe^{2+} content via Mössbauer spectroscopy. The Fe^{2+} content increases with the type of interlayer cation in the sequence $\text{Na}^+ < \text{Mg}^{2+} < \text{Fe}^{3+}$. The samples exposed to pyrrole vapour show a lower degree of reduction than the samples soaked in liquid pyrrole. The strong increase of reduction in case of Mg^{2+} and Fe^{3+} indicates that the binding of pyrrole to these ions could promote the polymerisation of pyrrole and the accompanied reduction of structural Fe^{3+} . Up to now we do not know the degree of polymerisation and the extent to which the polypyrrole is really produced in the interlayer space of the vermiculite crystals. This is subject of further investigation.

In aqueous solution we obtained an ion exchange from sodium by pyrrolium ions but no oxidation/polymerisation. This could lead to a two step process of intercalation and subsequent oxidation/polymerisation which should allow a preferred formation of the polymer in the interlayer space with respect to deposition on the outer surfaces. The very different behaviour in aqueous solution gives some interesting implications for the electron transfer processes in clay chemistry and guides us to a broader investigation of redox reactions of clays with pure organic reagents.

It is worth mentioning that we were now successful in the intercalation of isolated Fe^{3+} ions by applying a solution of waterfree FeCl_3 in methanol. After treating the clay with such a solution the sample has been washed with pure methanol and then dried in air by evaporation of the excess methanol. The Mössbauer spectra of these samples taken at 4.2 K do not show any magnetic hyperfine splitting typical for Fe-oxy-hydroxides observed in the samples prepared in aqueous medium. There is also no indication of a magnetic ordering in the clay by inserting the Fe^{3+} ions in the interlayer space.

Large Geometrically Enhanced TMR Effect in Magnetite Based Magnetic Tunnel Junctions

*A. Boger, E. Menzel, S.T.B. Gönnerwein, M. Opel, and R. Gross*¹

The Magnetoresistive Random Access Memory (MRAM) which is based on magnetic tunnel junctions (MTJs) using ferromagnetic electrodes with high spin polarization is a promising candidate for the next generation computer memory. In MRAMs information is stored as a magnetization direction in the electrodes of a MTJ, whereas in the presently used DRAMs information is stored as a charge on the metallic electrodes of a capacitor. Compared to our present DRAM memory, MRAM has the advantage that it is nonvolatile at similar other performance parameters. The implementation of MRAM requires the fabrication of MTJs with high tunneling magnetoresistance (TMR). Beyond storage, such MTJs are also useful for the realization of novel programmable logic elements [1] as well as extremely sensitive magnetic field sensors. The fabrication technology for MTJs based on simple ferromagnetic transition metals and alloys made an enormous progress in the year 2005. It has been reported that coherent spin-polarized tunneling between two ferromagnetic Fe(001) electrodes across an epitaxial tunneling barrier of MgO(001) could enhance the TMR effect above 200% [2, 3]. However, in general the ferromagnetic transition metals with their incomplete spin polarization of the charge carriers at the Fermi level are not the ideal materials for realizing MTJs with high TMR values. The recently reported high TMR values for Fe/MgO/Fe tunnel junctions are only possible by coupling specific electronic states through a structurally oriented tunneling barrier. In contrast, the use of half-metallic ferromagnets having a full spin-polarization of the charge carriers should allow to achieve even higher TMR values. Here, magnetite (Fe_3O_4) is of specific interest, since it has been predicted to be half-metallic [4] and furthermore has a high Curie temperature of 860 K easily enabling room temperature operation. Indeed, spin-resolved photoemission spectroscopy in magnetite thin films has revealed a spin polarization near the Fermi edge of $(-80 \pm 5)\%$ at 300 K [5].

Over the last years, we have successfully implemented a fabrication process for MTJs with Fe_3O_4 as bottom and Co or Ni as top electrodes. So far at room temperature we found a high TMR effect of up to about 20% leading to an estimate for the spin polarization of magnetite of about 60% [6]. Here, we report on the influence of the geometry of the MTJ on the measured TMR values. We found that the TMR could be increased up to several 1000% in a limited temperature regime, if the geometrical dimensions as well as the resistivity and thickness values of the magnetite bottom electrode were chosen properly. The resulting huge TMR effects is a geometrically enhanced TMR effect resulting from an inhomogeneous current distribution in the junction electrodes. Such effect is difficult to be realized with metallic electrodes due to the usually small resistivity of metals.

The thin film multilayer structures were fabricated in an ultra high vacuum (UHV) cluster system using pulsed laser deposition (PLD) and electron beam evaporation. First the MgO(001) single crystalline substrates were covered by a thin epitaxial TiN buffer layer by PLD. Then the Fe_3O_4 bottom electrode was grown epitaxially also by PLD. Details on the growth process including in-situ reflection high energy electron diffraction (RHEED) analysis and laser substrate heating are described elsewhere [7, 8, 9]. On top of the 40 nm thick magnetite base electrode, a 1.4 nm thin layer of Al was deposited by electron beam evaporation in UHV at room temperature. Afterwards, the Al was oxidized in pure oxygen to form the insulating AlO_x tunnel barrier. In the last step, the 40 nm thick Co counter electrode was deposited in-situ also by

¹This work is supported by the BMBF (project No.: 13N8279) and the DFG (project No.: GR 1132/13).

electron beam evaporation. The surface roughness of the films was probed in-situ with an Omicron atomic force microscope. The structural quality and the film thickness were studied by high resolution X-ray diffractometry and reflectometry, respectively, using a Bruker-AXS four-circle system. The magnetic properties of the thin film structures were measured with a Quantum Design SQUID magnetometer and, finally, the magnetotransport properties of the completed MTJs were obtained in an Oxford magnet system with variable temperature insert. We note that due to their high crystalline quality for the epitaxial magnetite films about the same magnetic properties and Verwey transition behavior have been observed as reported for single crystals [10].

From the deposited multilayers, MTJs as sketched in Fig. 1 have been fabricated using optical lithography and ion beam milling. The applied current I flows from the low-resistivity TiN buffer layer to the bottom ferromagnetic electrode (Fe_3O_4) across the tunneling barrier (AlO_x) and the top ferromagnetic electrode (Co) in perpendicular direction and finally leaves the sample through the left or right part of the split Au wiring layer (right in Fig. 1). The resistance R of the MTJ is derived from the voltage drop V between the bottom TiN layer and one part of the split Au wiring layer (left in Fig. 1). According to Julliere's model [11] R depends on the relative direction of the magnetization in the two ferromagnetic electrodes. For ferromagnetic materials with the same sign of the spin polarization of the carriers near the Fermi edge, a low value R_p and high value R_{ap} of the tunneling resistance is expected for the parallel and antiparallel magnetization configuration, respectively. This is also the case for our configuration, since both Fe_3O_4 and Co have negative spin polarization.

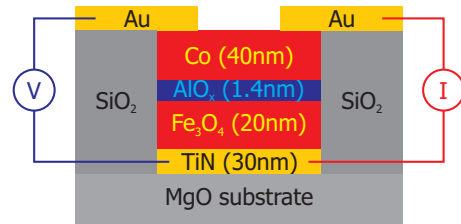


Figure 1: Cross-sectional view of a Magnetic Tunnel Junction (MTJ). The current (red) flows perpendicular to the multilayer structure from the bottom electrode (TiN/ Fe_3O_4) across the tunneling barrier (AlO_x) to the top electrode (Co/Au).

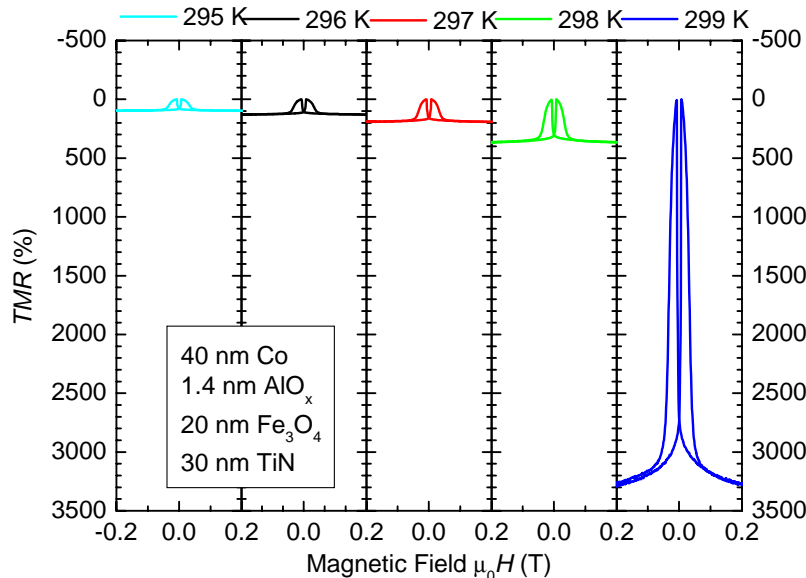


Figure 2: Resistance vs. applied magnetic field H for a $\text{Fe}_3\text{O}_4/\text{AlO}_x/\text{Co}$ junction at different temperatures. The TMR value reaches values of more than 3000% near room temperature.

whole measured temperature range from 150 K to 350 K. The switching fields extracted from the $R(H)$ curves agreed well with the coercive fields obtained for the magnetic electrodes from magnetization curves measured by SQUID magnetometry [6].

Performing $R(H)$ measurements in a 4-probe configuration the TMR effect

$$\text{TMR}(H) = \frac{R_{ap} - R(H)}{R_p} \quad (1)$$

was determined for the investigated MTJs at different temperatures. Here, for R_{ap} the maximum resistance value in the $R(H)$ curve and for R_p the value measured at 100 mT was used. The samples reproducibly showed a clear positive TMR effect, i.e. $R_{ap} \geq R(H)$, with almost ideal symmetric switching behavior. The TMR effect could be observed in the

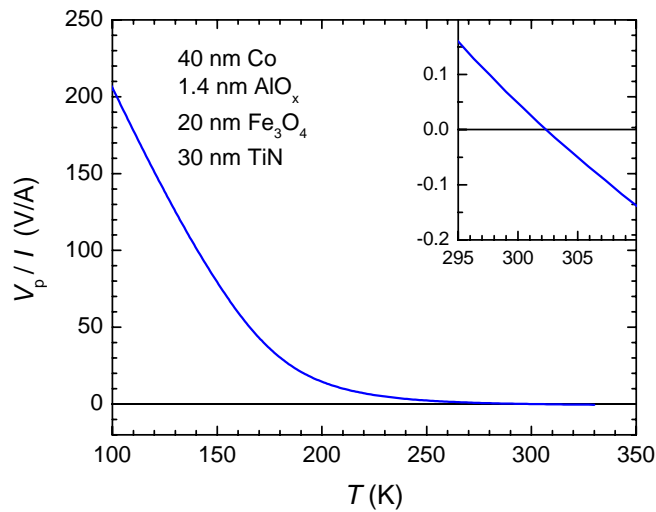


Figure 3: Temperature dependence of the resistance $R_p = V_p/I$. The reason for this astonishing observation is the fact that the measured voltage drop V_p for the parallel magnetization configuration approaches zero near 299 K. In turn, $R_p = V_p/I$, that is the denominator in eq.(1) approaches zero (see Fig. 3) leading to the extremely high TMR value. This effect could be reproduced in several samples and depends strongly on both the geometry of the MTJ structure as well as the thickness and resistivity of the bottom Fe_3O_4 electrodes [12].

To better understand this phenomenon, we performed numerical simulations to determine the current density distribution as well as the electrical potential within the MTJ structure. The simulations were based on the finite elements method. This numerical technique allows for the solution of partial differential equations also for non-symmetric objects which cannot be solved analytically. The finite elements method splits the continuous non-symmetric object into many small areas (so-called *finite elements*) with simpler shape and higher symmetry. For each of the finite elements there exists one set of partial differential equations which is being solved for this specific area. These solutions are then merged together using continuous boundary conditions. This allows to predict the behavior of the whole object and to simulate e.g. the current distribution of a complex MTJ. The calculations were performed with the help of the commercially available software FEMLAB 3.1 using the “conductive media DC” mode.

From the calculations we found that - due to an inhomogeneous current distribution - negative voltages across the sample can occur, if the total resistance of the effective tunneling barrier becomes comparable to that of the Fe_3O_4 base electrode [12]. This inhomogeneous current distribution is shown in Fig. 4 (left). Part of the current I coming from the back through the TiN bottom layer crosses the AlO_x barrier three times before leaving the sample through the right

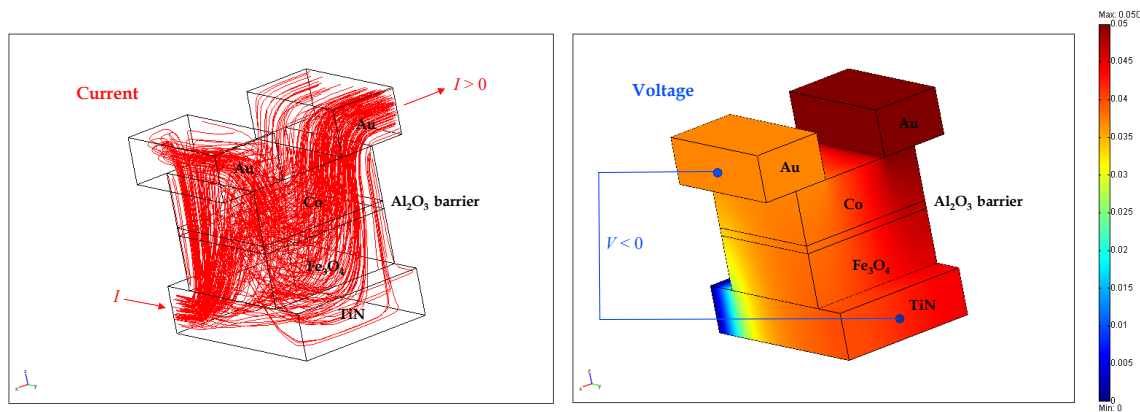


Figure 4: Simulated distribution of the current I (left) and the electric potential V (right) of a $\text{Fe}_3\text{O}_4/\text{AlO}_x/\text{Co}$ junction. TiN serves as buffer layer for bottom magnetite electrode while Au is used for the split wiring layer of the top Co electrode. The inhomogeneous current distribution leads to a negative voltage across the sample.

part of the split Au wiring layer. This leads to an electric potential within the MTJ structure that is higher at the front of the bottom electrode than in the left top electrode (Fig. 4, right). This results in a negative voltage V across the sample although the direction of the current I has not been changed.

In summary, the TMR effect usually is increased by increasing the difference $R_{\text{ap}} - R_{\text{p}}$ between the resistance values for the antiparallel and parallel magnetization configuration. The resulting magnetoresistive effect is related to the spin polarization in the junction electrodes and can be denoted as the intrinsic TMR effect. On the other hand, the TMR effect also can be increased by reducing the resistance R_{p} . We have shown that this can be obtained by optimizing the geometry of the MTJ. Therefore, this effect can be denoted as a geometric TMR effect. We have shown that the latter effect can be as large as several 1000% at room temperature but is restricted to a small temperature interval.

References

- [1] A. Ney, C. Pampuch, R. Koch, and K. H. Ploog, *Nature* **425**, 485 (2003).
- [2] S.S.P. Parkin, C. Kaiser, A. Panchula, P.M. Rice, B. Hughes, M. Samant, and See-Hun Yang, *Nature Materials* **3**, 862 (2004).
- [3] S. Yuasa, T. Nagahama, A. Fukushima, Y. Suzuki, and K. Ando, *Nature Materials* **3**, 868 (2004).
- [4] H.T. Jeng and G.Y. Guo, *Phys. Rev. B*, **65**, 094429 (2002).
- [5] Y.S. Dedkov, U. Rüdiger, and G. Güntherodt, *Phys. Rev. B* **65**, 064417 (2002).
- [6] S. Qureshi, D. Reisinger, E. Menzel, A. Erb, L. Alff, M. Opel, and R. Gross, *WMI Jahresbericht*, 50 (2004).
- [7] J. Klein, C. Höfener, L. Alff, and R. Gross, *Supercond. Sci. Technol.* **12**, 1023 (1999); see also *J. Magn. Magn. Mater.* **211**, 9 (2000).
- [8] D. Reisinger, B. Blass, J. Klein, J.B. Philipp, M. Schonecke, A. Erb, L. Alff, and R. Gross, *Appl. Phys. A* **77**, 619 (2003).
- [9] D. Reisinger, M. Schonecke, T. Brenninger, M. Opel, A. Erb, L. Alff, and R. Gross, *J. Appl. Phys.* **94**, 1857 (2003).
- [10] D. Reisinger, P. Majewski, M. Opel, L. Alff, and R. Gross, *Appl. Phys. Lett.* **85**, 4980 (2004).
- [11] M. Jullière, *Phys. Lett. A* **54**, 225 (1975).
- [12] E. Menzel, *Diplomarbeit*, TU München (2004).

Generation of Microwave Single Photons and Homodyne Detection on a Chip

*M. Mariantoni, A. Emmert, A. Marx, R. Gross,¹
M.J. Storzcz², F.K. Wilhelm,² W.D. Oliver,³ H. Christ,⁴ E. Solano^{4,5}*

In the interplay between matter and light, the generation and measurement of single photons are among the most interesting and challenging phenomena. In order to exploit possible implementations of such processes in solid-state architectures, in the last year we established an intensive collaboration between condensed matter experimentalists and theorists and quantum opticians, in order to merge different communities in a wide and multidisciplinary project [1]. The first task of this collaboration was to show theoretically the possibility of implementing a deterministic source of microwave single photons at the output of a superconducting resonator containing a flux qubit. A Raman-like scheme [2] determines the coupling between the cavity and the qubit, consisting of the two ground states of a three-level system in a Λ -type configuration [3]. Furthermore, we showed that these single photons can be measured by means of a microwave quantum homodyne detection (MQHD) scheme [4], based on a superconducting hybrid ring [5] acting as an on-chip microwave beam splitter (MBS). The generation of propagating microwave single photons in a controlled way and an appropriate measurement apparatus represent building blocks to establish on-chip quantum information transfer between qubits. First steps towards the experimental realization of this proposal have been taken. Superconducting niobium hybrid rings have been fabricated at the WMI. Initial high-frequency tests of these hybrid rings at 4 K are very promising.

A prototypical example of a flux-based quantum circuit is the radio-frequency (RF) superconducting quantum-interference device (SQUID) [6], a superconducting loop interrupted by a single Josephson tunnel junction. The RF SQUID Hamiltonian is

$$\hat{H}_S = \frac{\hat{Q}^2}{2C_j} + \frac{(\hat{\Phi} - \Phi_x)^2}{2L_s} - E_J \cos\left(2\pi \frac{\hat{\Phi}}{\Phi_0}\right), \quad (1)$$

where \hat{Q} is the charge stored on the junction capacitor C_j , $\hat{\Phi}$ is the total flux threading the loop, Φ_x is an externally applied quasi-static flux bias, L_s is the self-inductance of the loop, $E_J \equiv I_{c0}\Phi_0/2\pi$ is the Josephson coupling energy, I_{c0} is the junction critical current, and $\Phi_0 = h/2e$ is the flux quantum.

For appropriate design parameters, and close to half-integer values of Φ_x/Φ_0 , the RF SQUID potential profile becomes a relatively shallow double well whose asymmetry can be tuned by setting Φ_x (see Fig. 1). In this case, the two lowest eigenstates $|g\rangle$ and $|e\rangle$ are localized in the left and right wells, respectively, whereas the second excited state $|h\rangle$ is delocalized with energy above the barrier. The energy levels can be tuned by statically biasing Φ_x during the experiment, and transitions between states are driven by pulsed ac excitations.

The segment of superconducting coplanar waveguide (CWG) shown in Figs. 2 (a), (b), and (d) is one realization of a monolithic resonator. Such a resonator is characterized by eigenenergies with transition angular frequencies ω_k that are much larger than the thermal energy at

¹This work is supported by the DFG through the Cooperative Research Center 631, ES acknowledges EU support through RESQ project.

²Department Physik, CeNS and ASC, LMU, Theresienstrasse 37, D-80333 München, Germany

³MIT Lincoln Laboratory, 244 Wood Street, Lexington, Massachusetts 02420, USA

⁴Max-Planck Institute for Quantum Optics, Hans-Kopfermann-Strasse 1, D-85748 Garching, Germany

⁵Sección Física, Departamento de Ciencias, Pontificia Universidad Católica del Perú, Apartado 1761, Lima, Peru

cryogenic temperatures. Its Hamiltonian is $\hat{H}_C = \sum_k \hbar \omega_k (\hat{a}_k^\dagger \hat{a}_k + 1/2)$, where \hat{a}_k^\dagger and \hat{a}_k are the bosonic creation and annihilation operators for mode k . Voltage and current, corresponding to electric and magnetic fields, respectively, are conjugate operators associated with the quantized resonator, $\hat{I}_C(z, t) = (\partial/\partial t) \hat{\vartheta}(z, t)$, where z is the spatial coordinate for the superconducting inner strip and $\hat{\vartheta}(z, t)$ is the normal mode expansion of the cavity field. The vacuum rms current of a single mode $k = K$ of the cavity is $I_{c,K}^0(z) = \sqrt{\hbar \omega_K / 2(Dl)} |\sin(2\pi z/D - K\pi/2)|$.

Here, D is the length of the resonator and l is its total series inductance per unit length. The cavity is chosen to be a $\lambda/2$ open-circuited resonator operated at the second mode, $K = 2$, and coupled capacitively to a CWG transmission line, as in Figs. 2 (a), (b), and (d). Such a cavity can reach external quality factors $Q_x = 10^4$ at $f_K = \omega_K/2\pi \approx 10$ GHz [7], corresponding to a cavity decay rate $\kappa_c/2\pi \approx 1$ MHz. Hence, at a base temperature $T_b \approx 50$ mK, the mean number of thermal photons is $\langle n_{th} \rangle = [\exp(\hbar \omega_K / k_B T_b) - 1]^{-1} \approx 10^{-4}$ and the cavity mode can be considered to be in the vacuum state $|0\rangle$.

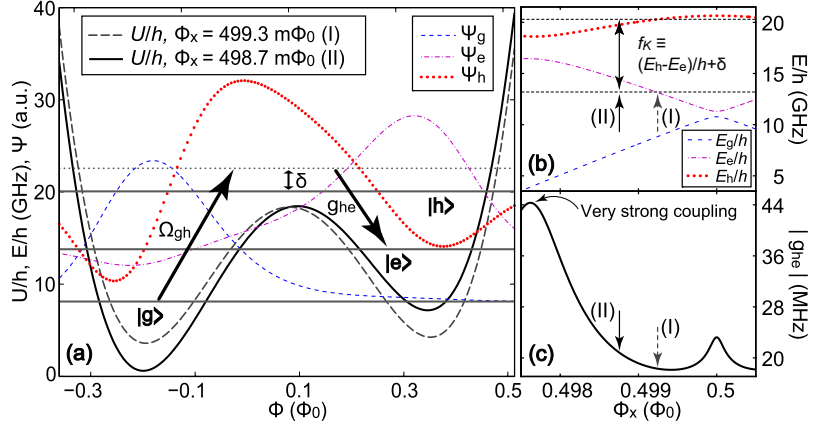


Figure 1: (a) Potential profile of the RF SQUID for two distinct values of Φ_x [(I) and (II)] and wave functions for the first three lowest energy levels ($|g\rangle$, $|e\rangle$, and $|h\rangle$). Parameters are given in Table I. The Raman scheme is indicated with arrows. (b) RF SQUID energy-band diagram near $\Phi_0/2$ plotted vs. Φ_x . Zero detuning case, point (I), and large detuning case, point (II). (c) Absolute value of the vacuum Rabi frequency g_{he} as a function of Φ_x . The coupling reaches 40 MHz at the anti-crossing between levels $|e\rangle$ and $|h\rangle$.

Embedding the RF SQUID in the CWG resonator [see Figs. 2 (a), (b) and (c)] allows a strong, inductive coupling between any two levels of the RF SQUID and the single cavity mode K . The resulting interaction Hamiltonian is $\hat{H}_I = -M_{cs} \hat{I}_{c,K} \hat{I}_s$, where $\hat{I}_{c,K}$ and \hat{I}_s are resonator and RF SQUID current operators, respectively, and M_{cs} is their mutual inductance. Explicitly, we find

$$\hat{H}_I = - (M_{cs}/L_s) I_{c,K}^0(z) (\hat{\Phi} - \Phi_x) i [\hat{a}_K^\dagger(t) - \hat{a}_K(t)]. \quad (2)$$

The RF SQUID can be positioned near one of the anti-nodes of the vacuum current [Fig. 2 (a)] and can be biased to yield maximum coupling for any two of its eigenstates $|i\rangle$ and $|j\rangle$. The interaction matrix element between these levels represents their coupling strength with mode K and it is used to define the vacuum Rabi frequency $g_{ij} = - (M_{cs}/L_s) I_{c,K}^0(z) \langle i | \hat{\Phi} | j \rangle / \hbar$.

A main application of the system illustrated above is the generation of single photons at frequency f_K in a manner similar to a quantum-optical Raman scheme [2, 8]. After preparing the RF SQUID in level $|g\rangle$, the transition $|g\rangle \leftrightarrow |h\rangle$ is driven by a classical excitation with Rabi frequency Ω_{gh} and detuned by the amount δ . The same transition is detuned from the resonator mode K by an amount $\Delta \gg \delta$, resulting in a comparatively negligible coupling. On the other hand, the $|h\rangle \leftrightarrow |e\rangle$ transition is the only one coupled to mode K , and it is also detuned by δ [see Figs. 1 (a) and (b)]. Choosing $\delta \gg \max[\Omega_{gh}, g_{he}]$, level $|h\rangle$ can be adiabatically eliminated [2, 8], thus leading to the effective second-order Hamiltonian

$$\begin{aligned} \hat{H}_{\text{eff}} = & \hbar \frac{\Omega_{gh}^2}{\delta} |g\rangle \langle g| + \hbar \frac{g_{he}^2}{\delta} |e\rangle \langle e| \hat{a}_K^\dagger \hat{a}_K + \\ & + \hbar g_{\text{eff}} (|g\rangle \langle e| \hat{a}_K + |e\rangle \langle g| \hat{a}_K^\dagger), \end{aligned} \quad (3)$$

where $g_{\text{eff}} = (\Omega_{\text{gh}}/\delta)g_{\text{he}}$ is the effective Raman coupling. The first two terms at the r.h.s. of Eq. (3) are ac Zeeman shifts, while the last term describes an effective anti-JC dynamics, inducing transitions within the $\{|g\rangle|n\rangle, |e\rangle|n+1\rangle\}$ subspaces. When the strong-coupling regime is reached, $g_{\text{eff}} \gtrsim \max[\kappa_{\text{c}}/2\pi, \gamma_{\text{he}}^{\text{eff}}/2\pi]$, an effective π -pulse realizes a complete transfer of population from state $|g\rangle|0\rangle$ to state $|e\rangle|1\rangle$. This process leads to the creation of a microwave Fock state $|1\rangle$ inside the resonator.

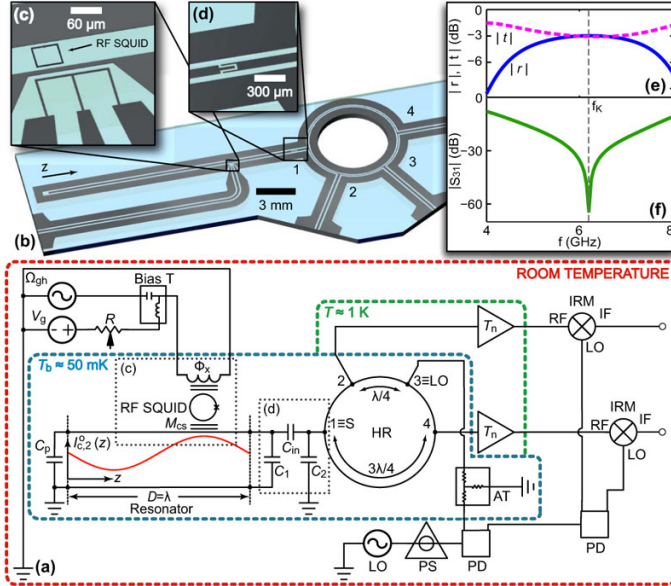


Figure 2: (a) Sketch of the entire generation and detection network (C_{in} , C_1 , and C_2 : capacitive Π network representing the resonator input port; C_p : parasitic capacitor at the cavity open-circuit ending; HR: hybrid ring; PS: phase shifter; PD: power divider; AT: attenuator). (b) Asymmetric CWG resonator with integrated HR. (c) On-chip antenna providing the classical driving Ω_{gh} . (d) Resonator-CWG coupling region. (e) The waves traveling around the HR interfere resulting in the plotted reflection and transmission amplitude patterns. (f) Isolation between ports three and one of the HR.

$V_{\text{d}}^2/Z_{\text{c}}$, where Z_{c} is the characteristic network impedance.

The MBS is realized using a superconducting four-port device: the hybrid ring, depicted in Fig. 2 (a). The advantageous coplanar design proposed here can be easily scaled and integrated with resonators in monolithic circuits that can be fabricated with Nb technology [see Fig. 2 (b)]. We now extend the classical theory of hybrid rings in Ref. [5] to the quantum regime by analogy with an optical beam splitter. With only the vacuum incident at ports two and four, and up to a global phase common to both input beams, the reduced quantum input-output relations of a (superconducting) lossless MBS are

$$\begin{bmatrix} \hat{a}_2 \\ \hat{a}_4 \end{bmatrix} = \begin{bmatrix} r & t \\ -t^* & r^* \end{bmatrix} \begin{bmatrix} \hat{a}_{\text{S}} \\ \hat{a}_{\text{LO}} \end{bmatrix}, \quad (4)$$

where r and t are the complex, frequency-dependent reflection and transmission coefficients, \hat{a}_{S} and \hat{a}_{LO} are the signal and LO port operators, respectively. The latter is chosen to be a classical coherent field which is characterized by its complex amplitude $\alpha_{\text{LO}} = |\alpha_{\text{LO}}| \exp(i\theta_{\text{r}})$, where $|\alpha_{\text{LO}}|$ is the real part of this field and θ_{r} is its relative phase with respect to S. The numerical simulations plotted in Fig. 2 (e) show that the MBS can be *balanced* over a broad bandwidth around the operation frequency f_{K} , i.e., $r = t = 1/\sqrt{2}$ (−3 dB).

After showing the theoretical possibility to generate microwave single photons, we investigated a method to measure these single photons. In particular we introduced an on-chip MQHD technique as a means to detect weak quantum signals, even at the level of Fock states. It can be implemented in three main steps. First, a signal (S) and a local oscillator (LO), characterized by the same angular frequency $\omega_{\text{S}} = \omega_{\text{LO}}$, are coherently superposed at a suitably designed MBS [Fig. 2 (a)]. This unitary manipulation of the input fields, the quantum part of the measurement process, is performed at cryogenic temperatures. Second, the microwave fields at the MBS output ports are amplified at low temperatures and then down-converted to dc signals via classical homodyning, which is carried out with image-rejection mixers (IRMs) at room temperature [5]. Finally, the dc signals are detected as rms voltages V_{d} with an oscilloscope and then processed to calculate the corresponding powers $P_{\text{d}} =$

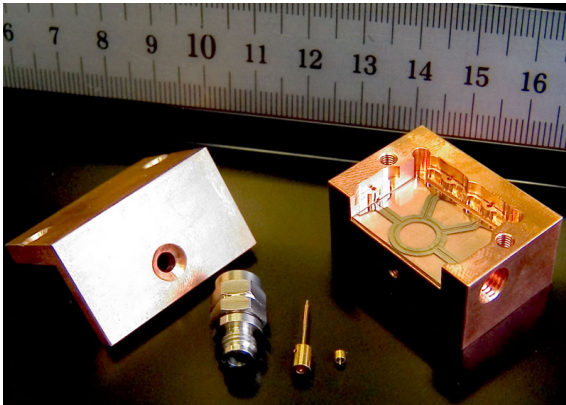


Figure 3: Superconducting niobium hybrid fabricated on a sapphire substrate mounted in a copper test box.

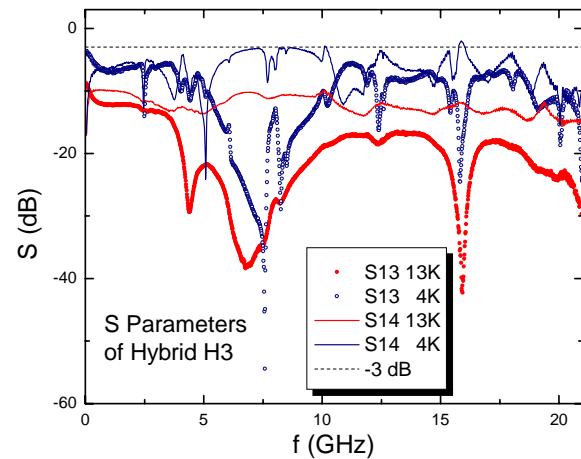


Figure 4: Selected S-parameters of a superconducting hybrid above the superconducting transition temperature and at 4 K. Circles show the frequency dependent isolation between port 2 and 4, solid lines show the coupling between port 1 and 4.

A balanced MQHD is implemented subtracting the powers associated to the measured voltages at ports two and four of the IRMs,

$$P_{d,2} - P_{d,4} \propto N_2 - N_4 = 2 |\alpha_{LO}| X_{\theta_r}, \quad (5)$$

where the quantity $(N_2 - N_4)$ represents different realizations of the measured observable $(\hat{n}_2 - \hat{n}_4)$, with $\hat{n}_2 = \hat{a}_2^\dagger \hat{a}_2$, $\hat{n}_4 = \hat{a}_4^\dagger \hat{a}_4$, and $\hat{a}_2 = (\hat{a}_S + \hat{a}_{LO})/\sqrt{2}$, $\hat{a}_4 = (-\hat{a}_S + \hat{a}_{LO})/\sqrt{2}$. Furthermore, X_{θ_r} represents different realizations of the measured quadratures $\hat{X}_{\theta_r} \equiv (\hat{a}_S^\dagger e^{i\theta_r} + \hat{a}_S e^{-i\theta_r})/2$, where the LO operators were replaced by their complex amplitudes. Equation (5) contains the essence of the balanced MQHD technique and reveals that the quadrature of the *weak* signal S is *amplified* by a factor $2 |\alpha_{LO}|$, and thus, for large LO voltages, can overcome the detector (a cold amplifier) noise floor. MQHD can be used for measuring any quadrature moment $\langle \hat{X}_{\theta_r}^p \rangle$ of signal S . It can be easily shown that the knowledge of the first two quadrature moments are sufficient to discriminate between classical-coherent states and Fock states, and between different Fock states [4].

Initial steps towards an experimental realization of the MQHD technique have been taken by fabricating and testing prototype superconducting hybrid rings which eventually will act as MBS. Fig.3 shows a superconducting hybrid ring which has been fabricated by sputter deposition and reactive ion etching at the WMI. The hybrid is mounted in a copper box which is used for high-frequency tests at low temperatures. Fig.4 depicts selected scattering parameters of the device at a temperature above the critical temperature T_c and at 4 K. The isolation between ports 2 and 4 shows a peak which is in good agreement with extensive microwave simulations, which we have performed to design the structure. The width of the isolation peak is about 70 MHz at -40 dB, which is promising for the application as a MBS. The coupling between port 1 and 4 is very close to the expected value of 3 dB in the superconducting regime. The additional resonances showing up below T_c , although not yet fully understood, are most probably caused by problems in making contact to the on-chip coplanar niobium structures.

References

- [1] M. Mariantoni *et al.*, e-print cond-mat/0509737 (2005).

- [2] M. França Santos, E. Solano, and R.L. de Matos Filho, *Phys. Rev. Lett.* **87**, 093601 (2001).
- [3] C.-P. Yang, S.-I Chu, and S. Han, *Phys. Rev. Lett.* **92**, 117902 (2004).
- [4] U. Leonhardt, *Measuring the Quantum State of Light* (Cambridge University Press, Cambridge, 1997).
- [5] R.E. Collin, *Foundations for Microwave Engineering*, 2nd ed. (Wiley-IEEE Press, New Jersey, 2000).
- [6] J.R. Friedman *et al.*, *Nature* **406**, 43 (2000).
- [7] A. Wallraff *et al.*, *Nature* **431**, 162 (2004).
- [8] M. Keller *et al.*, *Nature* **431**, 1075 (2004).

Microwave Spectroscopy on Single Josephson Junctions

*K. Madek, S. Beutner, R. Stolle, G. Wild, C. Probst, A. Marx, and R. Gross*¹

At low temperature the switching of a Josephson junction with small damping to the voltage state is governed by the macroscopic quantum mechanics of the superconducting phase difference across the junction. In superconducting quantum interference devices (SQUIDs) coupled to a superconducting flux quantum bit (qubit) this switching can be used to determine the quantum state of the qubit, since the switching current depends on the quantum state of the qubit. The quantum behavior of the phase difference across a single current-biased Josephson junction becomes obvious in escape rate measurements. The rate of escape to the voltage state shows a crossover from a thermally activated to a tunneling behavior at very low temperatures. The quantum nature of the phase difference already has been demonstrated in microwave spectroscopy experiments which show the quantization of energy levels in the washboard potential describing a current-biased Josephson junction [1].

We have shown the crossover from a classical to the quantum regime in a single Nb/AlO_x/Nb Josephson junction (cf. Annual Report 2004 [2]) in a current ramping technique, where histograms of the switching current are taken. This proved the viability of the experimental setup and demonstrated that the extensive filtering of the biasing lines together with strong magnetic shielding provides an efficient decoupling of the sample from environmental fluctuations. The dilution insert has been equipped with a microwave line carefully thermally anchored at 4 K and at the still. Using this setup we have performed spectroscopy experiments on individual Nb/AlO_x/Nb Josephson junctions showing the level quantization in the washboard potential during the last year. We also have shown multi-photon excitations of the phase particle, where up to 8 photons are absorbed simultaneously. Such processes have only recently been observed in macroscopic quantum systems. Multi-photon processes may eventually put limitations on qubit coherence times, because lower frequencies may already cause decoherence.

Figure 1 shows the potential energy of a current biased Josephson junction for a bias current close to the critical current vs the phase difference across the junction. For this choice of parameters three discrete energy levels fit into a potential well. The phase particle can be excited from the ground state to excited states by irradiating the junction by microwaves with energy matching the energy differences of two distinct energy levels. As is obvious from Fig. 1 the energy barrier for tunneling to the continuum of states is significantly smaller for the excited states. Since the tunneling rate depends exponentially on the barrier height and the barrier width, the macroscopic quantum tunneling rate from the first excited state is increased by a factor of typically 10 000 compared to the ground state. A second peak appears in the switching current histograms since by

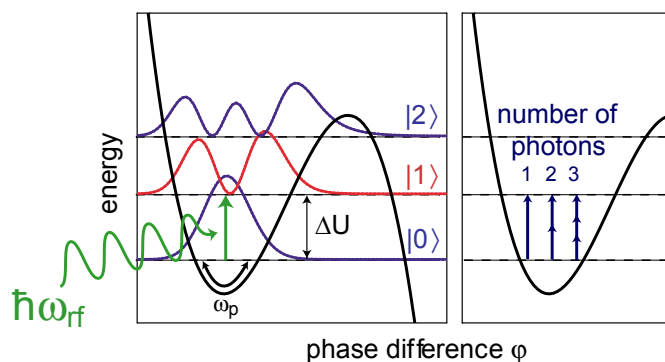


Figure 1: Left: Potential energy of a Josephson Junction vs phase difference across the junction for a bias current close to the critical current. The dashed lines show three quantized energy levels, for which the squared wave functions are indicated. Microwave irradiation induces transitions from the ground state to excited states. The photon energy $\hbar\omega_{rf}$ matches the level spacing ΔU . Right: Single and multi-photon transitions.

¹This work is supported by the DFG through the Cooperative Research Center 631.

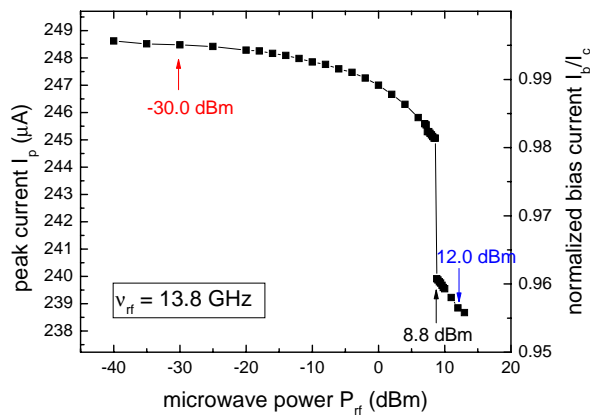


Figure 2: Maximum of the switching current histograms vs the microwave power for $\nu_{\text{rf}} = 13.8$ GHz. The arrows indicate the values of P_{rf} for which the switching current histograms are shown in Fig. 3.

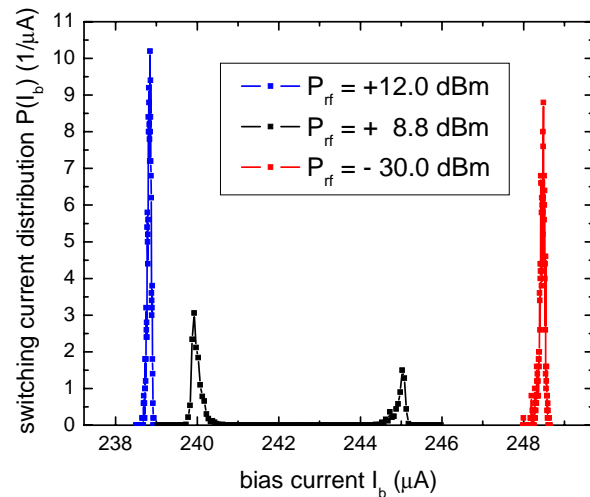


Figure 3: Switching current distributions for three different values of the microwave power.

exciting the phase particle to the first excited state the switching to the voltage state occurs at lower bias current values. In the large signal limit (i.e. for high enough microwave power), the potential energy of the Josephson junction is strongly modified by the applied microwave [3]. Therefore, the peak position of the switching current distribution shows a strong decrease with increasing microwave power in the high power regime. The histograms in Fig. 3 show a double peak structure or only a single peak corresponding to the escape from the ground state or the first excited state, respectively.

The anharmonicity of the potential of a current-biased Josephson junction allows the excitation of the phase particle by the simultaneous absorption of more than a single photon [4]. This becomes evident when plotting the microwave frequency $\nu_{\text{rf}} = \omega_{\text{rf}}/(2\pi)$ versus the resonant bias current I_{res} defined as the current at which the escape of the phase particle is maximally enhanced (cf. Fig. 4). In general the resonance condition taking multi-photon transitions into account is given by

$$\nu_{\text{rf}} = \frac{\nu_{p_0}}{q} \left(1 - \left(\frac{I_b}{I_c} \right)^2 \right)^{1/4}, \quad (1)$$

where the plasma frequency $\nu_{p_0} = \omega_{p_0}/(2\pi)$ is replaced by ν_{p_0}/q and q is the number of photons inducing the transition. I_b is the bias current, I_c is the junction critical current, and ω_{p_0} is the Josephson plasma frequency. The resonances shown in Fig. 4 obviously fall into different groups indicated by the dashed lines. This is in excellent agreement with Eq. (1). Transitions including up to eight photons have been observed in the experiments. The measurements have been performed both in the quantum- and in the thermal limit, showing no difference between these two cases, see Fig. 4. This proves that the escape of the phase particle is indeed caused by tunneling out of the first excited state, since thermal effects are effectively suppressed by the high tunneling rate. Fitting Eq. (1) to the experimental data multiplying the measured frequency by the respective number of photons q gives ω_{p_0} and I_c , cf. Fig. 5. The value of the critical current obtained in this fit is in very good agreement with the value determined in previous measurements in the thermal regime.

Presently, we have extended the escape rate measurements both with and without microwave irradiation to superconductor/insulator/normal/ferromagnet/superconductor (SINFS) and

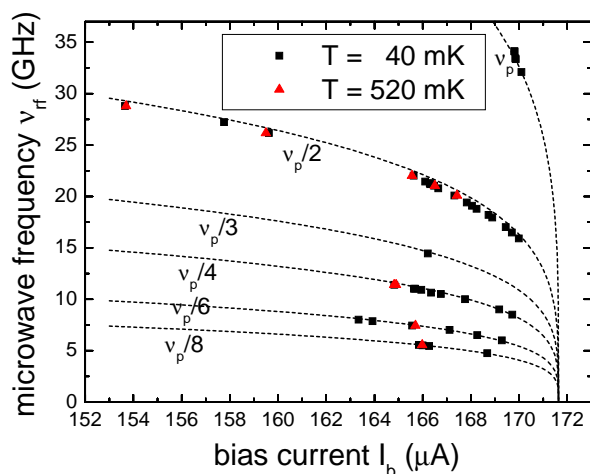


Figure 4: Microwave frequency vs resonance bias current. The dashed lines are calculated using Eq. (1) with the values of I_c and ν_{p0} obtained from the fit shown in Fig. 5.

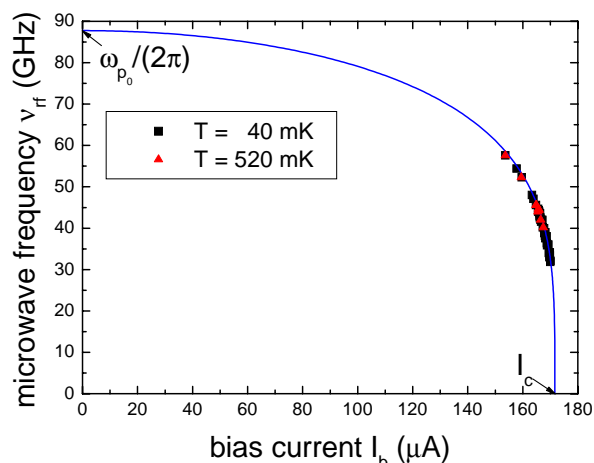


Figure 5: Data of Fig. 4 multiplied by the number of photons inducing the transition. The solid curve is a fit to Eq. (1) for $q = 1$. The arrows indicate the fitted plasma frequency $\omega_{p0}/(2\pi)$ and the fluctuation-free critical current I_c .

high temperature superconductor (HTS) grain boundary Josephson junctions. Such junctions are discussed for the realization of so-called quiet qubits involving π -phase shifters. However, so far an important open question is the influence of low lying quasiparticle excitations and the related damping in these junctions on their quantum behavior. Level spectroscopy is believed to give insight into this issue.

References

- [1] J. M. Martinis, M. H. Devoret, and J. Clarke, *Experimental test for the quantum behavior of a macroscopic degree of freedom: The phase difference across a Josephson junction*, Phys. Rev. B **35**, 4682 (1987).
- [2] Annual report 2004, Walther-Meissner-Institut, <http://www.wmi.badw.de/ueberuns/jahresberichte/2004.pdf>
- [3] M. V. Fistul, A. Wallraff, and A. V. Ustinov, *Quantum escape of the phase in a strongly driven Josephson junction*, Phys. Rev. B, **68**, 060504 (2003).
- [4] A. Wallraff, T. Duty, A. Lukashenko, and A. V. Ustinov. *Multi-photon Transitions between Energy Levels in a Current-Biased Josephson Tunnel Junction*, Phys. Rev. Lett. **90**, 037003 (2003).

Ferromagnetism in Cobalt Doped ZnO

K.-W. Nielsen, S. Bauer, M. Luebbe, J. Simon,¹ S. T. B. Gönnerwein, M. Opel, and R. Gross²

The field of magneto- or spin-electronics becomes increasingly important for commercial applications. For example, the high storage capacity of today's hard-disk drives would have been impossible without the development of read heads based on magneto-electronic concepts. Moreover, at present the feasibility of the magnetic random access memory (MRAM) is investigated vigorously by several companies. For future applications more complicated three-terminal devices such as spin transistors are envisioned. The common idea behind all these activities is to exploit both the charge *and* spin degree of freedom of electrons to arrive at spintronic devices with improved or novel properties that may be able to satisfy the continuously growing demands to devices used in our communication and information technology. Along this line, materials and/or technological concepts allowing to generate, manipulate, and detect spin-polarized charge carriers are of particular importance.

For spintronics diluted magnetic semiconductors (DMS) are very attractive materials. On the one hand they show long range ferromagnetic order and should have a high degree of spin polarization of the mobile charge carriers required for spin electronics. On the other hand they still have the versatile properties of semiconductors. For applications, DMS with ferromagnetic transition (Curie) temperatures T_C above room temperature are required. Therefore, the prediction of room-temperature ferromagnetism in transition-metal (TM) doped wide-bandgap semiconductors such as ZnO:Mn by Dietl *et al.* [1] triggered intense research activities. Indeed, ferromagnetic coupling at and above room temperature has been observed in e.g. ZnO:Co and ZnO:V [2]. However, these DMS show *n*-type (electron) conduction, whereas the theoretical prediction by Dietl *et al.* was based on *p*-type (hole) conduction and only very low ferromagnetic ordering temperatures were predicted for *n*-type semiconductors. Until today, the microscopic mechanisms responsible for the experimentally observed ferromagnetism are still discussed controversially. Suggestions range from the presence of local metallic clusters to ferromagnetic coupling of the transition metal spins via the states of an impurity band [2]. Within the latter model, the transition metal ions are assumed to hybridize with shallow impurity states forming bound magnetic polarons. To resolve the nature of the magnetic exchange in transition metal doped DMS, more detailed and systematic experiments are mandatory. In our work we concentrate on TM-doped ZnO. Here, the position of the transition metal-related energy levels in the ZnO band gap, as well as the exact nature of the impurity states are of particular interest.

We have grown thin $\text{Zn}_{0.95}\text{Co}_{0.05}\text{O}$ -films homoepitaxially on (0001)-oriented ZnO-substrates by pulsed laser deposition (PLD). The films were deposited at different temperatures ranging from 300°C to 600°C in Ar atmosphere. The film growth was monitored using in-situ RHEED. X-ray diffraction experiments show that the samples are of high structural quality, with no evidence for Co cluster formation. This observation is confirmed by detailed high-resolution transmission electron microscopy (TEM) studies (see Fig. 1).

The growth in reducing (Ar) atmosphere favors the formation of defects like oxygen vacancies or zinc interstitials, which act as shallow donors and are known to lead to *n*-type conductivity. If the density of these impurities is high enough, an impurity band can be formed, which is crucial for the occurrence of ferromagnetism following the model by Coey *et al.* [2]. The

¹Institut für Anorganische Chemie, Rheinische Friedrich-Wilhelms-Universität Bonn, 53117 Bonn

²This work is supported by the Deutsche Forschungsgemeinschaft via SPP 1157 (project No.: GR 1132/13).

presence of an impurity band in our samples is supported by the measured temperature dependence of the resistivity. As shown in Fig. 2, the resistivity rather saturates than diverges at low temperatures. Moreover, in the Arrhenius plot of Fig. 2, a linear variation of $\log \rho$ with $1/T$ corresponds to an electronic transport process following an activated behavior as

$$\ln \rho(T) = -\frac{E_a}{2k_B} \cdot \frac{1}{T} + \ln \rho_0, \quad (1)$$

where E_a is the characteristic activation energy and k_B is Boltzmann's constant. Fig. 2 suggests that there are two transport regimes (two regions with different slope) corresponding to activation energies $E_{a,h} < 1$ meV for $T \lesssim 50$ K, and $E_{a,g} = 10 - 30$ meV for $T \gtrsim 50$ K. It is tempting to attribute $E_{a,h}$ to the

hopping mechanism within the impurity band, while $E_{a,g}$ corresponds to the energy distance between the narrow impurity band and the lower edge of the conduction band. At low temperatures ($T \lesssim 50$ K) the charge carriers are frozen out into the impurity band and the transport is dominated by hopping within the narrow impurity band. At higher temperatures an increasing number of charge carriers is excited into the conduction band resulting in a decrease of resistivity.

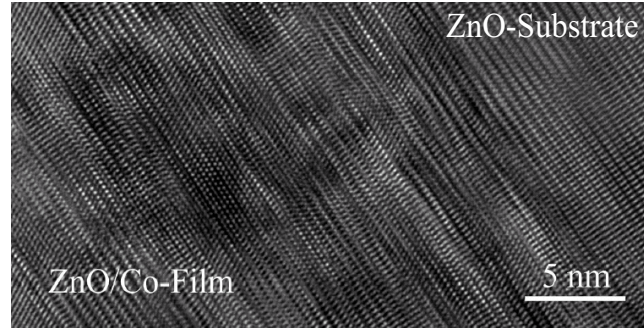


Figure 1: Transmission electron microscopy micrograph of a Co-doped ZnO film.

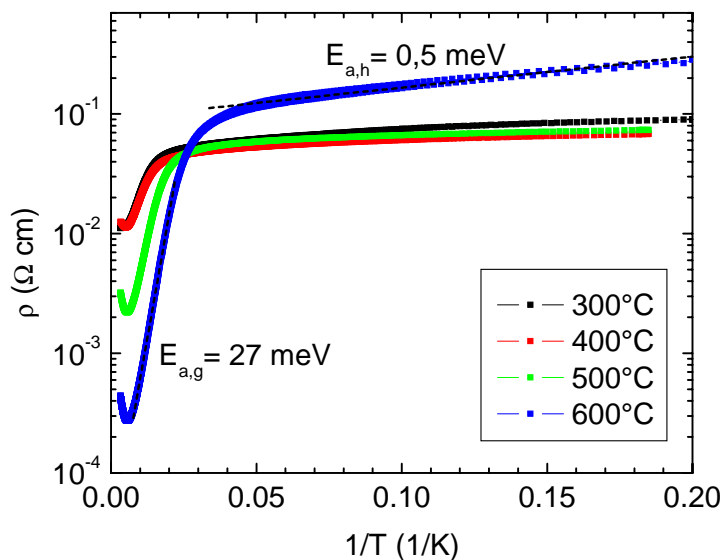


Figure 2: Resistivity versus temperature for Co-doped ZnO-films grown homoepitaxially on ZnO substrates at different temperatures.

The films range between about $0.2\mu_B/\text{Co}$ for $T_G = 300^\circ\text{C}$ and $0.4\mu_B/\text{Co}$ for $T_G = 500^\circ\text{C}$ after subtraction of the substrate contribution. The temperature dependence of the remanence is displayed in Fig 3b. In the corresponding experiments, the samples were first magnetized in a high field ($\mu_0 H = 7$ T) and then measured in zero field on increasing the temperature. Two regions with different temperature dependence are again evident at temperatures below and above about 50 K. It should be emphasized that the steep drop in $M(T)$ close to T_C , which is typically observed in conventional ferromagnets, is absent in our samples. Instead, the ferromagnetism decays rather continuously.

Two different temperature regimes are also observed for the magnetic properties of the films. The corresponding magnetization measurements are shown in Fig. 3. Note that the nominally undoped ZnO substrates used in our experiments contain paramagnetic impurities, which results in a substrate signal, which is explicitly shown in the figure for comparison. The magnetization of the films clearly is above the substrate level, with a well-developed ferromagnetic hysteresis, which varies with growth temperature T_G (see Fig 3a).

The electronic and magnetic properties of our $\text{Zn}_{0.95}\text{Co}_{0.05}\text{O}$ films summarized in Figs. 2 and 3 are qualitatively consistent with the model proposed by Coey *et al.* [2]. In particular, the ferromagnetic exchange seems to be closely linked to the electronic properties with two different temperature regimes. Moreover, no ferromagnetic behavior is observed, if the samples are grown in oxygen atmosphere resulting in the disappearance of the impurity band. Despite this apparent agreement with Coey's model, the key question still remains how the shallow impurity levels can effectively hybridize with the Co levels, which are expected to reside deep inside the band gap. To gain more insight into this question optical studies as well as spectroscopically resolved photoconductivity experiments are currently underway. These measurements should allow to pinpoint the cobalt-related energy levels in the ZnO band gap in our samples and to decide whether or not a hybridization between shallow impurities and transition metal orbitals can take place.

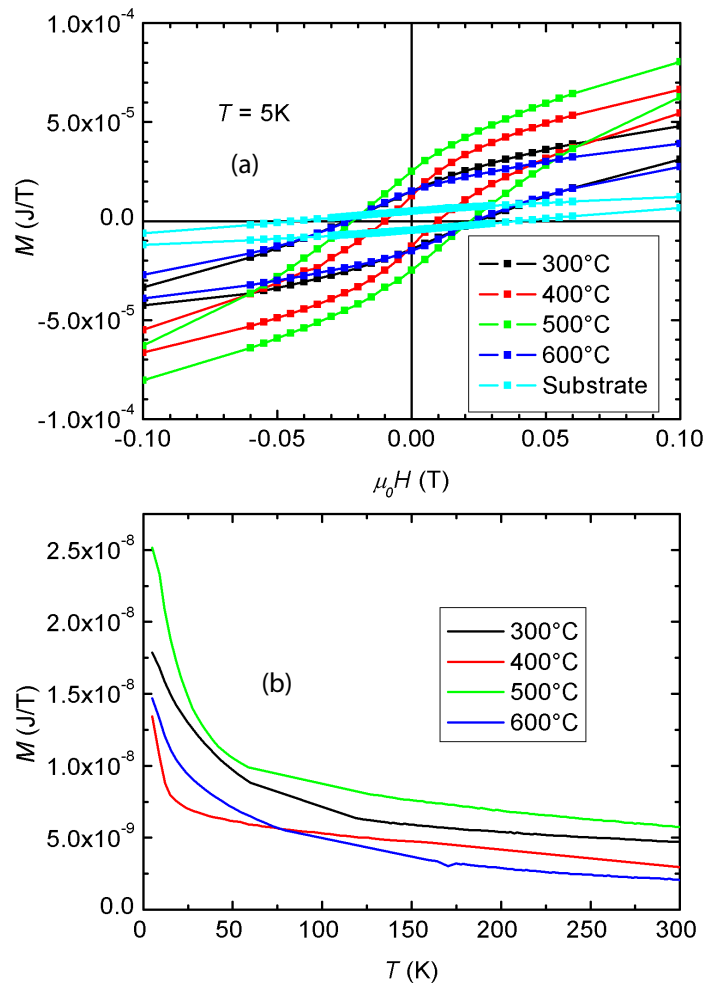


Figure 3: (a) Magnetization versus applied magnetic field of $\text{Zn}_{0.95}\text{Co}_{0.05}\text{O}$ films at $T = 5$ K. In (b) the temperature dependence of the magnetization measured at $H = 0$ A/m on increasing temperature after field cooling is shown. The diamagnetic contribution of the substrate has already been subtracted

References

- [1] T. Dietl, H. Ohno, F. Matsukara, J. Cibert and D. Ferrand, *Science* **287**, 1019-1022 (2000).
- [2] J.M.D. Coey, M. Venkatesan and C.B. Fitzgerald, *Nature Materials* **4**, 173-179 (2005).

Fabrication of Superconducting Flux Qubits

G. Wild, T. Heimbeck, B. Huber, M. Göppl, A. Marx, and R. Gross ¹

Quantum information (QI) theory and potential realizations of QI systems has become one of the most exciting topics in physics in recent years. The basic element of a QI processing unit is a quantum bit (qubit) consisting of a two level system with long enough decoherence time. Qubit behavior has already been realized by a large variety of two level systems for example in nuclear spins, ion traps, neutral atoms and also in different types of solid state based devices. Despite long enough coherence times scalability to QI processing units consisting of a large number of qubits is a central requirement imposed on the different qubit realizations. Here, solid state based devices could be advantageous because these systems can be scaled up using well established micro- and nanolithography techniques. Superconducting devices are especially attractive because the superconducting energy gap separates the ground state of the condensate from a large number of excited states, thereby minimizing possible decoherence sources. This points out the importance of using superconducting materials providing a large energy gap such as niobium.

Almost all superconducting qubits are based on Josephson junctions and sub-micron sized lateral dimensions requiring nanolithography. These structures can be fabricated using the well established aluminum shadow evaporation technique. On the other hand, niobium based Josephson junctions require more demanding multilayer technologies. By the insertion of π -phase bias elements into flux qubits the requirement of an externally applied magnetic flux bias to reach the degeneracy point is lifted. Josephson junctions based on niobium electrodes incorporating an additional ferromagnetic layer are one way to realize π -phase bias elements. Because of the aforementioned reasons we have on the one hand taken considerable efforts during the last year to establish a multilayer process to reproducibly fabricate niobium-based Josephson junctions both with and without ferromagnetic layers. On the other hand, the aluminum shadow evaporation technique has been further optimized. Here, the main focus was the optimization of the oxidizing process for defining the tunneling barriers and the realization of a well defined on-chip impedance seen by the qubit structures (on-chip capacitors, on-chip resistors).

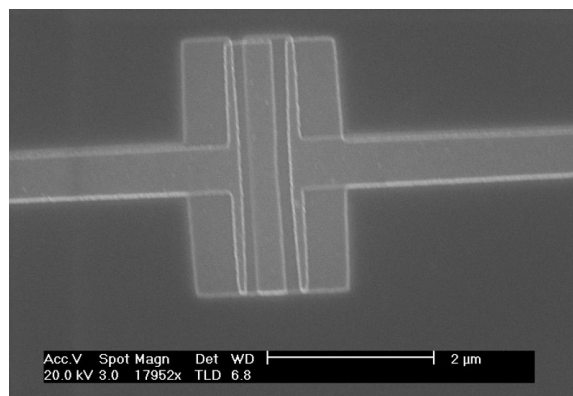


Figure 1: Josephson junction fabricated using aluminum shadow evaporation with 15 nm thick aluminum bottom layer and 25 nm thick top layer.

Aluminum technology: One approach to realize superconducting flux qubits is based on Al/AlO_x/Al Josephson junctions with sub-micron dimensions fabricated using shadow evaporation. This technique provides a well established process based on a single lithography step. The process is quite flexible with short turn around times and provides the possibility to easily fabricate and study different qubit design variants – even for nanosized device structures.

¹This work is supported by the DFG through the Cooperative Research Center 631.

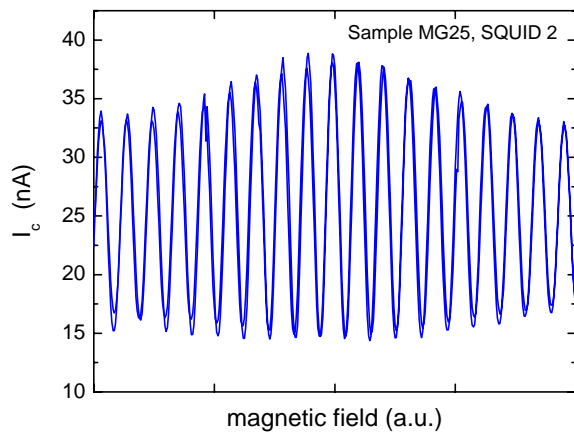


Figure 2: Dependence of the critical current on the applied magnetic field of an aluminum dc-SQUID fabricated using aluminum shadow evaporation technique.

able to produce structures containing Josephson junctions with lateral dimensions spanning a considerable interval. We have fabricated dc-SQUIDs which provide one means to read out a superconducting flux qubit showing the expected modulation of the critical current in an externally applied magnetic field (see Fig.2). Furthermore, we have implemented a mix-and-match technique, which allows to time-efficiently pattern the connecting lines and bonding pads via optical lithography in a first lithographic step, thereby reducing the scanning electron microscope (SEM) writing time by orders of magnitudes. By optimizing the deposition techniques for thin gold films which are used for bond pads and connecting structures the electrical and thermal resistivity could be reduced.

Presently, we are intensively working on the optimization and reliability of the oxidation process of the bottom aluminum layer. This oxide layer defines the tunnel barrier of the Josephson junction. Since the junction critical current density depends exponentially on the barrier thickness, this thickness has to be controlled with very high precision to fabricate junctions with the required critical currents. Here, the product of the oxygen partial pressure and the oxidation time has to be chosen correctly to get critical current densities of a few hundred A/cm^2 for the Josephson junctions. Furthermore, we have developed a process to fabricate on-chip capacitors, where the dielectric layer is defined in an extended oxidation process of the aluminum layer defining the lower capacitor electrode. The process to fabricate these on-chip capacitors is presently being combined with the aluminum shadow evaporation technique.

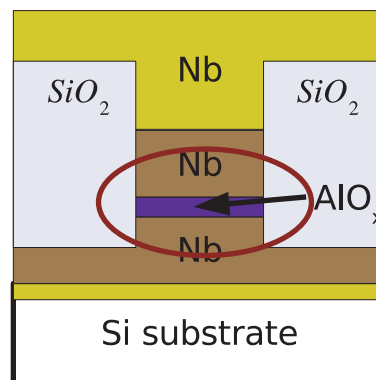


Figure 3: Schematic cross-sectional view of a multilayer structure fabricated with the process described in the text. The Josephson junction is defined by the oxidized aluminum in the mesa (marked in the red circle).

Niobium multilayer technology: High quality niobium Josephson junctions cannot be produced with the shadow evaporation technique using standard electron beam resists. Therefore, we have developed a multi-step lithographic process. In the first step a complete Nb/ AlO_x /Nb trilayer is deposited in-situ on an oxidized silicon substrate. A lift-off process is used to define the structure of the contacting lines ((1) in Fig. 4). Next, structure (2) is patterned around a mesa (3) using optical lithography. In this step the pattern transfer is performed using Reactive

Ion Etching. In the RIE process the trilayer structure is etched down to the bottom Nb layer except for the mesa area (3) which is covered by a resist stencil defining the actual junction area. After etching the same resist stencil is used to define an insulating sputter deposited SiO_2 layer around the mesa in a lift-off process. This layer acts as the insulation layer for the Nb wiring (4) of the top electrode, which is deposited in the last step. The actual Josephson junction is defined by the mesa structure etched into the trilayer structure as illustrated in Fig. 3.

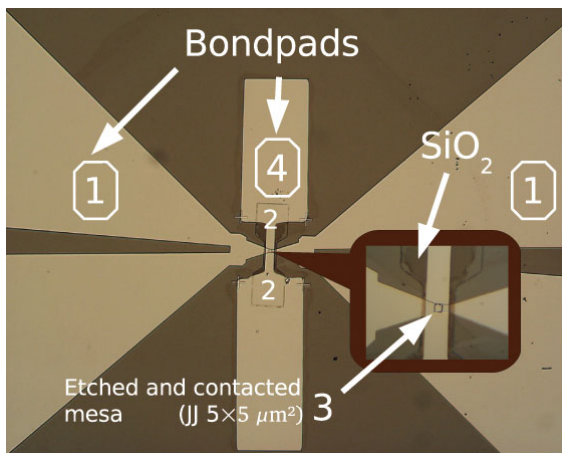


Figure 4: Optical micrograph of a Nb/ AlO_x /Nb Josephson junction fabricated by using a trilayer system which is deposited in-situ. The Nb/ AlO_x /Nb trilayer (1) is etched down to the first layer in the area defined by the contour (2) except for the mesa (3) defining the actual junction area. After covering the area defined by (2) with an insulating SiO_2 layer the Nb top electrode wiring (4) is defined. The junction area is $5 \times 5 \mu\text{m}^2$.

plement more sophisticated multilayer structures although it is technologically more challenging and time consuming. This flexibility allows to fabricate superconductor/ferromagnet/superconductor (SFS) or SNIFS (with an additional non-magnetic layer and insulating AlO_x layer) Josephson junctions. We plan to insert such Nb/ $\text{Al-}\text{AlO}_x$ / $\text{Ni}_{0.18}\text{Pd}_{0.82}$ /Nb junctions into flux qubit loops acting as π -phase-shift elements. In this way, the degeneracy (operating) point of flux qubits is shifted to zero applied magnetic flux instead of half an applied flux quantum which is presently required in the commonly used flux qubit designs.

In summary, the aluminum shadow evaporation technology has been optimized. We are now able to routinely fabricate circuits containing single Josephson junctions, SQUIDs and qubit. The critical current of the Josephson junctions and SQUIDs modulates in an external applied magnetic field as expected. Qubits have not yet been characterized. We further have established a multilayer process to fabricate niobium based Josephson junctions. The multidimensional parameter space for this fabrication process has still to be analyzed in more detail.

There are a few critical steps in this fabrication process. First, care has to be taken to guarantee electrical conduction along the niobium wiring layer of top electrode which is running across the sharp edges of the SiO_2 layer. Second, the surface of the Nb counter electrode within the mesa area has to be cleaned in-situ using an Ar ion beam to remove any oxide or contamination layer before the sputter deposition the Nb wiring layer (4) in order to guarantee a superconducting contact. Finally, the interface quality and especially the surface roughness of the individual layers of the trilayer structure are crucial parameters, since they are influencing the junction properties. The sputtering process has to be optimized for small surface roughness.

The fabrication process described above provides the possibility to im-

Dry Fridge Continued

K. A. W. Uhlig

A: Dilution refrigerator with high cooling power

In the past years we have constructed a $^3\text{He}/^4\text{He}$ dilution refrigerator which is precooled by a pulse tube refrigerator; it does not require any cryoliquids and is very cost efficient and easy to use. The advantages of this cooler have been described in detail elsewhere [1].

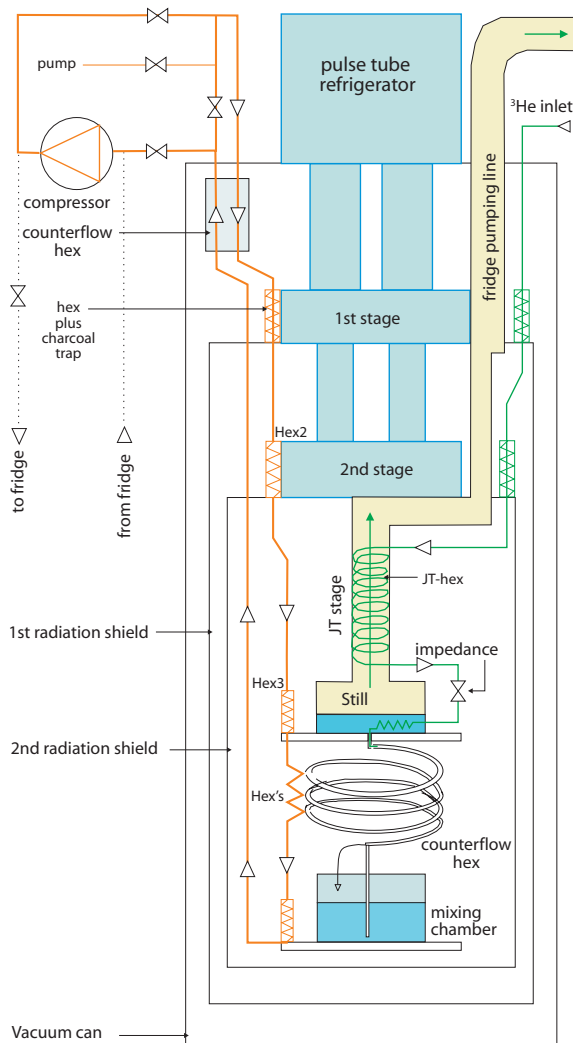


Figure 1: Cross sectional view of the cryostat and flow scheme for the dilution unit with precooling loop. For details see text.

In that respect, the heat exchanger of the Joule-Thomson stage (JT) is the most critical part (Fig. 1, yellow pumping line) of the pumping line.

Calculating the Reynolds number Re which is given by $Re = GD/\eta$ suggests that the flow in the low pressure line of the JT-heat exchanger is laminar ($G = 4m/\pi D^2$, with m being the mass flow, and D the hydrodynamic diameter; η : viscosity). So, one has a situation with conflicting

The cryostat consists of three parts, namely a commercial two-stage pulse tube refrigerator, a Joule-Thomson circuit and a dilution unit. We have given constructional details about those in various publications [1]- [3], and performance details on the pulse tube refrigerator can be found in the manufacturer's website [4]. We have demonstrated in the past that base temperatures near 4 mK can be reached with our dry fridge, and we could determine the integral heat leak into the mixing chamber of the fridge by using a so-called double mixing chamber [1]. We also demonstrated that the performance and the base temperature of the pulse tube refrigerator are not critical for the performance of the fridge; in fact, in one experiment we had installed a low cost pulse tube refrigerator which had only lead regenerators instead of the commonly used expensive rare-earth regenerators. The base temperature of this pulse tube refrigerator was 6 K (instead of 2.5 K) [5].

Last year we started a new project with the goal to increase the cooling power of the fridge. The cooling capacity of a dilution refrigerator is proportional to its ^3He throughput, and so it sounds like a straightforward task to construct a more powerful cooler. A pumping system with a higher pumping speed is needed, and one has to be sure that the pressure drop of the pumping lines is small so that the pressure in the still of the fridge is low (typically ~ 0.1 mbar). In that

requirements: On one side the flow resistance of the heat exchanger should be low to keep the pressure drop low, and so a heat exchanger with wide openings for the flow would be desirable. On the other hand, wide openings (compared to the thermal penetration depth) entail poor heat exchange – the gas flow passes through the heat exchanger without exchanging enthalpy. Thus, experimentally, the task is to find a construction which is a compromise between those requirements.

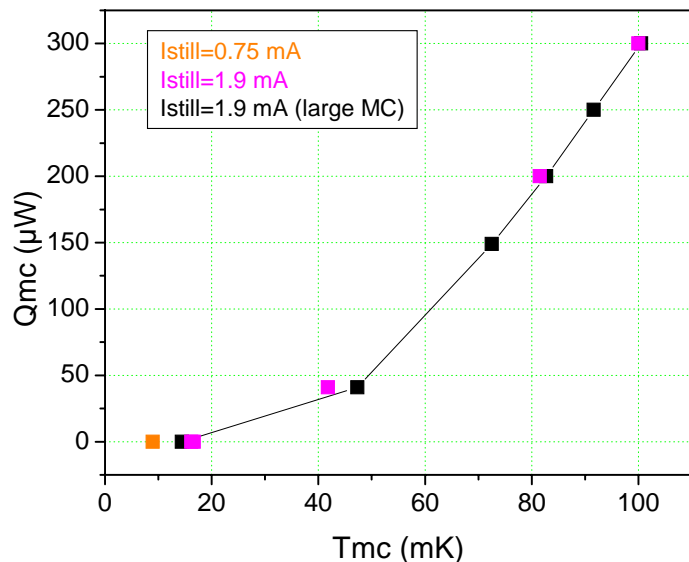


Figure 2: Cooling power of the dilution refrigerator at a flow rate of $500 \mu\text{mol}/\text{sec}$. The orange point is the base temperature at a flow rate of $200 \mu\text{mol}/\text{sec}$.

experiments where we had used a smaller turbo pump to circulate the ^3He . For thermometry two calibrated resistance thermometers were used [7]. The cooling capacity of the mixing chamber after those changes is depicted in Fig. 2. Cooling power measurements as a function of mixing chamber temperature are given for two experiments; only the volume of the mixing chamber was different in those experiments. The cooling capacity at 100 mK was $300 \mu\text{W}$ compared to $150 \mu\text{W}$ before. The lowest temperature of the mixing chamber was 9 mK at a reduced ^3He flow ($200 \mu\text{mol}/\text{s}$). It appears that the ^3He flow can be increased even more and the cooling capacity increased accordingly.

B: Precooling Cycle

Usually, at the beginning of an experiment, our dilution unit is cooled by the pulse tube refrigerator from room temperature to a temperature of 10 K in a can with hydrogen exchange gas. In some applications, however, like atom or electron beam experiments this is not possible; in these cryostats the dilution unit is in the vacuum space of the cryostat and has to be cooled from room temperature by some sort of thermal switch. We were faced with this problem in connection with our collaboration with VeriCold Inc. [8]. We chose to use a precooling cycle similar to the one we had constructed years ago for a different purpose [9]. To cool the components of the fridge a separate cycle with helium gas was built into the cryostat where each component of the fridge is cooled by heat exchangers which are part of the cycle (see Fig. 1, orange lines). To circulate the gas a little compressor was used; this compressor was needed later on for the condensation process of the $^3\text{He}/^4\text{He}$ mixture, as well.

During cooldown, the gas flow is cooled in heat exchangers at the first and the second stage of the pulse tube fridge and then the gas stream cools the still, the counterflow heat exchangers

In comparison to previous work a new JT-heat exchanger was made where the diameter of the outer tube was increased, and the construction of the insert was modified [6]. A bigger pump (Pfeiffer $1000 \text{ m}^3/\text{h}$) was installed, and the flow restriction and the counterflow heat exchanger were exchanged to allow for higher ^3He flow (Fig. 1). Besides, the fridge was equipped with two concrete heat exchangers (no temperature gradient across the exchanger) which are located between the counterflow heat exchanger and the mixing chamber (not shown in Fig. 1). After these measures the ^3He throughput could be increased by a factor of 2 in comparison to experi-

and the mixing chamber. The enthalpy of the outflowing stream is used in a counterflow heat exchanger to precool the gas of the return line. Once all components of the dilution unit are cooled to ≈ 15 K, the helium gas has to be pumped out of the precooling cycle, and the condensation of the $^3\text{He}/^4\text{He}$ mixture can begin.

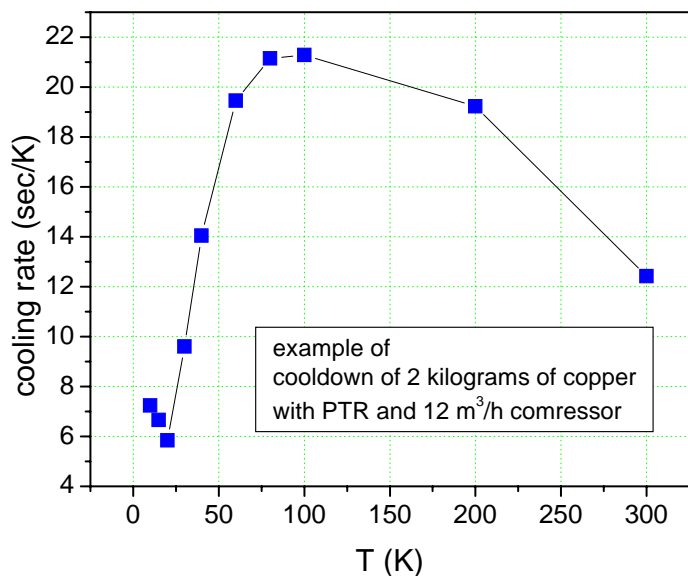


Figure 3: Example for the calculated cooldown rate of our precooling circuit.

cryostat which is about 10 hours. The cooldown loop worked well from the beginning and was never changed.

In summary, it could be demonstrated that dilution refrigerators with high cooling capacity can be built with pulse tube refrigerator precooling. Additionally, we showed how to construct a dry fridge where the cooldown from room temperature is accomplished by a precooling cycle with helium gas.

Finally we mention that our latest paper on a “dry” fridge [1] was awarded the CRYOGENICS-2004 prize for the best paper in this magazine in 2004.

References

- [1] K. Uhlig, “Dry” dilution refrigerator with pulse-tube precooling, *Cryogenics* **44**, 53 (2004).
- [2] K. Uhlig, $^3\text{He}/^4\text{He}$ dilution refrigerator with pulse-tube refrigerator precooling, *Cryogenics* **42**, 73 (2002).
- [3] K. Uhlig, $^3\text{He}/^4\text{He}$ dilution refrigerator precooled by Gifford-McMahon cooler II. Measurements of the vibrational heat leak, *Cryogenics* **42**, 569 (2002).
- [4] www.cryomech.com
- [5] K. Uhlig, C. Wang, *Cryogen-free dilution refrigerator precooled by a pulse tube refrigerator with non-magnetic regenerator*. Advances in Cryogenic Engineering, CEC-ICMC 2005, Keystone (Co), USA, to be published
- [6] K. Uhlig, $^3\text{He}/^4\text{He}$ dilution refrigerator without a pumped ^4He stage, *Cryogenics* **27**, 454 (1987).
- [7] K. Uhlig, Magnetoresistance of thick-film chip resistors at millikelvin temperatures, *Cryogenics* **35**, 525 (1995).
- [8] www.vericold.com
- [9] K. Uhlig, Thermal shunt for quick cooldown of two-stage closed-cycle refrigerator, *Cryogenics* **42**, 67 (2002).

To design the loop, reasonable assumptions were chosen for the flow rate (which is given by the specs of the compressor) and the dimensions of the heat exchangers and capillaries. For a typical inlet pressure of 4 bar we have turbulent flow in the loop ($Re \sim 4000$) which is desirable for good heat exchange. Then one can calculate the cooldown rate for the dilution unit, and by integration of the cooldown rate the cooldown time can be calculated. Note that below 25 K the circulation rate was reduced in our model which caused a kink in the data (Fig. 3). In our model a cooldown time of 1.4 hours is found. This time is short compared to the cooldown time of the

Single Crystal Growth of Cuprate Superconductors

Andreas Erb and Michael Lambacher¹

In 2004 the Deutsche Forschungsgemeinschaft (DFG) established the Research Unit FOR 538 "Doping Dependence of Phase Transitions and Ordering Phenomena in Cuprate Superconductors" consisting of altogether 7 independent projects, one of which is "Crystal Growth of *p* and *n*-doped cuprate superconductors". The goal of this project is the growth and characterization of high purity single crystals of the high temperature superconductors to provide samples for different spectroscopic experiments within the DFG Research Unit. In order to cover the whole phase diagram of the high-temperature superconductors, which is the main idea of this research project, crystals with well defined and homogeneous doping levels of both *p* (hole) and *n*- (electron) doped compounds need to be grown.

The available sample systems on the *p*-doped side of the phase diagram are mainly the 123 ($\text{REBa}_2\text{Cu}_3\text{O}_{6+x}$, RE=Y, Nd, Gd etc.) and the Bi-2212 ($\text{Bi}_2\text{Sr}_2\text{CaCu}_2\text{O}_{8+\text{ff}}$) compounds with different doping levels.

$\text{YBa}_2\text{Cu}_3\text{O}_{7-\delta}$

Single crystals of the 123-superconductors are grown out of high temperature solutions in inert BaZrO_3 crucibles developed especially for this purpose [1, 2], which allow the growth of crystals with purities up to 99.995 at.%. Hence, the purities which can be achieved are at least one order of magnitude higher than those grown in commercially available crucibles like ZrO_2 . This means a major advantage when the doping dependence is to be studied. To vary the doping in the 123-compounds over a wider range Y-123 crystals with Y partially replaced by Ca have been grown. Simultaneous doping with Ca and oxygen extends the accessible doping range for the 123-compounds. We point out that $\text{YBa}_2\text{Cu}_3\text{O}_{6+x}$ is the only copper-oxygen compound which exists at the stoichiometric cation composition making it ideally suited to probe the phase diagram. Unfortunately, not the whole doping range can be accessed using this compound alone.

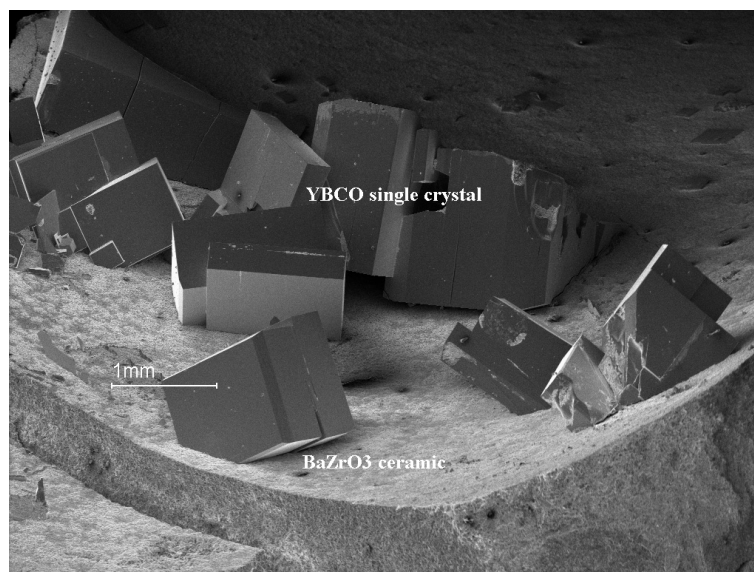


Figure 1: Single crystals of the high temperature superconductor $\text{YBa}_2\text{Cu}_3\text{O}_{7-\delta}$ inside a BaZrO_3 crucible.

¹This work is supported by the DFG via Research Unit 538 ("Doping Dependence of Phase Transitions and Ordering Phenomena in Cuprate Superconductors") under the grant number ER 342/1-1.

Bi-2212 ($\text{Bi}_2\text{Sr}_2\text{CaCu}_2\text{O}_8$), Bi-2201 ($\text{Bi}_2\text{Sr}_2\text{CuO}_6$) and Bi-2223 ($\text{Bi}_2\text{Sr}_2\text{Ca}_2\text{Cu}_3\text{O}_{10+\delta}$)



Figure 2: The 4-mirror image furnace at the WMI. The maximum temperature is approximately 2200°C at a pressure up to 10 bar. Surfaces required for the various surface sensitive spectroscopies (angle resolved photoemission, Raman and infrared spectroscopy) can be prepared conveniently.

The Bi-based compounds are grown in the mirror furnace shown in Fig. 2 by the container-free traveling solvent floating zone technique (TSFZ). Typical single crystals of the high-temperature superconductor $\text{Bi}_2\text{Sr}_2\text{CaCu}_2\text{O}_8$ grown by the traveling-solvent-floating-zone (TSFZ) technique in the mirror furnace of the WMI are shown in Fig. 3. Samples of the compound Bi-2212 allow us to cover a broad range of the phase diagram of the cuprates on the p -doped side, especially with additional doping by trivalent Yttrium or Dysprosium partially replacing bivalent Calcium. We now routinely grow Bi-2212 single crystals with a size of several centimeters in length.

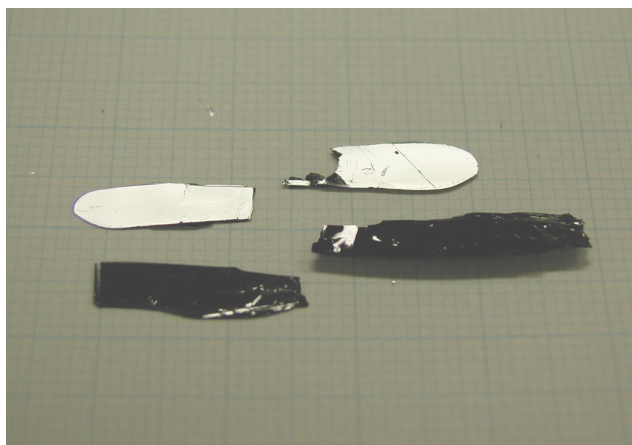


Figure 3: Single crystals of the high-temperature superconductor $\text{Bi}_2\text{Sr}_2\text{CaCu}_2\text{O}_8$ grown by the traveling-solvent-floating-zone technique in the mirror furnace.

Besides 123 the Bi-based compounds are interesting high- T_c materials, which also allow to study the phase diagram in a wider range. The family of the Bi-based high- T_c materials consists of 3 compounds: the so-called single-layer compound $\text{Bi}_2\text{Sr}_2\text{CuO}_6$ with a maximum transition temperature of $T_c \simeq 20$ K, the double-layer compound $\text{Bi}_2\text{Sr}_2\text{CaCu}_2\text{O}_8$ with a T_c^{max} of about 95 K and the triple-layer compound $\text{Bi}_2\text{Sr}_2\text{Ca}_2\text{Cu}_3\text{O}_{10+\delta}$ with a $T_c^{\text{max}} \simeq 110$ K. Especially double-layer Bi-2212 is of high interest for the research projects within the DFG Research Unit, since the crystals cleave very easily parallel to the CuO_2 planes. Hence, fresh surfaces required for the various surface sensitive spectroscopies (angle resolved photoemission, Raman and infrared spectroscopy) can be prepared conveniently.

214-compounds: $\text{La}_{2-x}\text{Ce}_x\text{CuO}_{4+\delta}$, $\text{Nd}_{2-x}\text{Ce}_x\text{CuO}_{4+\delta}$ and $\text{Pr}_{2-x}\text{Ce}_x\text{CuO}_{4+\delta}$

On the n -doped side of the phase diagram only the so-called rare earth (RE)214-compounds are available. These compounds are solid solutions with a simple tetragonal crystal structure. The undoped $\text{RE}_2\text{CuO}_{4+\delta}$ parent systems are antiferromagnetic insulators which can be driven superconducting by substituting trivalent rare earth ions RE^{3+} with bivalent ions like Sr^{2+} on the p -doped side or by tetravalent ions like Ce^{4+} on the n -doped side of the phase diagram. Note, that the two hole doped 214-compounds $\text{La}_{2-x}\text{Ba}_x\text{CuO}_{4+\delta}$ and $\text{La}_{2-x}\text{Sr}_x\text{CuO}_{4+\delta}$ were the first cuprate superconductors found [3].

In addition to x , the oxygen concentration δ is an important quantity in n -doped compounds, since excess oxygen in interstitial positions of the crystal structure acts as a pinning potential for the doped electrons. In order to get the n -doped crystals superconducting they have to be annealed after the growth process to remove the interstitial oxygen. However, this annealing treatment can lead to an inhomogeneous oxygen distribution. Decomposition of the system might result if the reduction treatment is too strong. We developed a better annealing treatment to avoid these problems and to get sharp transitions to the superconducting state at high T_c (see Fig. 4).

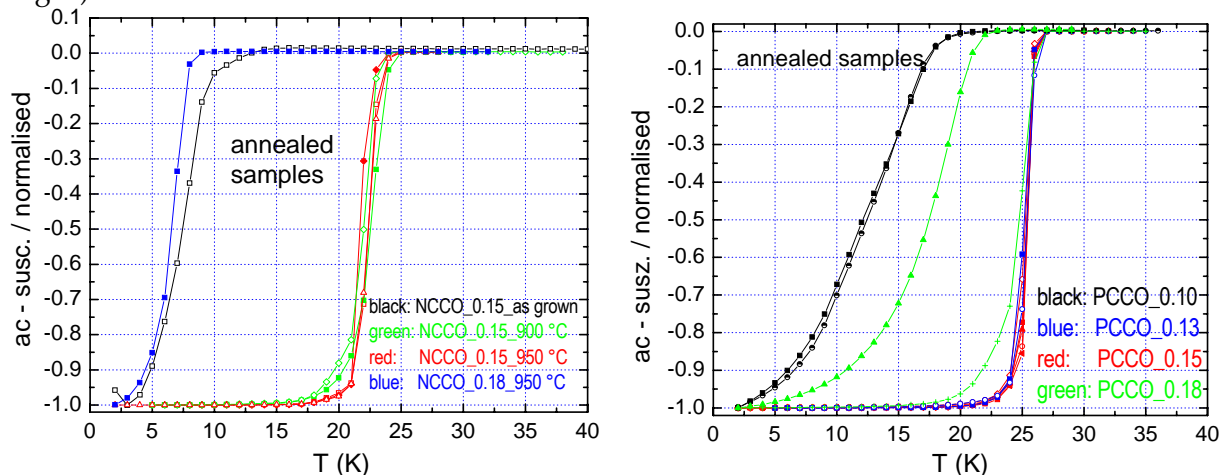


Figure 4: ac-susceptibility curves for $\text{Nd}_{2-x}\text{Ce}_x\text{CuO}_{4+\delta}$ (left) and $\text{Pr}_{2-x}\text{Ce}_x\text{CuO}_{4+\delta}$ single crystals (right). The doping level x does not only affect the magnetic and transport properties properties of the $\text{RE}_{2-x}\text{Ce}_x\text{CuO}_{4+\delta}$ compounds but also the stability of the growth process and the quality of the resulting material concerning, e.g., the homogeneity of the cerium distribution.

All these compounds are prepared by the TSFZ technique. The grains grow along the crystallographic $\langle 110 \rangle$ -orientation, and the $\langle 001 \rangle$ -axis is perpendicular to the growth direction. An as-grown single crystal rod of $\text{Pr}_{1.85}\text{Ce}_{0.15}\text{CuO}_4$ as well as a photo taken during the crystal growth are shown in Fig. 5.

In order to get high quality $\text{RE}_{2-x}\text{Ce}_x\text{CuO}_{4+\delta}$ single crystals the growth parameters have been optimized during the last year. Especially the atmosphere and the corresponding temperature, which we use for the crystal growth, correlate with the doping level x of the compound. We are now able to grow all the above-named 214-compounds with different doping x . At the moment our work is focused more on the compounds $\text{Pr}_{2-x}\text{Ce}_x\text{CuO}_{4+\delta}$ and $\text{Nd}_{2-x}\text{Ce}_x\text{CuO}_{4+\delta}$ as $\text{La}_{2-x}\text{Ce}_x\text{CuO}_{4+\delta}$ does not crystallize in the desired crystal structure. PCCO and NCCO differ in the Ce-solubility limit. For $\text{Nd}_{2-x}\text{Ce}_x\text{CuO}_{4+\delta}$ we get precipitations of a secondary phase, if the doping level x exceeds 0.18, whereas the limit for $\text{Pr}_{2-x}\text{Ce}_x\text{CuO}_{4+\delta}$ is 0.15. Therefore, it is quite difficult to cover the overdoped range for $\text{Pr}_{2-x}\text{Ce}_x\text{CuO}_{4+\delta}$. Both systems show the highest T_c at $x = 0.15$, and there is only a small region around this optimum doping, where the

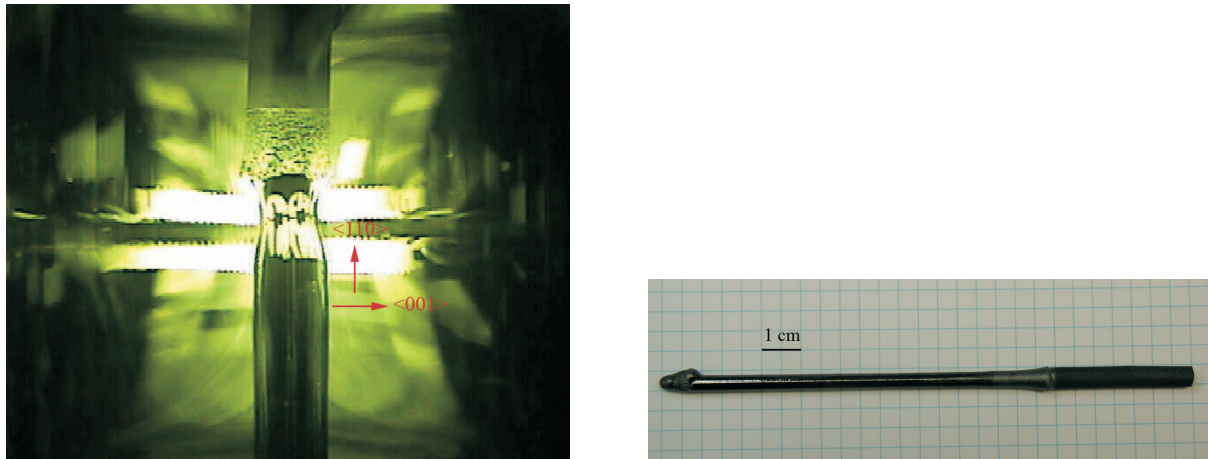


Figure 5: Left: growth of a $\text{Pr}_{1.85}\text{Ce}_{0.15}\text{CuO}_4$ crystal in the mirror furnace. The dissolving feed rod (top), the molten solvent zone (middle) and the slow-growing crystal (bottom) are well represented. Right: Photograph of an as-grown $\text{Pr}_{1.85}\text{Ce}_{0.15}\text{CuO}_4$ single crystal.

compounds are superconductive.

In conclusion, all the relevant compounds necessary to study the phase diagram of the cuprate superconductors, on both the p - and the n -doped side, can now be grown in the crystal laboratory of the Walther-Meissner-Institute.

References

- [1] A. Erb et al. *Physica C* **245**, 245 (1995).
- [2] A. Erb, E. Walker, R. Flükiger. *Physica C* **258**, 9 (1996).
- [3] J. G. Bednorz and K. A. Müller. *Z. Phys. B* **64**, 189 (1986).

Scanning Probe Division of the WMI

B. A. Hermann¹

The new division "Scanning Probe Microscopy" headed by B. A. Hermann, a C3-Professor of the LMU and member of the Center for NanoScience (CeNS), operates a low temperature STM since end of the year 2004. A microprocessor controlled three crucible evaporator for organic substances, was delivered and installed in 2005. This evaporator can be refilled without breaking the main vacuum.

Why Scanning Probe Microscopy at Low Temperatures

At low temperatures the mobility of single atoms, molecules, or weakly bound clusters on a surface is strongly reduced, allowing a more detailed analysis of their chemical and physical interactions as well as their diffusive behavior. Most quantum phenomena, like superconductivity, only occur at temperatures far below ambient. Additionally, it is possible to investigate temperature dependent 2-D ordering phenomena such as phase transitions or, e.g., freezing of rotations. On top of that the performance of the equipment is considerably improved concerning instrument noise and thermal drift. In the following, the low temperature scanning tunneling microscope (STM) is described along with other analytic and preparation possibilities.

Low Temperature STM

In the Walther-Meissner-Institute now a low temperature scanning tunneling microscope (top picture) is operating for the investigation of low dimensional systems such as self-organized molecules or superconductor, magnetic and heterostructure surfaces. The STM has been designed to meet the special requirements of a wide variety of collaborations. It comprises:

- in-situ sample and tip exchange,
- optimal vibration isolation ensured by a spring suspension system with eddy current damping and pneumatic damping legs,
- variable temperatures from 5 K (pumped 2 K) up to room temperature (~ 300 K),
- fast system cool-down ($T = 5$ K within ~ 6 hours),
- fast sample cool-down ($T = 5$ K within ~ 2 hours),
- UHV condition,
- optical access,

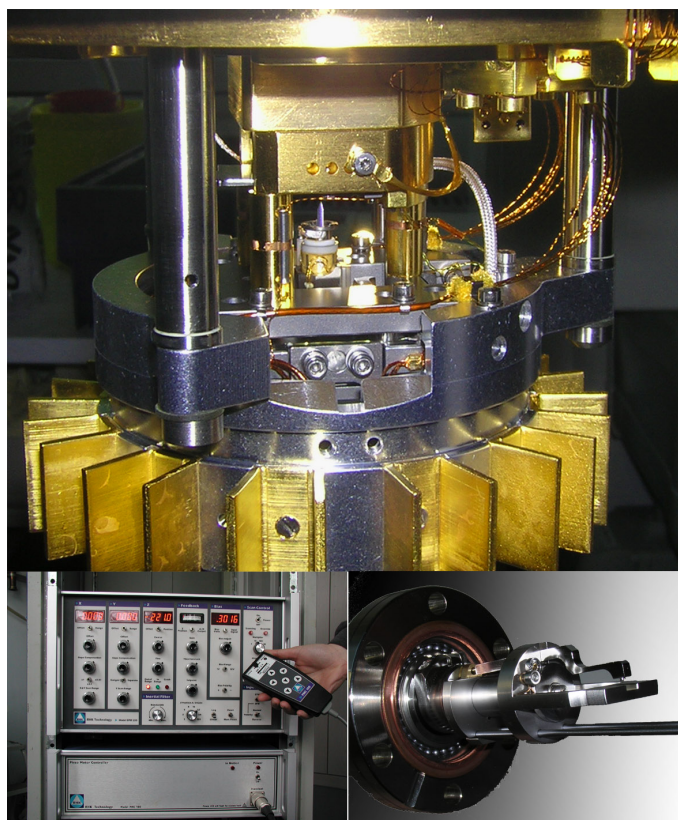


Figure 1: Top: low temperature STM, bottom left: scan electronics, bottom right: manipulator

¹The Omicron LT-STM and preparation chamber is supported by the Center for Nano Science (CeNS), Ludwig-Maximilians-University and the Bavarian State as well as the German Federal Government via the HBFG program. The laboratory infrastructure comes from the WMI.

- four terminal transport measurements,
- RHK open scan electronic system.

Preparation and Further Analysis

Docked to the analysis chamber containing the Omicron-STM (top picture: the tower to the left) is a preparation chamber (top picture: to the right and bottom picture). Inside this separate chamber clean single crystalline substrates can be prepared by ion-sputtering and subsequent thermal annealing, which is controlled by a three grid low energy electron diffraction (LEED) (bottom picture) in a vacuum of 10^{-11} mbar.

The surface ordering of (reconstructed) substrate/single crystal surfaces or molecular ad-layers can also be analyzed by LEED.

Samples can be additionally characterized by desorption spectroscopy with a quadrupole mass spectrometer. The desorbing molecules are ionized in a crossbeam ion source and accelerated in the quadrupole mass spectrometer, which either uses a Faraday cup or secondary electron multiplier (SEM) as detector with a mass resolution up to 2048 amu. The preparation facilities allow a direct current heating and a indirect heating from the back of the sample up to 800°C and sample cooling down to 50 K on the manipulator (top picture: far right). Multiple additional vacuum ports allow further extensions in the future.

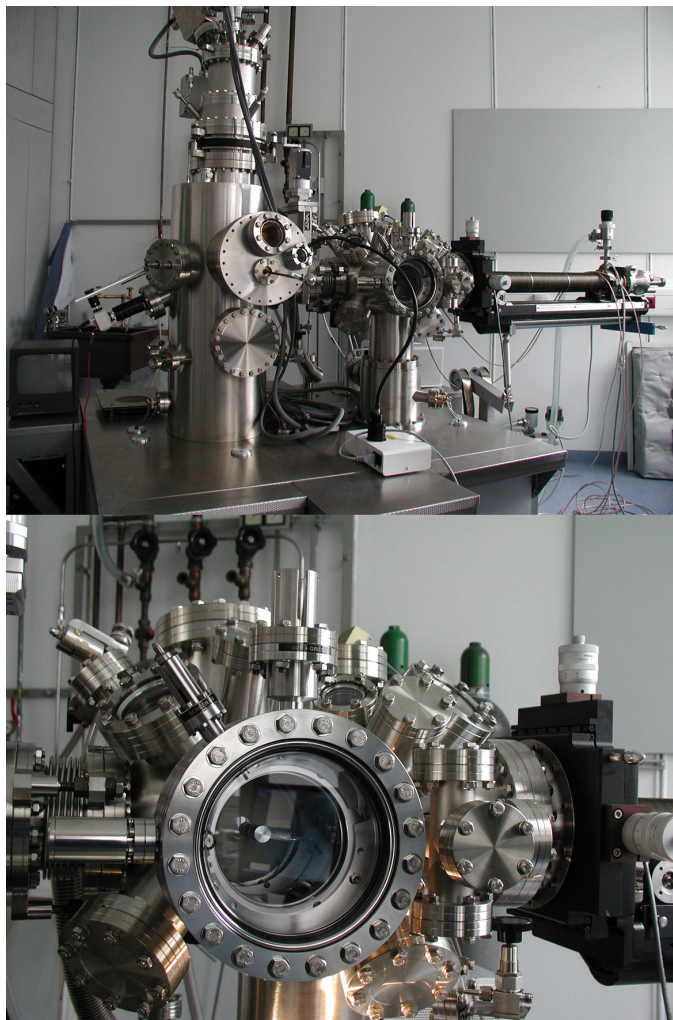


Figure 2: top: entire setup viewed from the main operation side, bottom: LEED system enlarged.

Research Interests

The research interests of the new division of scanning probe microscopy at the WMI range from oxides over nanostructures to large (bio)molecules – spectroscopy and imaging: A layered material (oxide, e.g. high- T_c -superconductor), a lithographically created nanostructure, or (self-organized) large (bio)molecules have material properties that radically differ from those of solids. The physics and (bio)chemistry takes place (at least concerning one of three dimensions) on the nanoscale. Besides the basic understanding of the physics and chemistry of those nanoscale materials, the investigations are primarily motivated by their application: how can measurements of the structure or electronic properties (superconductivity, transistor effect, diode characteristics) help to tune material properties? Which role do defects play? How does the system behave at various temperatures?

The New Helium-Liquefier at the WMI

*J. Höß*¹

In December 2004 the new Helium-Liquefier, a Linde TCF20 type, became fully operational. Since then 127 000 l Helium have been liquefied and supplied to the various research facilities of the Munich universities. The fully computer controlled and automatically working TCF20 Helium liquefier has a capacity of 27 and 58 l/h without and with liquid nitrogen (LN2) pre-cooling, respectively. The main components are:

Käser DSD 201 oil injected rotary screw compressor:

The compressor (see Fig. 1), with a power consumption of 110 kW instead of 170 kW of the old piston compressor, is air cooled via a radiator implying that there is no need for expensive cooling water. Approximately 14 000 m³/h air is circulated by a fan integrated in the compressor. The screw compressor and the motor have a direct torsional-elastic coupling without gear and transmission. In this way, the number of rotating components, the sound level, the vibrations, and



Figure 1: Compressor unit of the new liquefier. The important parts are indicated.

the energy consumption are reduced in comparison to the piston compressor. A component essential for the operation of the compressor is an efficient oil separation system. The oil is separated from the compressed helium by centrifugal forces in the separator tank. The oil mist in the compressed helium is removed by a second separation system outside the compressor. Here, residual oil is removed from the helium by two coalescers and an oil vapor charcoal adsorber, to ensure that oil does not contaminate the liquefier. In this way the oil concentration can be reduced to a level of less than 0.3 ppm. All functions of the compressor are controlled by a "sigma" control with alpha-numeric display and clearly marked navigation and input keys.

Coldbox: The pure high-pressure gas is fed into the coldbox and cooled in the first heat exchanger, which is equipped with passages for liquid nitrogen cooling. After passing the second heat exchanger the gas flow is divided into two streams. The larger stream passes the first turboexpander, then at medium pressure the gas enters heat exchanger number 3 and is finally expanded to low pressure in the second turboexpander. The low-pressure gas returns via heat exchangers to the compressor. The remaining stream is cooled in heat exchangers, passes a guard adsorber to remove impurities such as neon, and is finally expanded through a Joule-Thomson valve and an ejector to low pressure, where it is partially liquefied. The two-phase mixture is then fed to the dewar inside the coldbox, where the liquid helium is separated from the vapour. The cold gas returns through the heat exchanger to the compressor inlet.

¹The liquefier was funded by the State of Bavaria and the German Federal Government.

Turboexpanders: Very important parts in the coldbox are the gas bearing turboexpanders (see Fig. 2). Each consists of a small single-stage centripetal turbine that drives a directly coupled single-stage centrifugal brake compressor. The turbine is equipped with self-acting gas bearings. The lubrication of the bearings works automatically during all operation modes of the liquefier. Furthermore, self-acting bearings run very stable and are extremely reliable since they require no external gas supply from the control system. The main components of the turbine are the turbine itself, the rotor, the bearings and the brake compressor. The turbine housing is attached to the valve plate of the coldbox and projects vertically into the vacuum space of the cold box. The bearing and the compressor operate at ambient temperature. The turbine speed is measured by a magnetic induction sensor, converted into standard electronic signals and fed to a control valve at the brake compressor circuit. The work, the turbine withdraws from the process stream is transferred into the brake compressor circuit and rejected as heat to the cooling water in a helium gas-to-water heat exchanger.

Siemens S7-400 computer: A Siemens S7-400 computer controls all functions of the coldbox. The man-machine interface is an operator panel at the local control board with alphanumeric display and clearly marked navigation and input keys. Additionally, the liquefier is equipped with a remote monitoring and control system based on a standard personal computer.

Big advantages of the new liquefier are the possibility to switch on and off the liquid nitrogen pre-cooling at any time during all operating modes to manipulate the liquefaction rate and the lower running costs in comparison to the old piston compressor.

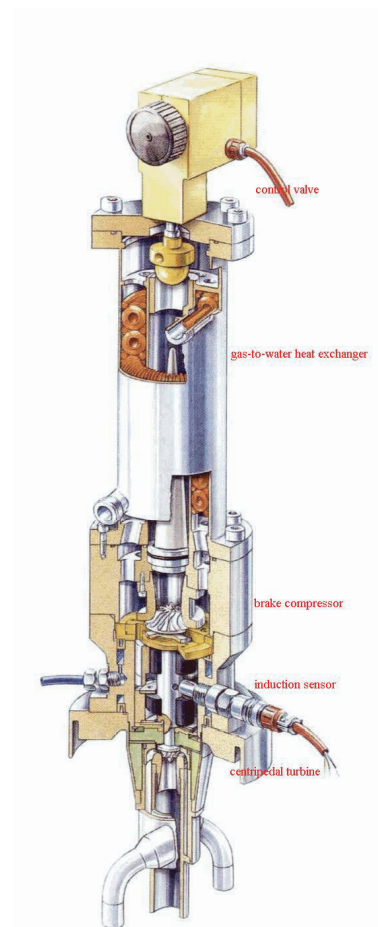


Figure 2: Cross-sectional view of the turboexpander of the Linde TCF 20.

Experimental Facilities and Infrastructure

Within the last years, several new experimental facilities and various components of the technical infrastructure have been installed at the Walther-Meißner-Institute. On the following pages a brief overview is given on the main equipment and techniques that are available at the Walther-Meißner-Institute at present.

UHV-Laser-MBE

The Walther-Meißner-Institute operates a UHV-Laser-Molecular Beam Epitaxy (L-MBE) system for the growth of complex oxide heterostructures. The system has been designed to meet the special requirements of oxide epitaxy. The UHV cluster tool consists of the following main components:

- central transfer chamber.
- load-lock chamber with heater system for substrate annealing.
- laser deposition chamber with in-situ reflection high energy electron diffraction (RHEED) system, laser substrate heating system, and atomic oxygen source. The RHEED system has been modified to allow for the operation at high oxygen partial pressure up to 0.5 mbar.
- sputter deposition chamber with four UHV magnetrons and in-situ ion beam cleaning of substrates
- surface characterization chamber with UHV scanning force microscope (Omicron).
- metallization chamber with a four heart electron gun system and a liquid nitrogen cooled sample stage. The sample holder can be tilt for shadow evaporation.
- KrF excimer laser.

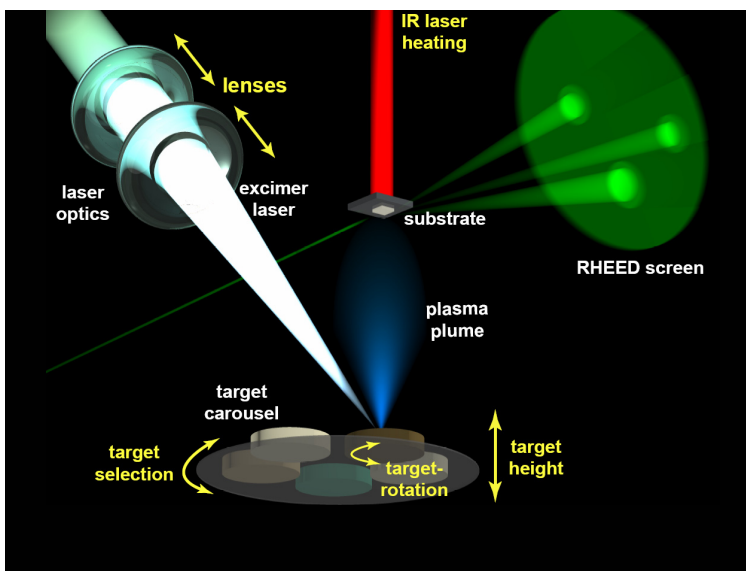
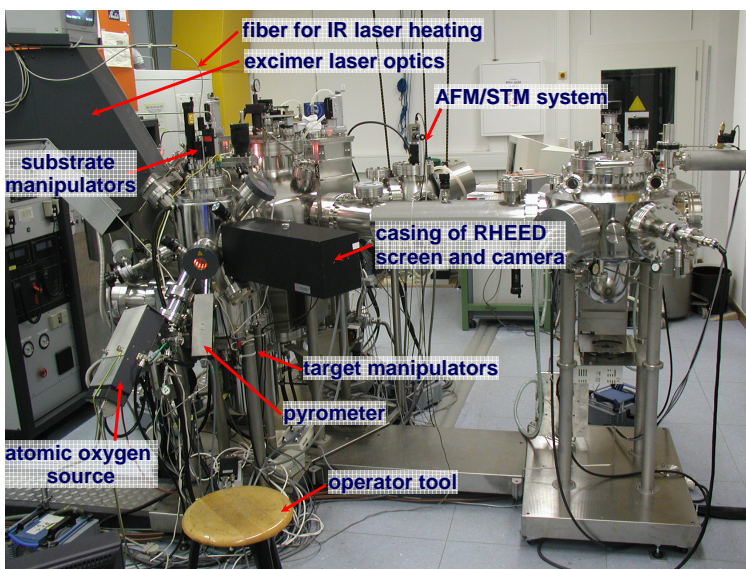


Figure 1: Top: UHV-Laser-Molecular Beam Epitaxy System. Bottom: Sketch of the principle of UHV pulsed laser deposition with in-situ RHEED control.

The system is used for the growth of complex oxide heterostructures consisting of superconducting, magnetic and dielectric materials such as the high-temperature superconductors, the

doped manganites, the double perovskites, magnetite etc.. In 2004 a UHV sputtering chamber with 4 magnetrons was added to the cluster allowing the sputter deposition of metallic multilayer structures and the combination of oxide and metallic materials systems.

During 2002 and 2003, the laser molecular beam epitaxy system (laser-MBE) which was installed at the Walther-Meißner-Institut during 2001 has been extended and modified. In particular, the substrate heating system and the temperature control unit was changed from a resistive radiation heater to a new infrared laser heating system (see Fig. 3, left) including a pyrometer for determining the sample temperature. In addition, a source for atomic oxygen has been added. The main advantage of the new heating system is that only the substrate is heated while the surrounding parts are hardly affected (Fig. 3, right). In this way one can achieve an essentially better vacuum at temperatures well above 1000°C. The achievable substrate temperature is limited by the melting point and the size of the substrate material (approx. 1410°C for a $5 \times 5 \text{ mm}^2$ silicon substrate). The laser heating system has already been successfully used for removing the amorphous silicon oxide layer from the surface of silicon substrates at 1150°C. This is required for the epitaxial growth of oxide thin films on this substrate.

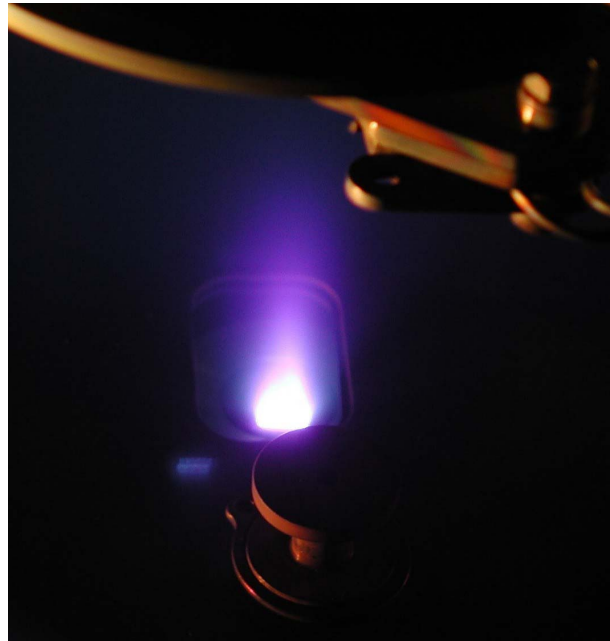


Figure 2: Pulsed Laser Deposition (PLD): When the pulse of the UV laser (KrF excimer laser, 248 nm) hits the target, the target material is ablated and the so-called laser “plume” containing highly excited atoms and molecules is formed.

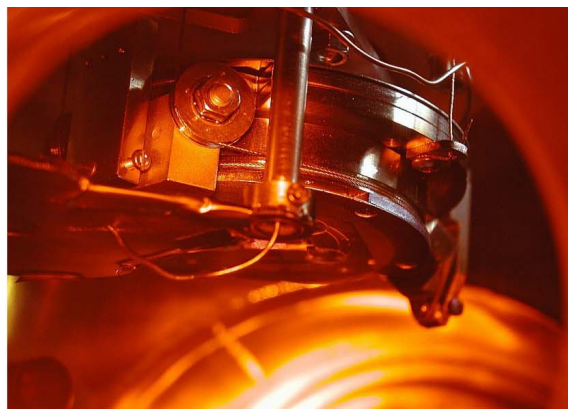
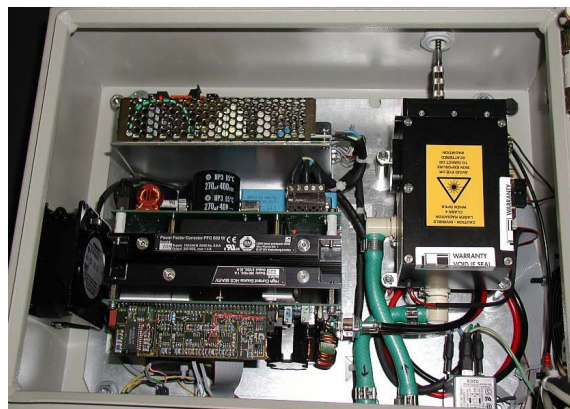


Figure 3: Components of the laser heating system: The substrate is heated using an IR diode laser head that is located in a separate box far away from the deposition chamber (left). The laser light is brought to the substrate (right) via an optical fiber.

Single Crystal Growth and Synthesis of Bulk Materials

Transition metal oxides are of great interest due to their various interesting physical properties (e.g. high temperature superconductivity, colossal magnetoresistance, ferroelectricity, nonlinear optical properties etc.) and their high potential for applications. The WMI operates a laboratory for the synthesis of bulk materials and single crystals including a four-mirror image furnace. With this furnace crystals of various high temperature superconducting materials or other transition metal oxides can be grown as single crystals using the traveling solvent floating zone technique. The furnace consists basically of 4 elliptical mirrors with a common focus on the sample rod and with halogen lamps in their other focus. By irradiation of the focused light the sample rod is locally heated and eventually molten. The molten zone can be moved up and down along the entire sample rod under simultaneous rotation. By repeated melting and crystallization of the sample seed selection takes place and the formerly polycrystalline rod is transformed into a single crystal. Single crystal growth can be performed with this furnace at maximum temperatures up to 2200°C in the pressure range from 10^{-5} mbar up to 10 bar and in oxidizing, reducing as well as inert atmosphere.



Figure 4: The four-mirror image furnace installed at the crystal laboratory of the WMI. Crystals can be grown by the floating zone and traveling solvent floating zone technique at temperatures up to 2200°C and pressures up to 10 bar.

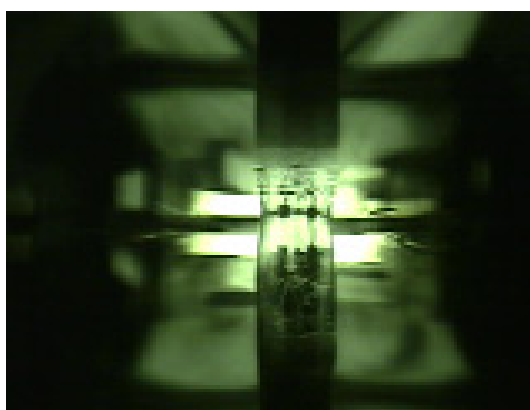
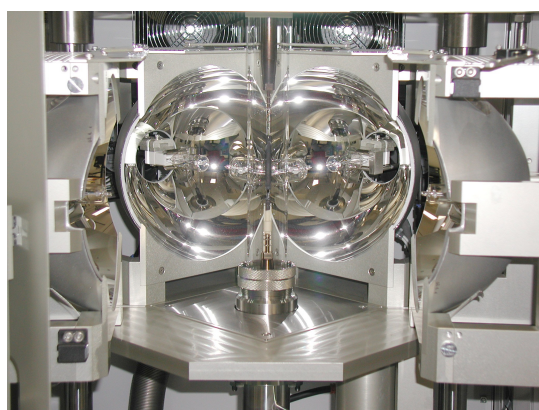


Figure 5: Left: Central part of the image furnace with the four elliptical mirrors. In the center one can see the quartz tube with the poly-crystalline rod. Right: View on the molten zone of cuprate superconductor obtained by a CCD camera.

The X-ray diffraction systems

For x-ray analysis the Walther-Meissner-Institute operates two X-ray diffractometers (Bruker D8 Advance and D8 Discover). The two-circle system is used for powder diffraction. In this system the samples can be heated in oxygen atmosphere up to 1600°C. It is equipped with a Göbel mirror and an area detector to save measuring time. The second system is a high resolution four-circle diffractometer that can be used for reciprocal space mappings. It is equipped with a Göbel mirror and an asymmetric two-fold monochromator and allows for the texture analysis of thin film superlattices and single crystalline materials. In both systems measurements can be carried out fully computer controlled.



Figure 6: The two-circle X-ray diffractometer Bruker D8 Advance.

Beyond these two Bruker x-ray systems a Laue camera for single crystal analysis and a Debye-Scherrer camera are available.

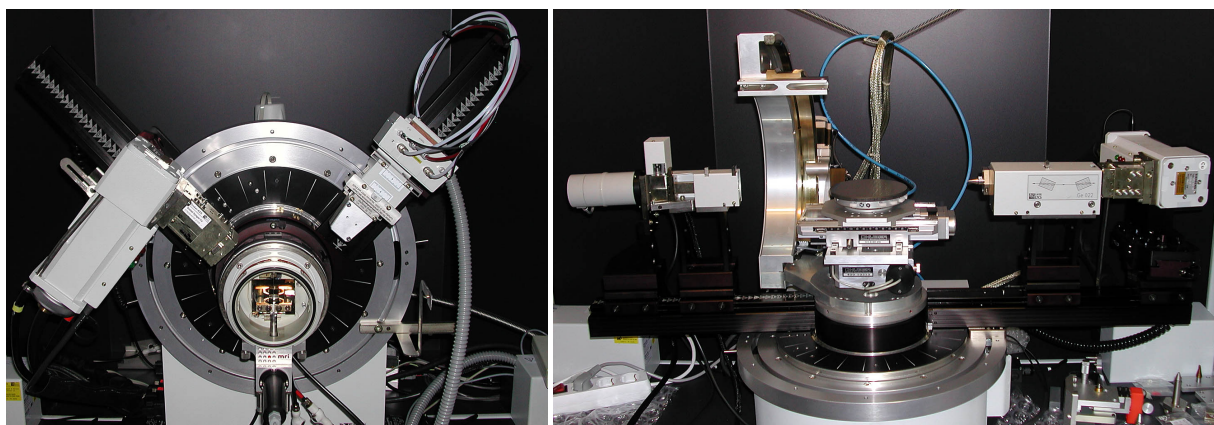


Figure 7: Left: High temperature sample holder of the D8 Advance system. Right: Four-circle high resolution X-ray diffractometer Bruker D8 Discover.



Figure 8: Quantum Design SQUID magnetometer.

The SQUID magnetometer is equipped with a superconducting solenoid allowing for a maximum field of 7 T. At present, the magnetometer is used for the characterization of magnetic materials (both in bulk and thin film form). Examples are the doped manganites, magnetite, the double perovskites or magnetic semiconductors.

The High Field Laboratory

Transport and thermodynamic properties of samples are often studied as a function of applied magnetic field. For such measurements several superconducting magnets are available at the WMI. Two of them (8/10 and 15/17 Tesla magnet system) are located in the high magnetic field laboratory in the basement of the WMI. The magnet systems are lowered below the ground level to facilitate the access to the top flange and the change of the sample sticks. The magnet systems are decoupled from the building to avoid noise due to mechanical vibrations. A variety of sample holders can be mounted allowing for e.g. sample rotation during the measurement. For standard sample holders the accessible temperature regime is $1.5 \text{ K} < T < 300 \text{ K}$. However, also $^3\text{He}/^4\text{He}$ dilution refrigerator inserts ($T > 20 \text{ mK}$) or high temperature units ($T < 700 \text{ K}$) can be mounted. All measurements are fully computer controlled (by the use of the LabView software tool) allowing for remote control and almost continuous measurements.



Figure 9: High field laboratory with Oxford 17 T magnet system.

The SQUID-magnetometer

For the analysis of the magnetic properties of materials, a Quantum Design SQUID magnetometer system as shown in Fig. 8 is used at the WMI. The SQUID magnetometer allows for measurements in the temperature regime from 1.5 to 400 K and provides excellent sensitivity particularly in the low field regime. Due to the excellent sensitivity of the system, thin film samples with a very small sample volume can be analyzed. In a special inset, samples can be measured up to temperatures well above room temperature (up to 700°C). For this option the sample volume has to be reduced.



The Clean Room Facility

For the fabrication of nanostructures and superconducting as well as spintronic devices the WMI operates a class 1000 clean room facility with an area of about 50 m². This clean room facility has been put into operation at the WMI within the year 2001. The clean room is subdivided into two parts for optical lithography and electron beam lithography, respectively. The clean room facility is equipped with the standard tools for optical lithography such as resist coaters, hot plates, wet benches, a Karl Süss MJB3 mask aligner and an optical projection lithography system. The technical infrastructure for the clean room is located in the basement of the WMI directly below the clean room area.



Figure 10: Top: Part of the clean room facility with optical lithography equipment and clean room benches. Bottom: Resist coater and hot plates.

Electron Beam Lithography

The Electron Beam Lithography System is installed in one part of the clean room facility. It consists of a Philips XL 30 SFEG scanning electron microscope (SEM) with a Raith Elphy Plus electron beam lithography system and a laser stage. The SEM is equipped with a hot field emitter and typically provides a beam diameter of less than 1.5 nm at ≥ 10 keV or about 2.5 nm at 1 keV. The lithography unit allows the fabrication of nanostructures down to about 10 nm. We have realized the controlled fabrication of metallic strip patterns with a strip width of about 20 nm. The electron beam lithography is used for the fabrication of nanostructures in metallic and oxide systems required for the study of quantum effects in mesoscopic samples.

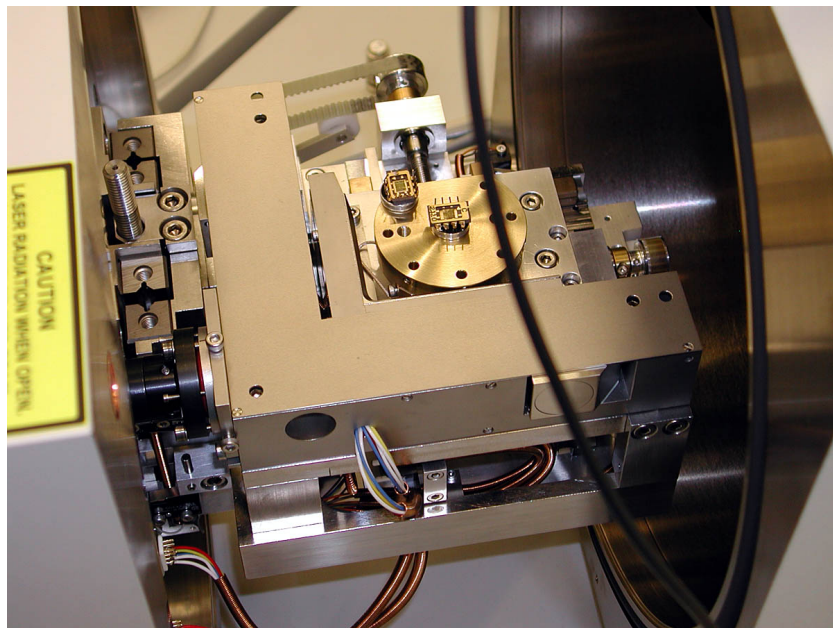
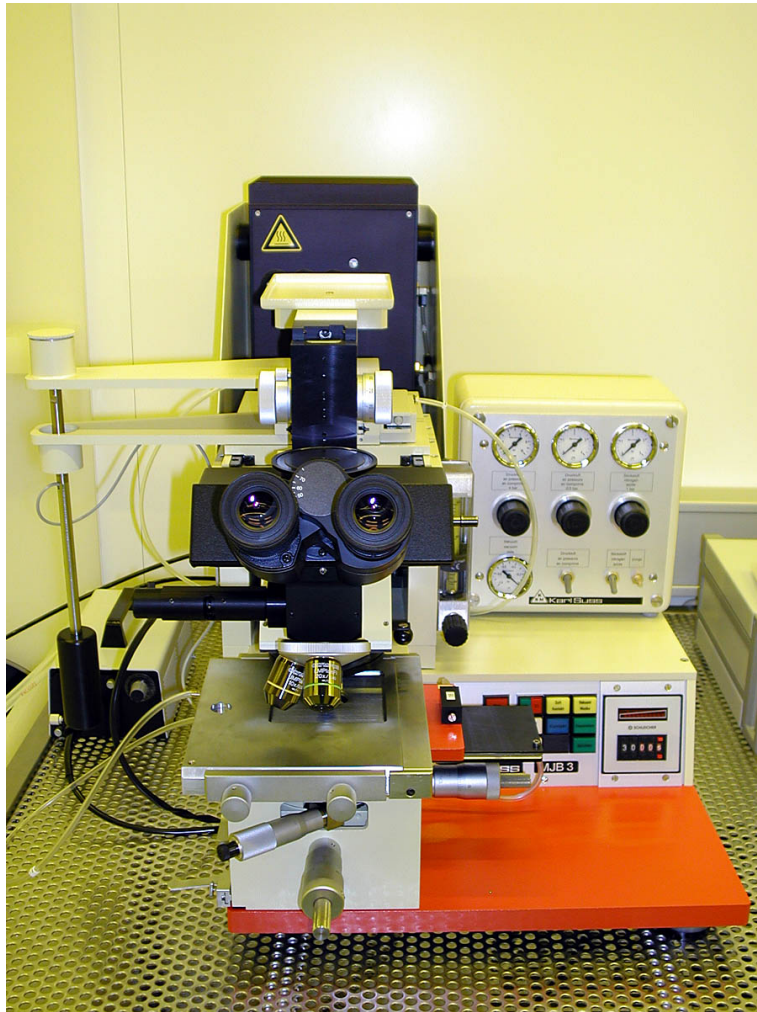


Figure 11: Top: Philips XL 30 SFEG Scanning Electron Microscope with Raith Elphy Plus Lithography System. Bottom: Raith Laser Stage.



Optical Lithography

For optical lithography a Karl Süss MJB 3 maskaligner or an optical microscope based projection system are used. The maskaligner is operating in the 1 : 1 soft or hard contact mode and is using chromium metal masks. In the projection system the mask pattern is demagnified by a factor of 5 to 100. Therefore, cheap foil masks can be used. With both systems microstructures with a lateral dimension down to $1\ \mu\text{m}$ can be fabricated.



Figure 12: Top: Süss MJB 3 maskaligner for optical lithography. Bottom: Optical projection lithography based on an optical microscope.

Low and Ultra-low Temperature Facilities

The Walther-Meissner-Institute operates several low and ultra-low temperature facilities that have been developed and fabricated in-house.

The lowest temperature is achieved by the nuclear demagnetization cryostat "Bayerische Millimühle 2". This ultra-low temperature facility consists of an in-house built dilution refrigerator and originally of two nuclear demagnetization stages. The first of those is based on a hyperfine enhanced van Vleck paramagnet PrNi_5 (0.9 mole), the second, which has been removed a few years ago, was based on purified copper (0.2 mole). The lowest temperature reached with this system was slightly below $30 \mu\text{K}$ in the copper nuclear spin system. At the moment, the first stage can be cooled to below $400 \mu\text{K}$ and, due to the large heat capacity of PrNi_5 , it stays below the mixing chamber temperature (5 mK) for nearly 3 weeks. In this cryostat three measuring sites are provided, two in a magnetic field compensated region and one in the center of an 8 T magnet. They are suitable for specific heat measurements, for capacitive torque- and SQUID magnetometry, as well as for transport measurements (electrical und thermal conductivity). The cryostat is also equipped with a pressure cell for liquid and solid ^3He , which at the moment is used for nuclear spin resonance measurements below 1 mK .



Figure 13: The dilution refrigerator and the nuclear demagnetization stage of the nuclear demagnetization cryostat "Bayerische Millimühle 2".



Figure 14: A “dry” millikelvin cooler: dilution refrigerator with pulse-tube pre-cooling developed at WMI.

Within the last years, the Walther-Meissner-Institute has developed a dilution refrigerator with pulse-tube pre-cooling. We denote such system as a “dry millikelvin cooler”, since it does no longer require liquid helium for precooling. In contrast, this ultra-low temperature system is pre-cooled using a pulse tube refrigerator. The system is under test at the moment and temperature below 10 mK have already been achieved at the mixing chamber.

We note that the pulse-tube refrigerator based precooling system cannot only be used for providing the base temperature of a dilution refrigerator but also for various other cryogenic systems. The dry systems are highly attractive for locations, where the supply with liquid helium is complicated and/or expensive. In future they even may displace standard liquid helium systems in low temperature laboratories. The system developed at the WMI is meanwhile commercialized by the VeriCold Technologies GmbH at Ismaning, Germany.

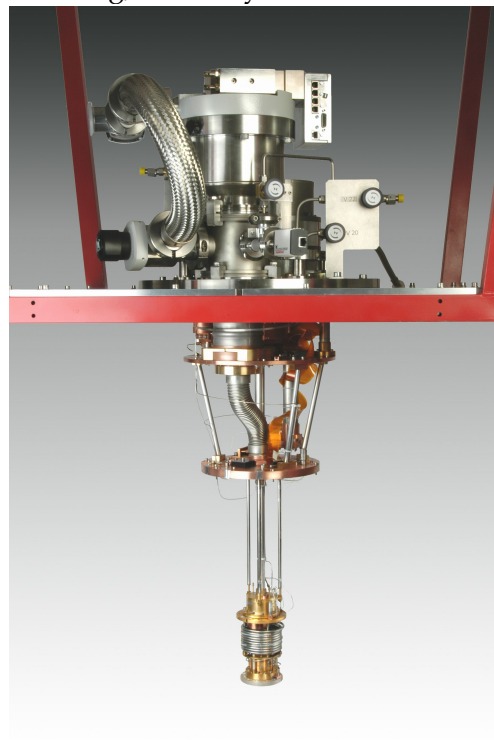
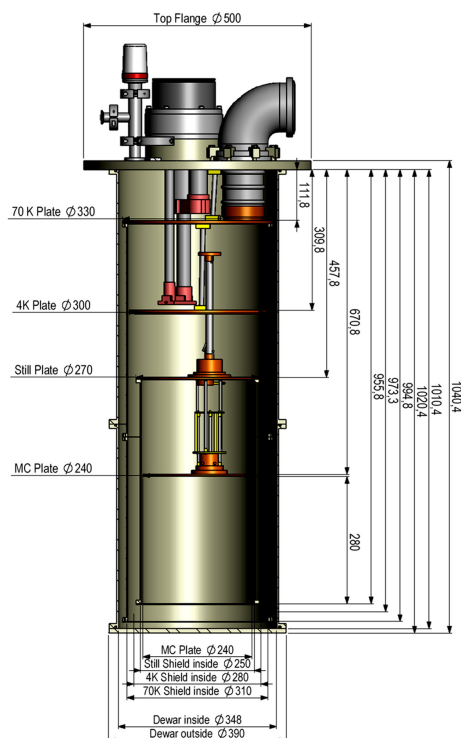


Figure 15: Cross-sectional view (left) and photograph (right) of the dry dilution refrigerator unit available at VeriCold Technologies GmbH.

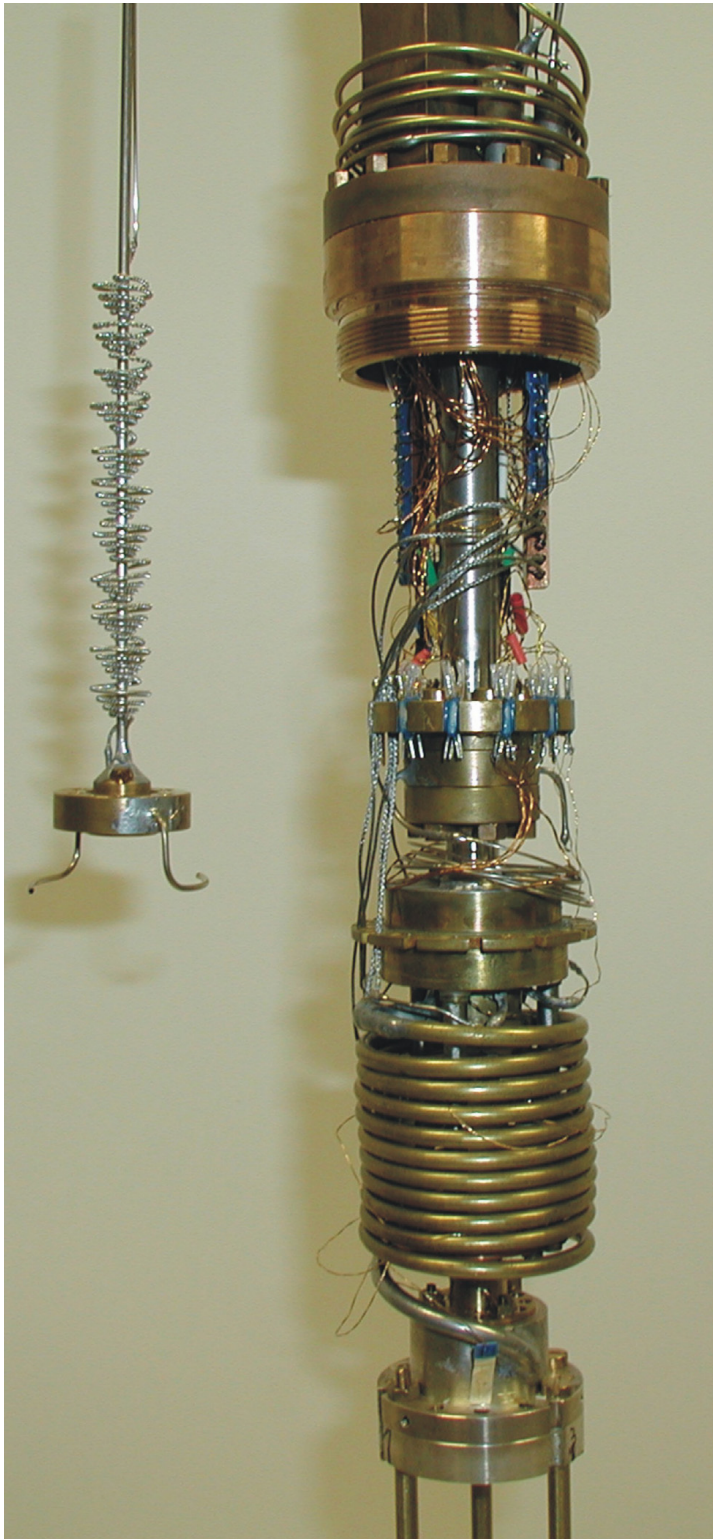


Figure 16: Dilution refrigerator insert with the Joule-Thomson stage, the heat exchanger and the mixing chamber.

The Walther-Meissner-Institute also develops and fabricates dilution refrigerator inserts for temperatures down to about 20 mK. The inserts fit into all cryogenic systems (e.g. superconducting magnets) having a two inch bore. They allow fast sample change and rapid cool down cycles of less than five hours.

The dilution refrigerator inserts are engineered and fabricated in-house and are also provided to other low temperature laboratories for ultra low temperature experiments.

New Network Infrastructure

The Walther-Meissner-Institute has a modern data network infrastructure. It was planned and installed in close cooperation with the Leibniz-Rechenzentrum and is based on fiber optic cables. About 270 double fiber optic lines with an average length of 50 m are installed in the WMI together with the corresponding number of data link sockets in all the labs and offices. In the basement of the institute, one room is hosting the central fiber optic network switch (see Fig. 17). There, the fibers coming from all rooms in the WMI meet together. The switch provides the data link between the nodes within the WMI as well as from the WMI to the internet. The structured concept of the new network consisting of single node-to-node connections leads to higher reliability and efficiency for the data transfer as compared to the former coaxial ring lines. With possible transfer rates up to 10 GBit/s per node the WMI fiber optic network is prepared for the coming generations of hardware and software.



Figure 17: In the basement of the WMI a new stacked switch providing 68 fiber optic connectors was installed to switch data packets within the WMI as well as from the WMI to the internet and vice versa.

Publications

1. RAMA N., RAO M.S. Ramachandra, SANKARANARAYANAN V., MAJEWSKI P., GEPRÄGS S., OPEL M., GROSS R.,
A-site-disorder-dependent percolative transport and Griffiths phase in doped manganites
Phys. Rev. B **70**, 224424 (2004).
2. GRAYSON M., HUBER M., ROTHER M., BIBERACHER W., WEGSCHEIDER W., BICHLER M., ABSTREITER G.,
Experimental demonstration of a sharp quantum Hall edge
Physica E **25**, 212-218 (2004).
3. CHANDRASEKHAR B.S.,
Magnetostriction
Encyclopedia of Physics, Wiley-VCH (2005).
4. MAJEWSKI P., GEPRÄGS S., BOGER A., OPEL M., ALFF L., GROSS R.,
Epitaxial growth of electron doped double perovskites $\text{La}_x\text{A}_{2-x}\text{CrWO}_6$ with A = Sr and Ca
J. Magn. Magn. Mat. **290-291**, 1154-1157 (2005).
5. NIELSEN K.-W., PHILIPP J.B., OPEL M., ERB A., SIMON J., ALFF L., GROSS R.,
Ferromagnetism in Mn-doped ZnO due to impurity bands
Superlattices and Microstructures **37**, 327-332 (2005).
6. RAMA N., OPEL M., SANKARANARAYANAN V., GROSS R., OGALE S.B., VENKATESAN T., RAO M.S. Ramachandra,
A-site dependent percolative thermopower and Griffiths phase in $\text{Pr}_{0.7-x}\text{Ho}_x\text{Sr}_{0.3}\text{MnO}_3$ ($x = 0.0, 0.04, 0.08$ and 0.1)
J. Appl. Phys. **97**, 10H713 (2005).
7. TASSINI L., VENTURINI F., ZHANG Q.-M., HACKL R., KIKUGAWA, N., FUJITA T.,
Dynamical Properties of Charged Stripes in $\text{La}_{2-x}\text{Sr}_x\text{CuO}_4$
Phys. Rev. Lett. **95**, 117002 (2005).
8. KARTSOVNIK M.V., PESCHANSKY V.G.,
Galvanomagnetic phenomena in layered organic conductors (Review)
Low Temp. Phys. **31**, 185-202 (2005).
9. FLACHBART K., GABÁNI S., GLOOS K., MEISSNER M., OPEL M., PADERNO Y., PAVLIK V., SAMUELY P., SCHUBERTH E., SHITSEVALOVA N., SIEMENSMEYER K., SZABÓ P.,
Low Temperature Properties and Superconductivity of LuB_{12}
J. Low Temp. Phys. **140**, 339-353 (2005).
10. MAJEWSKI P., GEPRÄGS S., BOGER A., OPEL M., ERB A., GROSS R., VAITHEESWARAN G., KANCHANA V., DELIN A., WILHELM F. ROGALEV A., ALFF L.,
Magnetic moments of W 5d in Ca_2CrWO_6 and Sr_2CrWO_6 double perovskites
Phys. Rev. B **72**, 132402 (2005).
11. MAJEWSKI P., GEPRÄGS S., SANGANAS O., OPEL M., GROSS R., WILHELM F., ROGALEV A., ALFF L.,
X-ray magnetic circular dichroism study of Re 5d magnetism in $\text{Sr}_2\text{CrReO}_6$
Appl. Phys. Lett. **87**, 202503 (2005).
12. ANDRES D., KARTSOVNIK M.V., BIBERACHER W., NEUMAIER K., SCHUBERTH E., MÜLLER H.,
Superconductivity in the charge-density-wave state of the organic metal α -(BEDT-TTF) $_2\text{KHg}(\text{SCN})_4$
Phys. Rev. B **72**, 174513 (2005).
13. HUBER M., GRAYSON M., ROTHER M., BIBERACHER W., WEGSCHEIDER W., ABSTREITER G.,
Structure of a Single Sharp Quantum Hall Edge Proped by Momentum-Resolved Tunneling
Phys. Rev. Lett. **94**, 016805 (2005).
14. BIBERACHER W.,
Shubnikov-de Haas and de Haas-van Alphen Techniques
Encyclopedia of Condensed Matter Physics, Elsevier (2005).
15. GÖNNENWEIN S.T.B., RUSSO S., MORPURGO A.F., KLAPWIJK T.M., VAN ROY W., DE BOECK J.,
Quantitative study of magnetotransport through a (Ga,Mn)As single ferromagnetic domain

- Phys. Rev. B **71**, 193306 (2005).
16. KEIZER R.S., GÖNNENWEIN S.T.B., VAN DIJK I., KLAPWIJK T.M., GUPTA A.,
Planar Hall Effect in CrO₂
Proceedings of the 24th International Conference on Low-Temperature Physics, (2005).
 17. HOUSECROFT C.E., HERMANN B.A., NEUBURGER M., SCHAFFNER S., SCHERER L.J.,
2,2':6',2''-Terpyridine-4'(1'H)-thione a missing link in metallosupramolecular chemistry
New J. Chem. **29**, 1475-1481 (2005).
 18. SCHERER L., MERZ L., CONSTABLE E.C., HOUSECROFT C., NEUBURGER M., HERMANN B.A.,
Conformational Analysis of Self-Organized Monolayers with Scanning Tunneling Microscopy at Near-Atomic Resolution
J. Am. Chem. Soc. **127**, 4033-4041 (2005).
 19. MERZ L., GÜNTHERODT H.-J., SCHERER L., CONSTABLE E.C., HOUSECROFT C., NEUBURGER M., HERMANN B.A.,
Octyl-Decorated Fréchet-Type Dendrons: A General Motif for Visualization of Static and Dynamic Behavior Using Scanning Tunneling Microscopy?
Chem. Eur. J. **11**, 2307-2318 (2005).
 20. HACKL R., TASSINI L., VENTURINI F., HARTINGER Ch., ERB A., KIKUGAWA N., FUJITA T.,
Ordering Phenomena in Cuprates
B. Kramer (Ed.): Adv. in Solid State Phys. **45**, 227-238 (2005).
 21. LYUBOVSKII R.B., PESOTSKII S.I., NIZHANKOVSKII V.I., BIBERACHER W., LYUBOVSKAYA R.N.,
De Haas-van Alphen oscillations in the organic quasi-two-dimensional metal (ET)₈Hg₄Cl₁₂(C₆H₅Cl)₂
J. Exp. Theor. Phys. **98**, 1037-1039 (2005).
 22. SCHUBERTH E.A., KATH M., TASSINI L., MILLAN-CHARCARTEQUI C.,
Magnetization Studies of the Nuclear Spin Ordered Phases of Solid ³He in Different Sinters
Eur. Phys. J. B **46**, 349 (2005).
 23. ESSELING M., MOSHNYAGA V., SAMWER K., MARX A., GROSS R.,
Low frequency 1/f-noise in LSMO:MgO nanocomposites films
Appl. Phys. Lett. **87**, 082509 (2005).
 24. LU Y., KLEIN J., HERBSTTRITT F., PHILIPP J.B., MARX A., ALFF L., GROSS R.,
Structure and Transport Properties of Coherently Strained La_{2/3}Ca_{1/3}MnO₃/SrTiO₃ Superlattices
Phys. stat. sol. (b) **242**, 1545-1560 (2005).
 25. REISINGER D., MAJEWSKI P., OPEL M., ALFF L., GROSS R.,
Hall effect, magnetization and conductivity of Fe₃O₄ epitaxial thin films
Appl. Phys. Lett. **85**, 4980 (2005).
 26. JIMÉNEZ DE HARO M.C., PÉREZ-RODRÍQUEZ J.L., POYATO J., PÉREZ-MAQUEDA L.A., RAMÍREZ-VALLE V., JUSTO A., LERF A., WAGNER F.E.,
Effect of ultrasound on preparation of porous materials from vermiculite
Appl. Clay Sci. **30**, 11-20 (2005).
 27. GROSS R.,
Grain Boundaries in High Temperature Superconductors: A Retrospective View
Physica C **432**, 105-115 (2005).
 28. EINZEL D., PARPIA J.M.,
Transport in Unconventional Superconductors: Application to Liquid ³He in Aerogel
Phys. Rev. B **73**, 1 (2006).
 29. MARIANTONI M., CHRIST H., OLIVER W.D., WILHELM F.K., EMMERT A., MARX A., GROSS R., STORCZ M.J., SOLANO E.,
Generation and Detection of Microwave Fock States: Linear Optics on a Chip
Phys. Rev. Lett., submitted for publication (2005).
 30. GEPRÄGS S., MAJEWSKI P., RITTER C., ALFF L., GROSS R.,
Electron doping in the double perovskite La_xA_{2-x}CrWO₆ with A=Sr and Ca
J. Appl. Phys., submitted for publication (2005).
 31. LU Y., KLEIN J., HERBSTTRITT F., PHILIPP J.B., MARX A., GROSS R.,

- Effect of strain and tetragonal lattice distortion in doped perovskite manganites**
Phys. Rev B, submitted for publication (2005).
32. WAGENKNECHT M., NACHTRAB T., EITEL H., PHILIPP J.B., GROSS R., KLEINER R., KOELLE D.,
Laser microscopy of tunneling magnetoresistance in manganite grain-boundary junctions
Phys. Rev. Lett., accepted for publication (2005).
33. SCHUBERTH E.A., KATH M., BAGO S.,
Magnetization Studies on the nuclear ordered phases of solid ^3He in Ag Sinters
J. Low Phys., accepted for publication (2005).
34. SCHUBERTH E.A.,
Magnetism in solid ^3He
Physica B, submitted for publication (2005).
35. KEIZER R.S., GÖNNENWEIN S.T.B., KLAPWIJK T.M., MIAO G., XIAO G., GUPTA A.,
Triplet supercurrent through the half-metallic ferromagnet CrO_2
Nature, accepted for publication (2005).
36. LERF A., BUCHSTEINER A., PIEPER J., SCHÖTTL S., DEKANY I., SZABO T., BOEHM H.P.,
Hydration Behaviour and Dynamics of Water Molecules in Graphite Oxide
J. Phys. Chem. Sol., in print(2005).
37. LERF A., ERB A., WAGNER F.E., POYATO J., PÉREZ-RODRÍQUEZ J.L., PÉREZ-RODRÍQUEZ L.A.,
Reduction reactions induced by heating in hydrazinium and ammonium vermiculites from Andalusia (Spain)
Phys. Chem. Miner., submitted for publication (2005).
38. HERMANN B.A., SCHERER L., CONSTABLE E.C., HOUSECROFT C.,
Self-Organized Monolayer- a Route to Conformational Switching and Read-Out of Supramolecular Assemblies
Adv. Funct. Mat., in print (2005).
39. HERMANN B.A.,
Self-Assembled Monolayers
Encyclopedia on Supramolecular Chemistry, in print (2005).
40. EINZEL D.,
Superfluids
Encyclopedia of Mathematical Physics, Elsevier, in print (2005).
41. DEVEREAUX T.P., HACKL R.,
Inelastic Light Scattering from Correlated Electrons
Rev. Mod. Phys., submitted for publication (2005).
42. HACKL R., TASSINI L., VENTURINI F., ERB A., HARTINGER CH., KIKUGAWA N., FUJITA T.,
Raman Study of Ordering Phenomena in Copper-Oxygen Systems
J. Phys. Chem. Solids, accepted for publication (2005).
43. KARTSOVNIK M.V., SIMONOV S., ANDRES D., BIBERACHER W., KUSHCH N., MÜLLER H., SHEIKIN I.,
Incoherent versus coherent interlayer transport in layered conductors under a magnetic field
J. Phys. IV France, in press (2005).
44. KARTSOVNIK M.V., ANDRES D., SIMONOV S.V., BIBERACHER W., SHEIKIN I., KUSHCH N.D., MÜLLER H.,
Angle-dependent magnetoresistance in the weakly incoherent interlayer transport regime
Phys. Rev. Lett., submitted for publication (2005).
45. KARTSOVNIK M.V., ANDRES D., BIBERACHER W.,
Hierarchy of the density-wave states and superconductivity in the organic conductor α -(BEDT-TTF) $_2\text{KHg}(\text{SCN})_4$
C.R. Chimie, submitted for publication (2005).
46. ZABOLOTNYY V.B., BORISENKO S.V., KORDYUK A.A., FINK J., GECK J., KOITZSCH A., KNUPFER M., BÜCHNER B., BERGER H., ERB A., LIN C.T., KEIMER B., FOLLATH R.,
Effect of Zn and Ni impurities on the quasiparticle renormalization in Bi-2212
Phys. Rev. Lett., accepted for publication (2005).

Theses, Appointments, Awards

Appointments

Priv.-Doz. Dr. habil. Erwin Schubert has been appointed apl.-Professor at the Technical University of Munich.

Completed and ongoing Ph.D. Theses

1. **Effects of high magnetic fields and hydrostatic pressure on the low temperature density wave state of the organic metal α -(BEDT-TTF)₂KHg(SCN)₄**
Dieter Andres, Februar 2005.
2. **Ferromagnetische Einzelladungstransistoren**
Jürgen Schuler, Mai 2005
3. **Symmetrie des Ordnungsparameters und Pseudogap-Verhalten in Hochtemperatur-Supraleitern**
Bettina Welter, seit August 2000.
4. **Herstellung und Charakterisierung von supraleitenden Quantenbits**
Frank Deppe, seit April 2002.
5. **Spininjektion in Halbleiter mit ferromagnetischen Oxiden**
Petra Majewski, seit November 2002.
6. **Raman scattering in materials with quantum phase transitions**
Leonardo Tassini, seit April 2003.
7. **Supraleitende Quantenbits mit π -Josephson-Kontakten für die Quanteninformationsverarbeitung**
Matteo Mariani, seit November 2003.
8. **Wachstum und Physik künstlicher magnetischer Heterostrukturen**
Karl Nielsen, seit Dezember 2003.
9. **Magnetisierungsmessungen an festem ³He bei ultratiefen Temperaturen**
Matthias Kath, seit April 2004.
10. **Kristallzüchtung und Charakterisierung von elektronendotierten Hochtemperatur-Supraleitern**
Michael Lambacher, seit September 2004.
11. **Supraleitende Quantenbits mit Supraleiter-Ferromagnet-Supraleiter Josephson-Kontakten**
Georg Wild, seit Oktober 2004.
12. **Spin-Engineering in funktionalen Schichtsystemen aus Übergangsmetalloxiden**
Stephan Geprägs, seit Oktober 2004.
13. **Herstellung und Charakterisierung von supraleitenden Nanostrukturen für die Realisierung von Quantenbits**
Tobias Heimbeck, seit November 2004.
14. **Untersuchung der Wechselwirkungspotenziale in Kupratsupraleitern durch quantitativen Vergleich spektroskopischer Resultate**
Wolfgang Prestel, seit November 2004.
15. **Entwicklung von Verfahren zur Manipulation und zum Auslesen supraleitender Quantenbits**
Karl Madek, seit März 2005.
16. **Tunnelkontakte und Spininjektoren auf der Basis von ferromagnetischen Übergangsmetalloxiden**
Andrea Boger, seit März 2005.

Completed and ongoing Diploma, Bachelor, Master Theses

1. **Untersuchung der Zustandsquantisierung in Josephson-Kontakten**
Karl Madek, Februar 2005.
2. **Herstellung eines Fluss-Qubits**
Markus Tober, Februar 2005.
3. **Determination of Thermal Contact Resistance Depending on the Different Parameters in Experiment and Validation of the Results in a Simulation**
Arne Laucht, Mai 2005.
4. **Kobalt-dotiertes Zinkoxid**
Maike Lübbe, August 2005.
5. **Elektronen-Dotierung in epitaktischen dünnen Schichten aus $\text{La}_x\text{Sr}_{2-x}\text{CrWO}_6$**
Robert Geißler, August 2005.
6. **A Growth Study of Silicon Nanowires by Chemical Vapor Deposition**
Emma Peters, Oktober 2005.
7. **Thermal Stratification of a Liquid Hydrogen Vessel**
Sascha Gasser, November 2005.
8. **Investigation of Spectroscopic Ellipsometry for the Characterization of Electrochemically Produced Nanostructured Technical Layers for Microelectronics Packaging Applications**
Jan Perlich, November 2005.
9. **Annealing and Characterization of High- T_c Single Crystals**
Manwan Abbas, November 2005.
10. **Geometrieabhängigkeit des TMR-Effekts in Tunnelkontakten aus Magnetit**
Edwin Menzel, Dezember 2005.
11. **Untersuchung der magnetischen Wechselwirkung von Strontium-basierten Doppelperowskiten**
Oliver Sanganas, Dezember 2005.
12. **Makroskopische Quantenphänomene in supraleitenden Tunnelkontakten**
Renke Stolle, seit Dezember 2004.
13. **Herstellung von π -Josephson-Kontakten mit Supraleiter/Ferromagnet/Supraleiter Schichtsystemen**
Bernhard Huber, seit Dezember 2004.
14. **Mikrowellenspektroskopie an ultrakleinen Josephson-Kontakten**
Sven Beutner, seit Dezember 2004.
15. **Circuit Quantum Electrodynamics with Superconducting Flux Qubits**
Andreas Emmert, seit Januar 2005.
16. **Novel room temperature ferromagnetic semiconductors: preparation and characterization of bulk and thin film samples**
Amilcar Bedoya Pinto, seit Februar 2005.
17. **Herstellung und Charakterisierung von supraleitenden Phasen-Qubits**
Martin Göppl, seit Mai 2005.
18. **Superconducting Microwave Circuits for Quantum Experiments**
Thomas Niemczyk, seit Mai 2005.
19. **Raumtemperatur-Ferromagnetismus und Magnetotransport in Kobalt-dotiertem ZnO**
Sebastian Bauer, seit Juni 2005.
20. **Wachstum und Charakterisierung epitaktischer Schichten aus Chromdioxid**
Sebastian Schink, seit September 2005.
21. **Magnetische Anisotropie in dünnen Schichten aus Magnetit**
Andreas Brandlmaier, seit Oktober 2005.

22. **Charakterisierung verschiedener Feuchtesensoren für den Einsatz auf dem hochfliegenden Forschungsflugzeug HALO**
Ingmar Mayerbuch, seit November 2005.
23. **Neutronenstreuung an Kupratsupraleitern**
Markus Bröll, seit November 2005.
24. **Single Microwave Photon Detection Using Hybrid Rings**
Ferhat Katmis, seit Dezember 2005.
25. **Spinabhängiger Transport in Magnetit**
Wolfgang Kaiser, seit Dezember 2005.
26. **Transport und Ramanstreuung in unkonventionellen Supraleitern**
Ludwig Klam, seit Dezember 2005.
27. **Fabrication and Characterization of Superconducting Flux Qubits in Well-defined Electromagnetic Environment**
Sonja Dandl, seit Dezember 2005.
28. **Herstellung und Strukturierung von nanomagnetischen Schichten mittels Nanoimprintlithographie**
Norman Augst, seit Dezember 2005.

Research Projects and Cooperations

Many of our research projects have benefited from the collaboration with external groups via joint research projects, individual collaborations, exchange programs and visitors. Several collaborations are based on joint projects which are financially supported by different organizations (see list below). A large number of collaborations also exists with several universities and other research institutions without direct financial support. These are also listed below.

Funded Projects

Deutsche Forschungsgemeinschaft: Sonderforschungsbereiche

Sonderforschungsbereich 631: Festkörperbasierte Quanteninformationsverarbeitung: Physikalische Konzepte und Materialaspekte

1. Teilprojekt A3/A4: Supraleitende Bauelemente mit π -Kontakten als Grundelemente für Quanteninformationssysteme
Gross, Alff, Marx
2. Teilprojekt C5: Spinabhängiger Transport in nanostrukturierten Festkörpern
Marx, Gross, Opel
3. Teilprojekt S: Verwaltung des Sonderforschungsbereichs
Gross

Deutsche Forschungsgemeinschaft: Forschergruppen

Forschergruppe 538: Dotierungsabhängigkeit von Phasenübergängen und Ordnungsphänomenen in Kupratsupraleitern

1. Teilprojekt: Einkristallzüchtung von p- und n-dotierten Kupratsupraleitern
A. Erb, R. Gross
2. Teilprojekt: Raman-Untersuchungen zu konkurrierenden Ordnungsphänomenen in Kupraten
R. Hackl, R. Gross
3. Sprecherprojekt
R. Hackl

Deutsche Forschungsgemeinschaft – Normalverfahren

1. Kristalline organische Metalle und Supraleiter: Synthese und elektronische Eigenschaften,
gefördert von der DFG und der russischen Stiftung für Grundlagenforschung (RFFI)
(W. Biberacher, WMI, und N. Kushch, Institut für Probleme der chemischen Physik, Cernogolovka, Az.: 436 RUS 113/592/0)

2. Neue funktionale Schichtsysteme auf der Basis künstlicher heteroepitaktischer Mehrlagenstrukturen aus Übergangsmetalloxiden
im Rahmen des Schwerpunktprogramms 1157 *Integrierte elektrokeramische Funktionsstrukturen*
(R. Gross, Az. GR 1132/13-1)
3. Entwicklung eines hochgenauen Rotationsensors mit superfluidem ^3He als Arbeitsmedium
(E. Schuberth, Az. Schu 450/4-1+2)

Bundesminister für Bildung, Wissenschaft, Forschung und Technologie (BMBF)

1. Verbundprojekt: Spinelektronik und Spinoptoelektronik in Halbleitern
Teilprojekt: Ferromagnetische metallische Oxide mit hoher Spinpolarisation für die Spinelektronik
(R. Gross, Förderkennzeichen: 13N8279)
Partners: Universities of Würzburg, Hamburg, Regensburg, Hannover and Marburg, Max-Planck-Institute Halle, Siemens AG, Infineon Technologies, Aixtron GmbH.

European Union

1. European Science Foundation Network "*Thin Films for Novel Oxide Devices: THIOX*"
(R. Gross; coordination: Prof. D. Blank, University of Twente, The Netherlands)
partners: several European Universities and research facilities.
2. Research and Training of Young Researchers on the "*Magnetic Properties of ^3He by Means of Neutron Diffraction*"
(E. Schuberth; coordination: Dr. Konrad Siemensmeyer, Hahn-Meitner Institute Berlin GmbH)
European Community, Contract No.: HPRN-CT-2000-00166
Partners: Hahn-Meitner Institut, Berlin, Univ. of Florida, Royal Holloway College, London, Univ. Liverpool, CNRS, Grenoble and Univ. Paris, Saclay.
3. ERA-Chemistry-network: *Hierarchically organized chemical structures: from molecules to hybrid materials*, project: *Probing Hierarchical Self-Assemblies Relevant for Drug and Vaccine Design by Employing STM*
(B. Hermann, project number ERA HE 5162/1-1)

Alexander von Humboldt Stiftung

1. Humboldt Forschungsstipendium "*Devereaux*"
(R. Hackl, Förderkennzeichen IV-USA/109800 6 STP)
2. Humboldt Forschungspreis "*Di Castro*"
(R. Hackl, Förderkennzeichen IV-ITA/111548 6 GSA)

Ministerio de Educacion y Ciencia, Spanien

1. Intercalación de minerales de la arcilla por medio de tratamiento con ultrasonidos y reacciones de transferencia de electrones. Producción de arcillas funcionalizadas con estructuras complejas jerarquizadas en el espacio interlaminar.
(J.L. Perez-Rodriguez, A. Lerf, Reference No. : MAT2005-04838)

INTAS

1. Magnetic quantum oscillations in layered organic superconductors
(W. Biberacher, M. Kartsovnik, Förderkennzeichen INTAS 01-0791)

IDK-NBT

1. STM on magnetic layers and self-organized magnetic molecules
(B. Hermann, head: C. Bräuchle, J. Rädler, IDK-NBT 1506-42501-1).

Research Equipment financed via HBFEG

1. Helium Liquefaction System, Linde TCF 20
(R. Gross, reference No.: HBFEG-163-957)
2. Reactive Ion Etching System
(R. Gross, reference No.: HBFEG-163-1009)

Conferences and Workshops

The Walther-Meißner-Institute has organized/co-organized the following conferences and workshops in 2005:

1. *Workshop on Ordering Phenomena in Cuprate Superconductors II*
May 2-3, 2005, Dresden, Germany.
2. *Workshop on the Properties of Cuprate Superconductors*
November 7-11, 2005, Ringberg Castle, Rottach-Egern, Germany

Collaborations

Other collaborations without direct project funding involve:

- University of Waterloo, Department of Physics, Ontario, Canada (Prof. Dr. T.P. Dev-
ereaux)
- NTT Basic Research Laboratories, Japan (Prof. Dr. H. Takayanagi)
- Tokyo Institute of Technology, Japan (Prof. K. Koinuma)
- Materials Physics Laboratory, Helsinki University of Technology, Finland (Dr. Tero
Heikkilä)
- Department of Condensed Matter Physics, The Weizmann Institute of Science, Israel (Dr.
Moshe Schechter)
- Instituto de Ciencia de Materiales de Sevilla, Spain (Prof. J. Poyato, Prof. J.L. Perez-
Rodriguez)
- Chalmers University of Technology, Gothenburg, Sweden (Prof. Dr. P. Delsing)
- Hungarian Academy of Sciences, Budapest University of Technology and Economics Bu-
dapest, Hungary (Prof. Dr. K. Kamaras, Dr. Attila Virosztek, Prof. Dr. A. Zawadowski)
- University of Basel, Institute of Inorganic Chemistry, Switzerland (Prof. E. Constable,
Prof. C. Housecroft)
- Royal Holloway University, London, UK (Prof. J. Saunders)
- University of Liverpool, UK (Dr. J. Goff)
- CNRS Grenoble, France (Prof. H. Godfrin)
- University of Florida, USA (Prof. D. Adams, Prof. Y. Takano)
- Materials Science Research Centre, IIT Madras, India (Prof. M.S. Ramachandra Rao)
- Cryomech, Inc. N.Y., USA (Dr. Ch. Wang)
- Vericold Technologies, Ismaning, Germany (Dr. J. Höhne, Dr. M. Bühler)
- University of Bonn, Germany (Prof. W. Mader)
- University of Leipzig, Germany (Dr. H. Schmidt)
- HMI Berlin, Germany (Dr. A. Buchsteiner, Dr. J. Pieper, Dr. K. Siemensmeyer)
- IFW Dresden, Germany (Prof. B. Büchner, Prof. J. Fink, Dr. S. V. Borisenko, Dr. M.
Knupfer)
- LMU Munich, Germany (Prof. Kotthaus, Prof. von Delft, Dr. F. Wilhelm)
- University of Tübingen, Germany (Prof. R. Kleiner, Prof. D. Kölle)
- University of Würzburg, Germany (Prof. W. Hanke, Prof. L. Molenkamp)
- University of Augsburg, Germany (Prof. Dr. P. Hänggi)
- Walter-Schottky-Institut, Garching, Germany (Prof. G. Abstreiter, Dr. M. Brandt)
- University of Hamburg, Germany (Dr. D. Grundler, Dr. G. Meier)
- Anorganic Chemistry, TU Munich, Germany (Prof. T. Fässler)
- Institute for Experimental Physics, Slovakian Academy of Sciences, Kosice, Slovakia
(Prof. K. Flachbart)
- High-Magnetic-Field Laboratory, Grenoble, France (Dr. I. Sheikin)
- B. Verkin Institute for Low Temperature Research and Engineering, Kharkov, Ukraine
(Prof. V.G. Peschansky)
- Landau Institute for Theoretical Physics, Chernogolovka, Russia (Dr. P. Grigoriev)

Stays abroad

Extended visits of members of the Walther-Meissner-Institute at foreign research laboratories:

1. **Rudolf Hackl**
University of Waterloo, Canada (Prof. T.P. Devereaux)
05. 04. – 24. 04. 2005
2. **Rudolf Hackl**
University of Rome (Prof. Carlo Di Castro) Rom, Italien
08. 05. - 11. 05. 2005
3. **Rudolf Hackl**
Hungarian Academy of Sciences, Research Institute for Solid State Physics (Prof. I. Tüttö),
Budapest, Ungarn
15. 12. – 19. 12. 2005
4. **Rudolf Hackl**
Budapest University of Technology and Economics and Research Institute for Solid State
Physics and Optics (Profs. I. Tüttö, A. Viroztek, A. Zawadowski, A. Janossy), Budapest,
Ungarn
26. 05. – 01. 06. 2005
5. **Anton Lerf**
Universidad de Malaga, Spanien (Prof. J.L. Perez-Rodriguez, Prof. J. Poyato)
13. 03. – 23. 03. 2005
6. **Mark Kartsovnik, Werner Biberacher**
High Magnetic Field Laboratory, Grenoble, France
29. 05. – 06. 06. 2005
7. **Mark Kartsovnik, Dieter Andres**
High Magnetic Field Laboratory, Grenoble, France
03. 07. – 10. 07. 2005
8. **Mark Kartsovnik**
Institute of Problems of Chemical Physics, Chernogolovka, Russia
23. 12. – 30. 12. 2005
9. **Petra Majewski**
ESRF, Grenoble, France
14. 06. – 21. 06. 2005
10. **Bianca Hermann**
University of Basel, Institute of Physics (Prof. E.C. Constable and Prof. H.-J. Güntherodt),
Basel, Switzerland
01. – 02. 02. 2005, 14. – 17. 02. 2005, 02. – 03. 11. 2005
11. **Matteo Mariani**
Massachusetts Institute of Technology (MIT), USA
04. 03. – 20. 03. 2005

Conference Talks and Seminar Lectures

Werner Biberacher

1. **Electronic Properties of Layered Organic Metals Studied by Magnetotransport and Magnetic Torque**
13. – 14. 06. 2005
Symposium "Science in High Magnetic Fields", Grenoble, France.
2. **Kristalline organische Metalle in hohen Magnetfeldern**
31. 10. 2005
Seminar des Sonderforschungsbereichs "Elektroaktive Stoffe", TU Graz, Austria.

B.S. Chandrasekhar

1. **Low Temperature Physics and Physicists 50 years ago**
27. 10. 2005
Syracuse University, Syracuse, USA.
2. **Low Temperature Physics and Physicists 50 years ago**
27. 05. 2005
Bruker Biospia R&D Center, Fällanden, Switzerland.

Andreas Erb

1. **Crystal growth of the high temperature superconductors within the Research Unit FG538**
23. 06. 2005
DPMC University of Geneva, Switzerland.

Sebastian Gönnerwein

1. **Hydrogen-control of ferromagnetism in the ferromagnetic semiconductor $\text{Ga}_{1-x}\text{Mn}_x\text{As}$**
28. 07. 2005
International Conference on Defects in Semiconductors, Awaji Island, Japan.
2. **Anisotropic magnetoresistance and long-range proximity effect in single ferromagnetic domains**
09. 12. 2005
Forschergruppenseminar Ferromagnet-Halbleiter-Nanostrukturen, Universität Regensburg, Germany.

Rudolf Gross

1. **Spin Electronics Based on Half-Metals**
18. 01. 2005
Van der Waals – Zeeman Colloquium, University of Amsterdam, Amsterdam, The Netherlands.

2. **From Electronics to Spintronics**
R. Gross
GMM-Workshop on “Devices after CMOS”
June 16 – 17, 2005, Munich, Germany.
3. **Metallische Nanostrukturen**
29. 06. 2005
Nanotechnologie-Seminar der Carl-Cranz-Gesellschaft e.V., Oberpfaffenhofen, Germany.
4. **Ferromagnetic Transition Metal Oxides for Spin Electronics**
R. Gross
SPIE Conference on “Correlated Electron Materials: Physics and Nanoengineering”
July 31 – August 4, 2005, San Diego, USA.
5. **From Flux Quantization to Superconducting Quantum Bits**
R. Gross
International Conference on “Advances in Physics and Astronomy of the 21st Century”
September 06 – 11, 2005, Varna, Bulgaria.
6. **Spinelektronik: Konzepte, Materialien und Zukunftsperspektiven**
14. 11. 2005
Seminar des Arbeitskreises Mikroelektronik, Mikro- und Feinwerktechnik des VDE/VDI,
München.
7. **Magnetic Oxide Thin Film Heterostructures for Spin Electronics**
THIOX Workshop on “Oxides at the Nanoscale”
November 17–18, 2005, Zaragoza, Spain.
8. **Superconducting Qubits: From Flux Quantization to Linear Optics on a Chip**
24. 11. 2005
Kolloquium des SFB/TR 21 “Control of quantum correlations in tailored matter: Common perspectives of mesoscopic systems and quantum gases”, Universität Tübingen.
9. **Supraleitende Quantenbits: Von der Flussquantisierung zur Quanteninformationsverarbeitung**
09. 12. 2005
Bavarian Academy of Sciences, Munich, Germany.

Rudolf Hackl

1. **Ordering phenomena in the cuprates: a Raman scattering point of view**
08. 09. 2005
University of British Columbia, Canada.
2. **Ordering phenomena in the cuprates: a Raman scattering point of view**
21. 10. 2005
University of Dortmund, Germany.
3. **Scaling behavior of electronic properties in normal and superconducting cuprates**
13. 04. 2005
University of Waterloo, Canada.

4. Cuprate Superconductors: Old Puzzles – New Developments

03. 02. 2005

University of Marburg, Germany.

5. Ordering phenomena and electron renormalization in the cuprates

06. – 11. 11. 2005

International Workshop of the Max-Planck-Institute for Solid State Research, Stuttgart, and the DFG Research Unit "Hochtemperatur-Supraleitung", Schloss Ringberg, Germany.

6. Comparison of ARPES, Infrared and Raman spectra

02. – 03. 05. 2005

Workshop der DFG Research Unit "Hochtemperatur-Supraleitung", Dresden, Germany.

7. Ordering Phenomena in Cuprates

04. – 09. 03. 2005

Spring Meeting of the German Physical Society, Berlin, Germany.

Bianca Hermann**1. Dynamic Reorganization and Conformational Diversity in Molecular Monolayers Investigated with STM**

19. 01. 2005

Max-Planck-Institute for Solid State Research, Stuttgart, Germany.

2. Static and Dynamic Self-Organization of Dendron Monolayers on Graphite Monitored with Scanning Tunneling Microscopy

09. 03. 2005

Spring Meeting of the German Physical Society, Berlin, Germany.

3. Self-Organizing Molecules – A Bottom-Up Approach to Functional Surfaces

09. 05. 2005

Physics Colloquium of the TUM and LMU, Munich, Germany.

4. Self-Organized Monolayers - A Route for Switching and Read-out of Functional Surfaces by Scanning Probe Methods

18. 06. 2005

Supramolecular Functional Materials Symposium, Murten, Switzerland.

Mark Kartsovnik**1. Incoherent versus coherent interlayer transport in layered conductors under a magnetic field**

21. – 27. 08. 2005

International Workshop on Electronic Crystals, ECRYS-2005, Cargese, Corsica.

2. Breakdown of the interlayer coherence as seen in the magnetotransport

11. – 16. 09. 2005

VIth International Symposium on Crystalline Organic Metal, Superconductors and Magnets, ISCOM'2005, Key West, Florida, USA.

3. **Hierarchy of the density-wave states and superconductivity in the organic conductors α -(BEDT-TTF)₂MHg(SCN)₄**
17. – 19. 10. 2005
International Symposium on Spin- and Charge-Correlations in Molecule-Based Materials, Königstein, Germany.
4. **Angle-dependent magnetoresistance in extremely anisotropic layered conductors: incoherent versus coherent interlayer transport regimes**
27. 12. 2005
Seminar at the Institute of Problems of Chemical Physics, Chernogolovka, Russia.

Anton Lerf

1. **Intercalation and electron transfer in layered host materials**
14. 03. 2005
Universidad de Malaga, Spain.
2. **Hydration behaviour and dynamics of water in Graphite Oxide**
06. – 09. 06. 2005
13th International Symposium on Intercalation Chemistry, Clermont-Ferrand, France.

Petra Majewski

1. **Probing the magnetic moment of W in the double perovskite Sr₂CrWO₆**
04. 10. 2005
12th International Workshop on Oxide Electronics, Cape Cod, USA.

Matteo Mariani

1. **The Persistent-Current Qubit in a Microwave Cavity**
15. 01. 2005
Kommissionssitzung, Walther-Meißner-Institute, Germany.
2. **Cavity-QED with Superconducting Flux Qubits**
09. 03. 2005
Massachusetts Institute of Technology (MIT), USA.
3. **Generation of Microwave Single Photons and Homodyne Tomography on a Chip**
17. 10. 2005
Group Seminar, Prof. Kotthaus, LMU Munich, Germany.

Achim Marx

1. **Superconducting Flux Qubits and Cavity QED**
05. 10. 2005
UT-TUM Bilateral Symposium on Nanosciences, University of Tokyo, Japan.

Matthias Opel

1. **Large Room Temperature TMR Effect in Tunnel Junctions Based on Magnetite**
18. 05. 2005
THIOX, 2nd Topical Meeting, Santa Margherita Ligure, Italy.

2. **Large Room Temperature TMR Effect in Tunnel Junctions Based on Magnetite**
08. 06. 2005
International Workshop on Integrated Electroceramic Functional Structures, Berchtesgaden, Germany.
3. **Ferromagnetische metallische Oxide mit hoher Spinpolarisation**
14. 06. 2005
Abschlusstreffen BMBF-Verbundprojekt 13N8279, Marburg, Germany.
4. **Large Room Temperature TMR Effect in Tunnel Junctions Based on Magnetite**
02. 11. 2005
50th Conference on Magnetism and Magnetic Materials, San Jose, California, USA.

Kurt Uhlig

1. **Cryogen-free dilution refrigerator precooled by a pulse-tube refrigerator with non-magnetic regenerator**
29. 08. – 02. 09. 2005
Cryogenic Engineering Conference and International Cryogenic Materials Conference, Keystone, Colorado, USA.

Seminars, Courses, Lectures and other Scientific Activities

The WMI Seminars

The Friday Seminar — Walther-Meissner-Seminar on Current Topics in Low Temperature Physics

1. **Effects of high magnetic fields on the charge-density wave conductor α -(BEDT-TTF)₂KHg(SCN)₄**
Dieter Andres, Walther-Meissner-Institut
21. 01. 2005
2. **Oxidische Dünnschichtsysteme bis in atomare Dimensionen: Analysemöglichkeiten der modernen Transmissionselektronenmikroskopie**
Jürgen Simon, Universität Bonn
28. 01. 2005
3. **Supramolekulare Nanomagnete: Quantenphysik im mesoskopischen Grenzbereich**
Dr. Oliver Waldmann, Department of Chemistry and Biochemistry, University of Bern
04. 02. 2005
4. **Deterministic optical Fock space generation**
Dr. Kenneth R. Brown, Center for Bits and Atoms, Department of Physics, Cambridge, USA
11. 02. 2005
5. **Quantum physics with quantum dots**
Prof. Klaus Ensslin, ETH Zürich, Schweiz
15. 04. 2005
6. **Electronic structure and magnetic properties of transition metal oxides**
Dr. G.S. Veittheswaran, Max-Planck-Institut für Festkörperforschung, Stuttgart
22. 04. 2005
7. **Origin of the resistive transition broadening for superconducting magnesium diboride**
Prof. A.S. Sidorenko, Institute of Applied Physics, Kishinev, Moldova
29. 04. 2005
8. **Wissenschaftliches Präsentieren - wie man einen guten Vortrag hält**
Dr. habil. Claus Ascheron, Executive Editor Physics, Springer-Verlag, Heidelberg
13. 05. 2005
9. **Deep insights into magnetism on a nanometer scale**
Prof. Josef Zweck, Universität Regensburg
20. 05. 2005
10. **Experimentelle Untersuchung der internen Reformierung in einer SOFC**
Claus Huber, Lehrstuhl für Thermodynamic, TU München
23. 05. 2005
11. **Dynamik und Reaktivität molekularer Adsorbate an Metalloberflächen**
Dr. Ludwig Bartels, Pierce Hall, University of California at Riverside, USA
20. 06. 2005
12. **Energetik und Dynamik 1-, 2- und 3-dimensionaler Strukturen an Grenzflächen**
Dr. Margareta Giesen, Institut für Biologische Schichten, Forschungszentrum Jülich
23. 06. 2005
13. **Formation and site-control of strain-driven nanostructures**
Dr. Oliver Schmidt, Max-Planck-Institut für Festkörperforschung, Stuttgart
23. 06. 2005
14. **Self-Assembled Monolayers: From Wishful Thinking of Reality**
Dr. Manfred Buck, EaStChem School of Chemistry, University of St. Andrews, UK
24. 06. 2005
15. **Elektronische Eigenschaften molekularer Festkörper - kohärente Festkörper oder nur viele Moleküle**
Dr. Martin Knupfer, Leibniz-Institut für Festkörper- und Werkstoffforschung, Dresden
24. 06. 2005

16. **Organische Moleküle zur Oberflächenfunktionalisierung und Herstellung von Halbleiterbauelementen**
Dr. Thorsten Kampen, Fritz-Haber-Institut der Max-Planck-Gesellschaft, Berlin
24. 06. 2005
17. **Grenzflächen-modifizierte organische Dünnschichten**
Prof. Rainer Fink, Lehrstuhl für Physikalische Chemie II, Universität Erlangen-Nürnberg
27. 06. 2005
18. **Supramolecular Architecture at Surfaces**
Dr. Johannes Barth, Advanced Materials and Process Engineering Laboratory, University of British Columbia, Canada
27. 06. 2005
19. **Understanding materials and high- T_c superconductivity**
Prof. Tom Devereaux, University of Waterloo, Canada
08. 07. 2005
20. **Double-exchange systems with general angular momentum j**
Dr. Randy Fishman, Condensed Matter Sciences Division Oak Ridge National Laboratory, USA
11. 07. 2005
21. **Depth-resolved investigation of the in-plane magnetic correlations in magnetic multilayers by scattering of polarized neutrons under grazing incidence**
Dr. E. Kentzinger, Institut für Festkörperforschung, Forschungszentrum Jülich
15. 07. 2005
22. **Conference Reports**
Members of Walther-Meissner-Institute
21. 10. 2005
23. **Josephson self-frustrated networks with π -junctions: possible applications in digital and quantum logics**
Prof. Valerii Ryazanov, Institute of Solid State Physics, Chernogolovka, Russia
28. 10. 2005
24. **Novel physics in copper-oxide high-temperature superconductors**
Dr. Yoichi Ando, Central Research Institute of Electric Power Industry, Japan
04. 11. 2005
25. **Pulsed measurements of a flux qubit using a capacitive bias**
Frank Deppe, Walther-Meissner-Institute
11. 11. 2005
26. **Superconducting triplet correlations in the half-metallic ferromagnet CrO_2**
ir. Ruurd Keizer, Kavli Institute of NanoScience Delft University of Technology
25. 11. 2005
27. **Micromagnetism and Magnetotransport in Domain Patterns of Permalloy Microelements**
Dr. habil. Guido Maier, Institut für Angewandte Physik, Universität Hamburg
02. 12. 2005
28. **Investigation of spectroscopic ellipsometry for the characterization of electrochemically produced technical layers for microelectronics packing applications**
Jan Perlich, Physik-Department, TUM Garching
06. 12. 2005
29. **Oscillations of the order parameter and transition temperature in Nb/CuNi interfaces: Evidence for reentrant superconductivity**
Dr. V. Zdravkov, Institute of Applied Physics, Kishinev, Moldova
09. 12. 2005
30. **Novel Josephson Effect in Triplet Superconductor-Ferromagnet-Triplet Superconductor Junctions**
Dr. habil. Dirk Manske, MPI für Festkörperforschung, Stuttgart
16. 12. 2005

Topical Seminar on Macroscopic Quantum Systems – WS 2004/2005

This topical seminar was held for students in the 7th and 8th semester. It is part of the special physics courses on superconductivity and low temperature physics offered by the WMI.

1. **Quantenflüssigkeiten I**
Dietrich Einzel
30. 11. 2004
2. **Quantenflüssigkeiten II**
Dietrich Einzel
07. 12. 2004
3. **Geladene Quantenflüssigkeiten: Supraleitung**
Markus Bröll
14. 12. 2004
4. **Quantenmechanische Grundlagen der Supraleitung**
Martin Zeppenfeld
18. 01. 2005
5. **Supraleitende Quanteninterferometer**
Susanne Hofmann
25. 01. 2005
6. **Transporteigenschaften von Quantenflüssigkeiten: Zwei-Flüssigkeiten-Modell**
Yvonne Gawlina
01. 02. 2005
7. **Quanteninterferenzexperimente mit atomaren Gasen**
Eva Riedlberger
08. 02. 2005

Topical Seminar on Advances in Solid State Physics – SS 2005 and WS 2005/2006

This topical seminar was held for students in the 7th and 8th semester. It is part of the special physics courses on superconductivity and low temperature physics as well as on magnetism and spintronics offered by the WMI. For the WS 2005/2006 the main topic of the seminar is “Macroscopic Quantum Systems in Solids”.

1. **Analytic two-fluid description of unconventional superconductivity**
Dietrich Einzel
19. 04. 2005
2. **Magnetisierungsmessungen an festem ³He**
Matthias Kath
26. 04. 2005
3. **Co-doped Zinc oxide**
03. 05. 2005
Maïke Lübke
4. **Neues vom ferrimagnetischen Doppelperovskit Sr₂CrWO₆**
10. 05. 2005
Petra Majewski
5. **Großer Tunnelmagnetwiderstand bei Raumtemperatur in ferromagnetischen Tunnelkontakten mit MgO-Barriere**
17. 05. 2005
Matthias Kehr
6. **La-doping in epitaxial thin films of La_xSr_{2-x}CrWO₆**
24. 05. 2005
Robert Geißler

7. **Heterostructures based on ZnO**
31. 05. 2005
Karl Nielsen
8. **Raman study of charge ordering phenomena in cuprates**
21. 06. 2005
Leonardo Tassini
9. **Magnetische Tunnelkontakte aus Magnetit**
28. 06. 2005
Edwin Menzel
10. **Gekreuzte Andreev Reflexion in Supraleiter-Ferromagnet-Hybridstrukturen**
08. 07. 2005
Thomas Goßner
11. **Magnetismus in Sr-basierten Doppelperowskiten**
12. 07. 2005
Oliver Sanganas
12. **Makroskopische Quantensysteme: Konzept der makroskopischen Wellenfunktion**
22. 11. 2005
Susanne Hofmann
13. **Makroskopische Quanteninterferenz in Supraleitern: Supraleitende Quanteninterferometer (SQUIDs)**
29. 11. 2005
Marc Tippmann
14. **Makroskopisches Quantentunneln und makroskopische Quantenkohärenz: Josephson-Kontakte und rf-SQUIDs**
06. 12. 2005
Thomas Hell
15. **Makroskopisches Quantentunneln der Magnetisierung**
13. 12. 2005
Christoph Geißinger
16. **Quantisierung elektromagnetischer Schaltkreise: LC-Oszillator und supraleitende Ladungs-Fluss-Qubits**
20. 12. 2005
Matthias Weiler
17. **Quantenmechanische Zwei-Niveausysteme**
10. 01. 2006
Gunther Jegert
18. **Quantenmechanische Zwei-Niveausysteme in Resonatoren: cQED**
17. 01. 2006
Matthias Althammer
19. **Supraleitende Fluss/Phasen-Qubits**
24. 01. 2006
Hans-Martin Eiter
20. **Dekohärenz**
31. 01. 2006
Stefan Nimmrichter
21. **Quantenmechanischer Messprozess und Quantentomographie**
07. 02. 2006
Thorbjörn Buck

Lectures

A: Technical University of Munich

Dietrich Einzel

- WS 2004/2005
- Mathematische Methoden der Physik I (Mathematical Methods of Physics I)
 - Übungen zu Mathematische Methoden der Physik I (Mathematical Methods of Physik I, Problem Sessions)
 - Festkörperkolloquium (Colloquium on Solid State Physics (with R. Gross))
 - WMI-Seminar über aktuelle Fragen der Tieftemperatur-Festkörperphysik (WMI Seminar on Current Topics of Low Temperature Solid State Physics) (with R. Gross)
- SS 2005
- Mathematische Methoden der Physik II (Mathematical Methods of Physics II)
 - Übungen zu Mathematische Methoden der Physik II (Mathematical Methods of Physics II, Problem Sessions)
 - Supraleitung und Suprafluidität (Superconductivity and Superfluidity)
 - Festkörperkolloquium (Colloquium on Solid State Physics (with R. Gross))
 - WMI-Seminar über aktuelle Fragen der Tieftemperatur-Festkörperphysik (WMI Seminar on Current Topics of Low Temperature Solid State Physics) (with R. Gross)
- WS 2005/2006
- Mathematische Methoden der Physik I (Mathematical Methods of Physics I)
 - Übungen zu Mathematische Methoden der Physik I
 - Festkörperkolloquium (Colloquium on Solid State Physics (with R. Gross))
 - WMI-Seminar über aktuelle Fragen der Tieftemperatur-Festkörperphysik (WMI Seminar on Current Topics of Low Temperature Solid State Physics) (with R. Gross)

Rudolf Gross

- WS 2004/2005
- Festkörperphysik I (Solid State Physics I)
 - Übungen zu Festkörperphysik I in Gruppen (Solid State Physics I, exercises)
 - Magnetismus (Magnetism, with M. Opel)
 - Festkörperkolloquium (Colloquium on Solid State Physics (with D. Einzel)
 - WMI-Seminar über aktuelle Fragen der Tieftemperatur-Festkörperphysik (WMI Seminar on Current Topics of Low Temperature Solid State Physics) (with D. Einzel)
 - Seminar über Mesoskopische Systeme und Nanostrukturen (Seminar on Mesoscopic Systems and Nanostructures)
- SS 2005
- Festkörperphysik I (Solid State Physics I)
 - Übungen zu Festkörperphysik I in Gruppen (Solid State Physics I, exercises)
 - Spinelektronik (Spin Electronics, with M. Opel, A. Marx)
 - Festkörperkolloquium (Colloquium on Solid State Physics (with D. Einzel)
 - WMI-Seminar über aktuelle Fragen der Tieftemperatur-Festkörperphysik (WMI Seminar on Current Topics of Low Temperature Solid State Physics) (with D. Einzel)
- WS 2005/2006
- Angewandte Supraleitung (Applied Superconductivity)
 - Festkörperkolloquium (Colloquium on Solid State Physics (with D. Einzel)
 - WMI-Seminar über aktuelle Fragen der Tieftemperatur-Festkörperphysik (WMI Seminar on Current Topics of Low Temperature Solid State Physics) (with D. Einzel)
 - Seminar über Makroskopische Quantensysteme in Festkörpern (Seminar on Macroscopic Quantum Systems in Solids)

Rudi Hackl

- WS 2004/2005
- Supraleitung und Tieftemperaturphysik I (Superconductivity and Low Temperature Physics I, with D. Einzel)
 - Übungen zu Supraleitung und Tieftemperaturphysik I (Superconductivity and Low Temperature Physics I, exercises, with D. Einzel)
- WS 2005/2006
- Supraleitung und Tieftemperaturphysik I (Superconductivity and Low Temperature Physics I)

Anton Lerf

- WS 2004/2005
- Angewandte Anorganische Chemie II: Feste Stoffe (Applied Inorganic Chemistry II: Solids)
 - Moderne Aspekte der Chemie für Physiker I (Modern Aspects of Chemistry for Physicists I)
- SS 2005
- Moderne Aspekte der Chemie für Physiker II (Modern Aspects of Chemistry for Physicists II)
 - Nanostrukturierte Materie (Nanostructured Matter)
- WS 2005/2006
- Angewandte Anorganische Chemie II: Feste Stoffe (Applied Inorganic Chemistry II: Solids)

Erwin Schubert

- WS 2004/2005
- Experimente bei tiefsten Temperaturen 1 (Experiments at very Low Temperatures 1)
- SS 2005
- Angewandte Physik: Supraleitung und Tieftemperaturphysik II (Applied Physics: Superconductivity and Low Temperature Physics II)
- WS 2005/2006
- Höhere Physik 1 (Advanced Physics I)

B: Ludwig-Maximilians University of Munich**Bianca Hermann**

- WS 2004/2005
- Selbst-organisierende Moleküle
 - Zwergerluni
- SS 2005
- Experimentalphysik II (Experimental Physics II) (with R. Kersting, D. Lüst)
 - Seminar: Dissertationen und Diplomarbeiten schreiben
- WS 2005/2006
- Hauptseminar: Tiefkalte Quantenphänomene
 - Erstkontakt mit der Programmiersprache LabVIEW (First contact with the programming language LabVIEW)

Staff of the Walther-Meissner-Institute

Director

Prof. Dr. Rudolf Gross

Deputy Director

Dr. Werner Biberacher

Head of the Scanning Probe Division

Prof. Dr. Bianca Hermann

Administration/Secretary's Office

Jutta Laaser

Emel Dönertas

Scientific Staff

Dr. Dieter Andres

Dipl.-Phys. Andrea Boger

Dr. Werner Biberacher

Dipl.-Phys. Stephan Geprägs

Dr. habil. Dietrich Einzel

Dipl.-Phys. Wolfgang Prestel

Dr. habil. Andreas Erb

Dipl.-Phys. Michael Lambacher

Dr. Sebastian Gönnenwein

Dipl.-Phys. Karl Madek

Dr. habil. Rudi Hackl

Dipl.-Phys. Georg Wild

Dr. Mark Kartsovnik

Dipl.-Phys. Markus Schmeißner

Prof. Dr. Anton Lerf

Dipl.-Phys. Matthias Kath

Dr. Achim Marx

Dipl.-Phys. Bettina Welter

Dr. Matthias Opel

Dipl.-Phys. Frank Deppe

Prof. Dr. Erwin Schubert

Dipl.-Phys. Petra Majewski

Dr. Jürgen Schuler

Dipl.-Phys. Matteo Mariantoni

Dr. Kurt Uhlig

Dipl.-Phys. Karl-Wilhelm Nielsen

Dipl.-Phys. Leonardo Tassini

Dipl.-Phys. Tobias Heimbeck

Technical Staff

Thomas Brenninger

Jan Naundorf

Joachim Geismann

Georg Nitschke

Gabrielle Görblich

Walter Nitschke

Ulrich Guggenberger

Christian Reichlmeier

Dieter Guratzsch

Harald Schwaiger

Josef Höss

Helmut Thies

Julius Klaus

Siegfried Wanninger

Robert Müller

Assistants

Sybilla Plöderl

Brigitte Steinberg

Permanent Guests

Prof. Dr. B. S. Chandrasekhar

Dr. Robert Doll

Prof. Dr. Schöllhorn

Guest Researchers

1. Prof. Dr. B.S. Chandrasekhar
permanent guest
2. Dr. Robert Doll
permanent guest
3. Prof. Dr. Schöllhorn
permanent guest
4. Prof. Dr. Juan Poyato Ferrera, Instituto de Ciencia de Materiales, Sevilla, Spain
15. 07. – 17. 08. 2005
5. Verónica Ramirez del Valle, Instituto de Ciencia de Materiales, Sevilla, Spain
15. 07. – 17. 08. 2005
6. Dr. Nataliya D. Kushch, Institute of Problems of Chemical Physics, Chernogolovka, Russia
17. 11. – 14. 12. 2005
7. Dr. Sergei Pesotskii, Institute of Problems of Chemical Physics, Chernogolovka, Russia
14. 04. – 23. 05. 2005
8. Prof. T.P. Devereaux, University of Waterloo, Canada
17. 05. – 06. 08. 2005
9. Prof. A. Zawadowski, Budapest University of Technology and Economics, Budapest, Ungarn
01. 06. – 10. 06. 2005
10. Prof. A. Janossy, Budapest University of Technology and Economics, Budapest, Ungarn
27. 06. – 30. 06. 2005
11. Prof. I. Tüttö, Research Institute for Solid State Physics and Optics Hungarian Academy of Sciences, Budapest, Ungarn
25. 07. – 29. 07. 2005
12. Sergey Simonov, Institute of Solid State Physics, Chernogolovka, Russia
17. 06. – 16. 07. 2005
13. Taylor Stock, Trent University, Canada
05. 10. – 11. 11. 2005

Commission for Low Temperature Physics

Members of the Commission for Low Temperature Research of the Bavarian Academy of Sciences:

Kaiser, Wolfgang, Leiter (Technische Universität München)
Abstreiter, Gerhard (Technische Universität München)
Brenig, Wilhelm, stellv. Leiter (Technische Universität München)
Gross, Rudolf (Walther-Meißner-Institut)
Landwehr, Gottfried (Universität Würzburg)
Hänsch, Theodor (Max-Planck-Institut für Quantenoptik, Garching)
Kotthaus, Jörg Peter (Ludwig-Maximilians-Universität München)
Renk, Karl Friedrich (Universität Regensburg)
Schwoerer, Markus (Universität Bayreuth)
Vollhardt, Dieter (Universität Augsburg)

Prof. Dr. Frederick Koch, Technical University of Munich, has retired in 2005 and left the Commission for Low Temperature Research. He was replaced by Prof. Dr. Gerhard Abstreiter, Walter Schottky Institute of the Technical University of Munich.